The progenitors of Type Ia Supernovae: What can we learn from the circumstellar medium around single degenerate systems?

Richard Anthony Booth

Physics Department and Worcester College, Oxford

A thesis submitted for the degree of Doctor of Philosophy
in the University of Oxford.

Michaelmas Term 2013

Declaration

I declare that no part of this thesis has been accepted, or is currently being submitted, for any degree or diploma or certificate or any other qualification in this University or elsewhere. Chapters 5 and 6 rely on simulations carried out by Shazrene Mohamed at the South African Astronomical Observatory. However, all text, figures and descriptions of the simulations are my own. Otherwise, except where explicit reference is made to the work of others, the work contained in this thesis is my own, and is not the outcome of work done in collaboration.

Richard A. Booth

(April 2014)

The progenitors of Type Ia Supernovae: What can we learn from the circumstellar medium around single degenerate systems?

Richard A. Booth

Worcester College

Submitted for the Degree of Doctor of Philosophy

Hilary 2014

Abstract

While the progenitors of Type Ia supernovae (SNe Ia) have long been thought to be thermonuclear explosions of white dwarf stars, what triggers the explosion are still a topic of debate. This thesis considers constraints on single-degenerate progenitors of SNe Ia based on the presence of a Roche-lobe filling companion. The ejecta strips material from the companion, that maybe detectable via Hα emission during the nebular phase. Using the full structure from simulations produces line widths are larger than those produced in simple models.

The structure formed by the ejecta-companion interaction produce a broken reverse shock that may be visible in X-rays via the Fe Kα line at the age of Tycho's supernova remnant (SNR). If the similar structures in Tycho's SNR are produced this way then the companion star must have been massive, with $M \sim 2\,M_\odot$.

Detections of circumstellar material within the supernova provides another way to indirectly probe the companion star. Mass loss through winds or novae are expected to shape the circumsteller medium for single-degenerate progenitors and the velocities, $v \sim 100\,\mathrm{km\,s^{-1}}$ appear to be consistent with recurrent nova shells, a model that is tested by analysing simulations of RS Ophiuchi.

Models of RS Ophiuchi can explain the absorption lines seen around the 2006 outburst if the mass loss is $10^{-6}\,M_\odot\,\mathrm{yr}^{-1}$. The circumsteller medium is shown to produce in the velocity and relative strengths of the features seen in SN 2006X. However, whether density in the shells is high enough to produce the required recombination timescale and to overcome ionization by γ-rays for shells at $5 \times 10^{16}\,\mathrm{cm}$ remains uncertain.

Acknowledgements

Firstly, I would like to take the opportunity to thank my supervisor, Philipp Podsiadlowski, for the support and guidance he has given me during throughout this project. His advice and encouragement has been instrumental to my understanding of the topics in question and has lead me to a deeper understanding of physics behind the models.

I am grateful of the support from the administration team in Oxford, Ashling Morris and Vanessa Ferraro-Wood, who have ensured the smooth running of my D.Phil. I am also grateful for the opportunities to tutor and demonstrate provided to me by Philipp, and Jeff Tseng. I am very grateful the opportunities provided to travel to conferences and present my work, which were a great help in developing many of the skills required to complete this work.

I would like to thank a number of the staff and students, with whom I had many enjoyable and provocative discussions with during my time. Mark Sullivan and Kate Maguire, Phil Bull, Will Potter, Thibaut Louis, Jean Teyssandier and Henry Tillson to name but a few. There were many more, that I am sure I have forgotten to mention.

I would like to thank Cathie Clarke, Jonathan Gair and Sergei Taraskin in Cambridge for all of their help and encouragement during my undergraduate degree. Without them and their advice, I surely would not be where I am today. I would also like to thank my physics teachers in school, particularly Anne Duffy, who nurtured my interests in physics.

I would like to thank my family, without whom none of this would have been possible for the years of encouragement and support, who were always helping me to aim higher and achieve what I did not believe possible.

Finally, I must thank Isabel, who has been so dependable during the entire time. I don't know how you do it!

For my family.

Contents

List of Figures

Chapter 1

Introduction

The nature of Type Ia supernovae (SN Ia) has remained a mystery despite decades of research, which belies their relative homogeneity. Observationally they are distinguished by a lack of hydrogen and helium lines in their spectra, along with the presence of strong silicon lines. The spectral evolution appears homogeneous in comparison with the variety seen in Type II supernovae, and the spectra show velocities in excess of $10^4\,\mathrm{km\,s^{-1}}$.

The spectral homogeneity of Type Ia supernovae has been known for a long time (Minkowski, 1939); however, there is intrinsic variation amongst them. While there are clearly sub-samples of peculiar over-luminous (SN 1991T-like, Filippenko et al., 1992a) or under-luminous (SN 1991bg-like, Filippenko et al., 1992b), it became clear that 'normal' SN Ia show variation. One of the most notable is the correlation between maximum luminosity and decline rate of the luminosity after maximum light (Pskovskii, 1977; Phillips, 1993). In general, the more luminous supernovae are slower declining and have higher velocities. However, currently there is little to be gained in applying multiple parameter models for normalising the luminosity (Branch, 1998; Maguire et al., 2012).

Furthermore, the properties of Type Ia supernova have been shown to depend on their environment, star forming galaxies tend to host supernovae that are more luminous by 0.2-0.3 mag (Hamuy et al., 1995), although these supernovae still sit on the luminosity-decline rate relation. Star forming galaxies also tend to have a higher rate of SN Ia per unit stellar mass than ellipticals (Cappellaro

et al., 1997) and the supernova rate is proportional star formation rate in star forming galaxies (Sullivan et al., 2006).

The presence of SN Ia in elliptical galaxies is a key difference to Type II supernovae, which have not been conclusively seen in ellipticals, showing that at least some SN Ia must come from low mass stars in older stellar populations. This is supported by their lack of association to star formation relative to Type II supernovae (Anderson et al., 2012)

The difference in rates and properties between SN Ia in spiral and elliptical galaxies may be explained by a difference between supernovae occurring promptly ($< 10^8$ yr) after star formation and those that are more delayed (Mannucci et al., 2006), as elliptical galaxies should only host the delayed channel. However, it appears that the delay-time distribution of SN Ia is also consistent with a continuous distribution following approximately a $\frac{\mathrm{d}N}{\mathrm{d}t} \propto t^{-1}$ law (Totani et al., 2008; Maoz et al., 2010, 2012).

The relative homogeneity and intrinsic variability in Type Ia supernovae provide one of the major insights into their possible progenitors, which along with the distinctive lack of hydrogen in their spectra, led to the currently accepted scenario that SN Ia involve the thermonuclear explosion of a white dwarf. This explanation for SN Ia was originally put forward by Hoyle & Fowler (1960), albeit as an explanation for Type II supernovae as well. The nuclear burning during explosion leads to the production of several $0.1 M_\odot$ of ^{56}Ni (Truran et al., 1967), which is radioactive and decays with a half-life of 6 days. Colgate & McKee (1969) showed that the $^{56}\mathrm{Ni} \rightarrow ^{56}\mathrm{Co} \rightarrow ^{56}\mathrm{Fe}$ decay chain can power the light curve of the supernova, helping the model become more generally accepted. However, there is some debate over how what triggers the explosion.

The first model for the explosion of a white dwarf through carbon burning is due to Arnett (1969), who found that once the mass reaches $M = 1.37 M_\odot$ the central density is high enough for carbon burning to become explosive. Arnett's models were deficient intermediate mass elements ($6 < Z < 21$) compared to observations (Arnett et al., 1971). Among the first models that were successful at reproducing the spectra was the W7 model of Nomoto et al. (1984), which could explain many of the features present in spectra of Type Ia supernovae when artificial mixing was invoked in the outer-layers. The key difference between the Arnett et al. (1971) model and Nomoto et al. (1984)

W7 model is that in Arnett's model the carbon burning wave was a detonation, in which the carbon burning front is supersonic, while in the W7 model the carbon burning front is subsonic, a deflagration. This resulted in weaker carbon burning and the production of more intermediate mass elements.

Delayed-detonation models, in which the nuclear burning starts off subsonic and transitions to a supersonic detonation wave, represent an intermediate to the pure detonation models of Arnett (1969) and deflagration models Nomoto et al. (1984). The amount ^{56}Ni produced in delayed-detonation models depends on the density at which the deflagration-to-detonation transition occurs (Khokhlov, 1991). This provides a possible mechanism for explaining the small intrinsic variations seen in SN Ia, as well as a good match to observations of normal SN Ia (Hoeflich & Khokhlov, 1996).

As isolated white dwarfs below the Chandrasekhar mass are inert, an explanation is needed as to what causes them to explode. Whelan & Iben (1973) developed a model in which the white dwarf is in a binary and accretes gas from a companion star. The binary initially consists of a primary with mass $M_{\rm P} \sim 3 - 8 M_{\odot}$ and a secondary with lower mass $M_{\rm S} < 1 M_{\odot}$. The more massive star evolves most rapidly, which loses it's envelope during the giant phase through mass loss or mass transfer, leaving behind a carbon-oxygen (CO) white dwarf. During this time the less massive star remains on the main sequence. Later, as the secondary evolves it expands and begins transferring mass to the white dwarf. Once the white dwarf has accreted sufficient material to reach the Chandrasekhar mass it explodes as a Type Ia supernova.

Prior to the explosion, the white dwarf undergoes a period of quiescent carbon burning in the core. Initially the core is stabilized by neutrino cooling, followed by convective transport. Due to the high densities before the explosion, convection is modified by the Urca process (Paczyński, 1972). The Urca process involves the cyclic electron-capture and beta decay of a pair of elements with the same atomic mass, A, and nuclear charges Z and $Z-1$. The processes

$$(Z, A) + e^{-} \rightarrow (Z-1, A) + \nu \tag{1.1}$$

$$(Z-1, A) \rightarrow (Z, A) + e^{-} + \bar{\nu}, \tag{1.2}$$

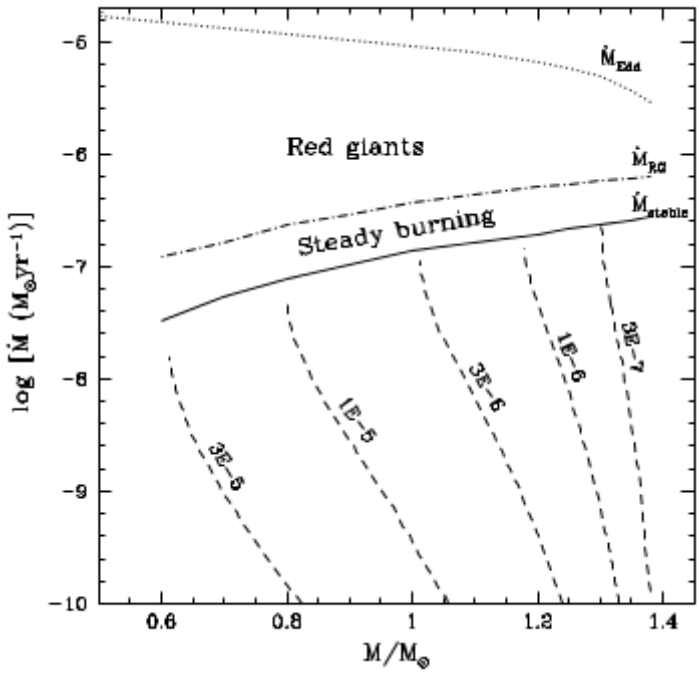

Figure 1.1: Different burning regimes for accretion onto a white dwarf. The range of accretion rates for which steady hydrogen burning can occur is relatively narrow. Above this range the accreted material expands to form an envelope, similar to red giant and mass loss may occur through winds. Below the range, the white dwarf undergoes recurrent novae. The dashed lines trace the mass over of the envelope accreted before the novae occur. [Reproduced from Nomoto et al. (2007)]

both result in the release of a neutrino that cools the core. At an appropriate density shell in the core electron capture and beta decay rates are in equilibrium, which can result in significant cooling. Away from chemical equilibrium, as is found in the convective case, the electrons captured and ejected dominates the energy budget, resulting in heating of the core (Bruenn, 1973). The Urca process results in a smaller convective core at the time of explosion, which occurs after typically 10^3 yr of quiescent burning (Lesaffre et al., 2006; Stein & Wheeler, 2006). The difficulty in accurately calculating the Urca process is one main uncertainties in the structure of the white dwarf at the time of explosion.

Despite the successes of the model there are a number of difficulties. One of the main problems that remains is the range of accretion rates which lead to the white dwarf growing in mass is small (see Fig. 1.1, Nomoto, 1982a; Nomoto et al., 2007). If the mass loss rate is too high ($5\times10^{-7} M_\odot$ yr^{-1} for $M \approx 1.35 M_\odot$) the accretion forms an envelope that is similar to a red giant (Nomoto et al.,

1979) and mass may be lost through winds, or this could lead to a common envelope phase and potentially eject the envelope. For accretion rates that are too low ($10^{-7} M_\odot\,\mathrm{yr}^{-1}$ for $M \approx 1.35 M_\odot$), the nuclear burning occurs through shell-flashes, which give rise to novae. The novae are expected to eject the majority of, or perhaps more than, the accreted mass (Yaron et al., 2005). The large fraction of mass lost through novae means that it may be difficult for white dwarf stars to reach the Chandrasekhar limit while accreting this way. In the intermediate region the white dwarf should burn the accreted hydrogen stably and may appear as a super-soft source (e.g. Nomoto et al., 2007).

Sub-Chandrasekhar mass explosions have also been considered, which have the advantage of avoiding the need for large amounts of accretion. An explosion may be triggered on a helium accreting white dwarf via a Helium shell flash once the 0.1 to $0.2 M_\odot$ of Helium has built up on the surface (Nomoto, 1982b; Woosley et al., 1986). Depending on the mass and accretion rate, helium detonation may lead to a the detonation of carbon in the core. In the absence of a second detonation these models eject only a small mass consisting mainly of ^{56}Ni and leave behind a remnant. In the case of a double detonation the whole white dwarf is disrupted, however current models produce too much ^{44}Ti, resulting in a far redder colour than observed SN Ia (Woosley et al., 1986; Kromer et al., 2010). More recently, Fink et al. (2010) found that helium detonations in two-dimensional simulations always produce secondary carbon detonations; however, Moll & Woosley (2013) found that double detonations can only occur in helium shells with $M_{\mathrm{He}} \gtrsim 0.05 M_\odot$.

Work on an alternative, double-degenerate model for Type Ia supernovae began with Iben & Tutukov (1984) and Webbink (1984), which involves the merger of two white dwarf stars. Stellar evolution predicts that there should be enough of these systems to account for the supernova rate, and a merger presents a relativity easy way to get the total mass above the Chandrasekhar limit. However, there has been considerable debate whether the merger results in a Type Ia supernova. The less massive white dwarf is completely disrupted during the merger, forming a disc around the more massive white dwarf. Accretion from the disc can induce quiescent, off-centre carbon burning, converting the core of the white dwarf from CO to ONeMg, resulting an accretion induced collapse (Nomoto & Iben, 1985) and formation of a neutron star. However, a more recent investigation has shown that this may not be universally true, as for sufficiently low accretion rates ($\dot{M} <$

$5 \times 10^{-6} M_{\odot}\,\mathrm{yr}^{-1}$) neutrino cooling may be able to prevent off centre carbon burning (Yoon et al., 2007).

Another interesting prospect for the formation of Type Ia supernovae appeared to be triggering detonation during violent mergers of white dwarfs. Hydrodynamic simulations by Pakmor et al. (2012) showed that nearly equal mass mergers could lead to carbon detonation in CO+CO which dwarf mergers. However, Dan et al. (2014) calculated the merger properties for a range of binaries, finding that CO+CO white dwarf systems do not ignite as they merge. The models differ by their initial conditions, Pakmor et al. (2012) used non-rotating white dwarfs in their initial conditions, which appears to be at odds with the constraint that the white dwarfs should be co-rotating at the onset of mass transfer (Fuller & Lai, 2012). In contrast to this, Dan et al. (2012) showed that if there is a significant helium layer on the surface of the white dwarf then prompt detonation of the helium can occur, though this does not result in the total destruction of the white dwarf. These might be similar to the edge-lit models of Nomoto (1982b). Although they are unlikely to explain Type Ia supernovae, they might be able to explain sub-luminous events like SN 2002cx (Li et al., 2003).

While ab initio modelling of spectra and light curves provides one way to distinguish between progenitor scenarios the differences are subtle as all successful models are fundamentally similar. Each model discussed depends on explosive carbon burning of CO white dwarf stars resulting in similar energies available. Currently there are differences in the models: double-degenerate progenitors resulting in slower declining light curves (Kromer et al., 2013) and double-detonations produce produce supernovae that are more red (Kromer et al., 2010). However, there are still differences between the results of different groups both within hydrodynamic modelling (e.g. Kromer et al., 2010; Moll & Woosley, 2013) and radiative transfer (Dessart et al., 2013).

An alternative method for distinguishing between progenitor models involves population synthesis, which can be directly related to observed rates and delay-time distribution (Totani et al., 2008; Maoz et al., 2010, 2012). These models naturally seem to favour double degenerate progenitors. Similarly, a measurement of the galactic rate of white dwarf mergers appears to be consistent with supernova rate (Badenes & Maoz, 2012). There is currently a lot of flexibility in population

synthesis models, which is a problem for constraning progenitor scenarios, since it means that most progenitor scenarios can be made to fit. For example, while Gilfanov & Bogdán (2010) show that there are not enough super-soft sources in the galaxy to account for the SN Ia rate, it is known that these sources have a duty cycle (e.g. Kahabka & van den Heuvel, 1997), which may be able to account for the difference.

While direct observations of the progenitors is not feasible, constraining the progenitors via the effects they have on their local environment may be. As the double-degenerate channel requires a long delay time between the formation of the second white dwarf and the explosion, naively one would expect there to be no detectable effect of the progenitors at the time of the supernova. However, non-conservative mass transfer, winds from the companion and recurrent novae should shape the environment around a single-degenerate progenitor.

The main possibilities for studying the interaction of a supernova with its environment are the dynamical interaction the supernova has with the medium, and the effect the medium has on the light from the supernova. These two methods are complimentary, as the dynamical interaction happens slowly over a timescale of several 100 yr, while the interaction between the light and the medium constrain the early evolution of the supernova while the light curve is still radioactively powered. Alternatively, light echoes can be used to study supernovae long after they have occurred. The idea was first proposed by Zwicky (1940). Using the light scattering by dust filaments in the interstellar medium, it has recently become possible to determine the type of some historical supernovae (Rest et al., 2005, 2008).

The work presented in this thesis focusses on using the effects of the secondary to help determine whether SNe Ia can have single-degenerate progenitors. A number of the features discussed may also have explanations based upon double-degenerate or sub-Chandrasekhar models, for example Shen et al. (2013) suggest a model for a circumstellar medium in double-degenerate progenitors. However, the focus will be on considering whether single-degenerate progenitors are compatible with observations.

1.1 Supernova-Companion Interaction

The early signatures of the dynamical interaction of a supernova with it's environment are available through X-ray and radio emission from particles accelerated at the forward shock. The classic example of early radio and X-ray emission from supernovae is the Type IIb supernova SN 1993J (Fransson et al., 1996), in which a mass loss of $\sim 10^{-5} M_{\odot}\,\mathrm{yr}^{-1}$ was measured. So far no Type Ia supernova has been detected in radio or X-rays. The most constraining upper limit is from SN 2011fe, which assuming spherical geometry would appear rule out a mass-loss rate of $10^{-9} M_{\odot}\,\mathrm{yr}^{-1}$ (Horesh et al., 2012; Chomiuk et al., 2012). This assumption is far from valid, which may make the constraint much less severe.

There are notable exceptions, as far as a few hybrid Type Ia/Type IIn supernovae which have showed clear detection of an interaction with circumstellar material. SN 2002ic, SN2005gj and PTF 11kx all show spectroscopic features similar to those seen in Type Ia supernovae (Hamuy et al., 2003; Aldering et al., 2006; Dilday et al., 2012). These supernovae also showed strong Hα emission, which is a signature of circumstellar interaction in Type IIn supernovae. However, these supernovae cannot be considered spectroscopically normal Type Ia supernovae. Therefore, any conclusions about about the circumstellar medium in normal Type Ia supernovae drawn from them would be subject to proving that they are produced by similar mechanisms to the majority of SN Ia, which is not clear. For the rest of this work such supernovae will be excepted from consideration.

The close proximity of a companion star to the supernova means that the ejecta interact with the companion star within the first few hours of the explosion. The stripping and ablation of material from the companion has been studied using analytical calculations based upon the energy and momentum deposition (Colgate, 1970; Wheeler et al., 1975) and more recently using simulations to incorporate the time-dependence of the problem.

Initially simplified models for the companion and ejecta were used (Fryxell & Arnett, 1981; Livne et al., 1992). Calculations by Marietta et al. (2000) were the first to use realistic models for the supernova ejecta and a range of models for the companion star. The calculations showed that for main sequence and sub-giant stars 0.1 to 0.2 $M_{\odot}$ is stripped by the supernova. For red giants the envelope is less strongly bound and is completely stripped by the supernova. The hydrogen-rich

stripped material remains at velocities $v \approx 1000\,\mathrm{km\,s^{-1}}$, much lower than the $v \sim 10^4\,\mathrm{km\,s^{-1}}$ of the supernova ejecta, remaining in the centre of the supernova. The supernova ejecta also become aspherical and the region shadowed by the companion is devoid of ejecta, resulting in a hole with a half-opening angle of approximately 40°. Although the stars used by Marietta et al. (2000) did not take into account full binary evolution, recent calculations that do found largely consistent results (Liu et al., 2012; Pan et al., 2012).

Kasen (2010) studied the effects of the supernova companion on the early light curve. The direct interaction with the companion star is expected to be luminous in X-rays up to $10^{44}\,\mathrm{erg\,s^{-1}}$, which may last up to hours and would be followed by an excess UV emission. The light curve may show a significant UV excess for observers looking down the hole, that could last for several days for a red giant companions. For main sequence companions with, the UV excess is only expected during the first day. For observers viewing the supernova opposite to the hole, the light curve is similar to that from spherical models.

There is some uncertainty in whether the early time emission would be observed for main-sequence companions, since in order to match the spectral evolution to the light curve the supernova may be dark during the first day (Mazzali et al., 2014). Since the temperature from the explosion drops rapidly through adiabatic expansion any initial luminosity is lost within minutes of the explosion and subsequent emission powered by the radioactive decay make take up to a day to escape due to the high opacity within the ejecta. This would mean that by the time the supernova is detected in the optical, any prompt X-ray or early UV would have disappeared. For red-giant companions the UV excess should be detectable within the first five days (Kasen, 2010). An analysis of the early time colours of 100 SNe Ia limits the proportion of SNe Ia with red giant companions to no more than 10 to 20 per cent (Bianco et al., 2011).

The prediction that solar metallicity material should be found deep within the ejecta is currently one of the strongest arguments against single-degenerate progenitors. Due to the low velocity of the hydrogen and the high opacity of the supernova around maximum light, the best prospects for detecting the stripped material is during the nebular phase. At this time, ionization and heating of the ejecta is dominated by scattering of γ-rays (Mazzali et al., 2001). Nebular spectral models

based upon simple approximations for the distribution of stripped companion material suggest that the luminosity of the Hα line should be as high as $10^{35}\,\mathrm{erg\,s^{-1}}$ 300 days after the supernova (Mattila et al., 2005; Lundqvist et al., 2013). If this is the case, then late time observations of SN 2005am, SN 2005cf and SN 2011fe put strict limits on the amount of stripped hydrogen that can be present in the supernovae, which appears to rule out single-degenerate progenitors (Leonard, 2007; Shappee et al., 2013). However, only models considering a uniform distribution of stripped material within the core of the supernova have been used to predict the luminosity. As we will show in Chapter 3, the stripped material is far from uniform and the Hα emission is optically thick, the effects that this has on the emission will be discussed.

However, since the mass stripped from the companion depends on its distance from the supernova, there is a mechanism by which the lack of hydrogen could still be explained. Justham (2011) argued that there may be a delay between the mass transfer and the supernova. Accretion of angular momentum means that rotational support may allow the white dwarf to exceed the Chandrasekhar mass by at least $0.1\,M_\odot$ (Saio & Nomoto, 2004). If rotational support prevents the white dwarf from exploding while it is still accreting, then there could be a delay between the end of accretion and the explosion.

Even if the spin-down time-scale, τ_J, was negligibly short then the delay would be at least as long as the $10^3\,\mathrm{yr}$ for the Urca process. Since this is longer than the Kelvin-Helmholtz timescale on which the envelope contracts, which of the order of years, the companion would no longer be filling its Roche lobe and very little mass would be stripped from it.

However, some of the physical processes involved in the spin-up, spin-down picture are not well understood. The efficiency of accretion of angular momentum affects whether a supernova can occur while the white dwarf is accreting, and the time-scale for angular momentum loss, τ_J, is not well known. Upper limits for τ_J can be derived from heuristic arguments. If $\tau_J > 10^9\,\mathrm{yr}$ then the white dwarf will crystallize and undergo an accretion induced collapse rather than exploding as an SN Ia (Yoon & Langer, 2005). Furthermore, for $\tau_J > 10^6\,\mathrm{yr}$ the central density at ignition would be higher than $2 \times 10^9\,\mathrm{g\,cm^{-3}}$, producing too many stable iron group elements.

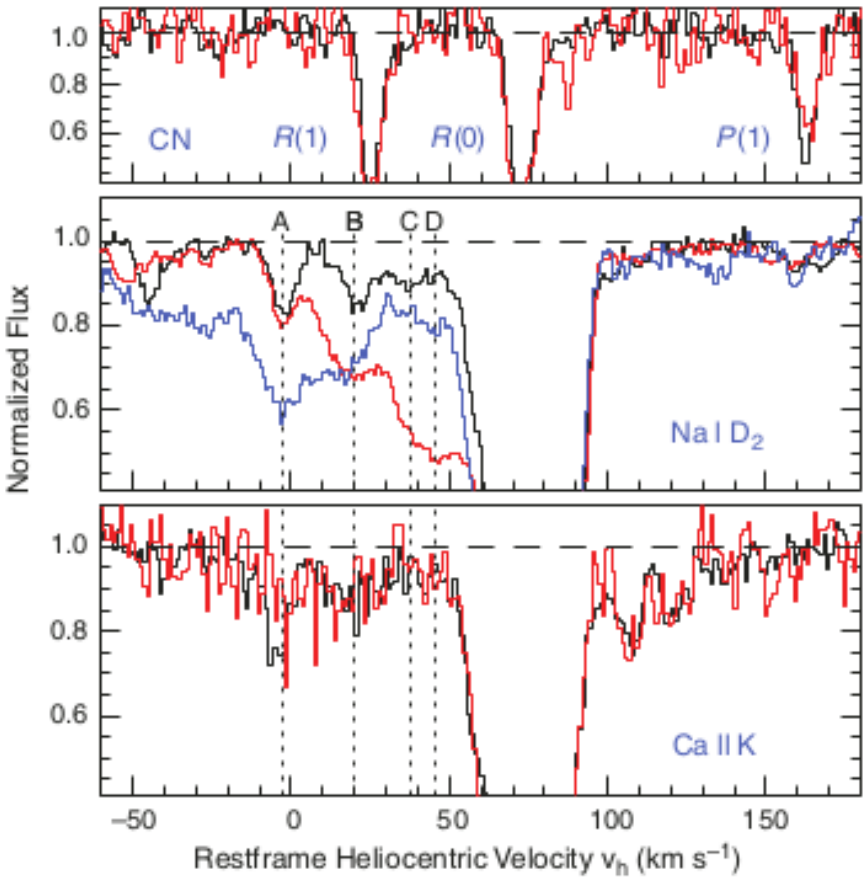

Figure 1.2: Evolution of the Na I D2 and Ca II K line profiles in SN 2006X. The absorption lines are from spectra taken at day −2 (black), day +14 (red), and day +61 (blue, Na I D2 only) relative to the maximum light. The vertical dashed lines mark the four main variable components at −3 ("A"), +20 ("B"), +38 ("C"), and +45 ("D") $\mathrm{km\,s^{-1}}$. The strong absorption at +75 is likely to be due to the local interstellar medium, and is assumed to be coincident with the supernova velocity. [Reproduced from Patat et al. (2007)]

1.2 Circumstellar Material and Recurrent Novae

The first normal Type Ia supernova that showed clear signs of circumstellar material is SN 2006X, which was made through the time evolution of narrow absorption lines in the spectra (Patat et al., 2007). Several components at varying velocities appeared in the absorption lines of different species, including the Na D lines and the Ca II H & K lines. As the strong variation in the Na D lines was not seen in the Ca II lines, it removes the possibility that the variations could be explained by interstellar clouds passing across the line of sight (see Fig. 1.2). Patat et al. (2007) suggest that the

variation is driven by photoionization effects, as no variation was seen in the harder to ionize species (Ca II). While SN 2006X was heavily reddened, it was otherwise a normal Type Ia supernova.

Between days -2 and $+14$ the variable components in SN 2006X all became stronger. If the variation is due to photoionization, then this suggests that the recombination timescale is of order tens of days, which corresponds to a density $n_e \approx 10^5\,\mathrm{cm}^{-3}$ (Patat et al., 2007). Behaviours consistent with recombination on similar timescales was also seen in SN 1999cl and SN 2007le (Blondin et al., 2009; Simon et al., 2009).

However, it has been questioned as to whether the absorption in these two supernovae is really consistent with a detection of circumstellar material. Chugai (2008) argued that the ionization from γ-rays and two-photon ionization caused by the Type Ia supernovae would sufficiently ionize a red-giant wind that the material should not be seen. Furthermore, as the absorption lines were still present in both SN over 100 days after the supernova, the distance to the material must be large $r > 10^{16}\,\mathrm{cm}$, potentially putting the material too far from the supernova for the UV photoionization rate to be high enough. Simon et al. (2009) found similar results for SN 2007le, for which they suggested that observations could be explained by a cloud located 0.1 pc from the supernova with a density of $n_e \sim 10^7\,\mathrm{cm}^{-3}$.

Statistical arguments make a stronger case that these observations may be associated with a pre-supernova outflow. If the absorptions were associated with the interstellar medium, the distribution in velocity should be symmetric about the local interstellar medium velocity. Sternberg et al. (2011) found evidence for a significant excess of supernovae with blue-shifted absorption components over those with red-shifted absorptions. One point of contention for such studies is how well the local rest frame for the supernova is known. Sternberg et al. (2011) used the strongest absorption component as the velocity of the local interstellar medium. A more recent study using the centre of emission lines as a tracer of the local standard of rest found similar results, showing a 20 per cent excess of blue-shifted absorption (Maguire et al., 2013). Current evidence suggests that while a significant fraction of type Ia supernovae show blue-shifted absorption, time-variability is much less common and currently no normal type Ia supernovae have been observed showing a general weakening of the lines (Blondin et al., 2009; Maguire et al., 2013).

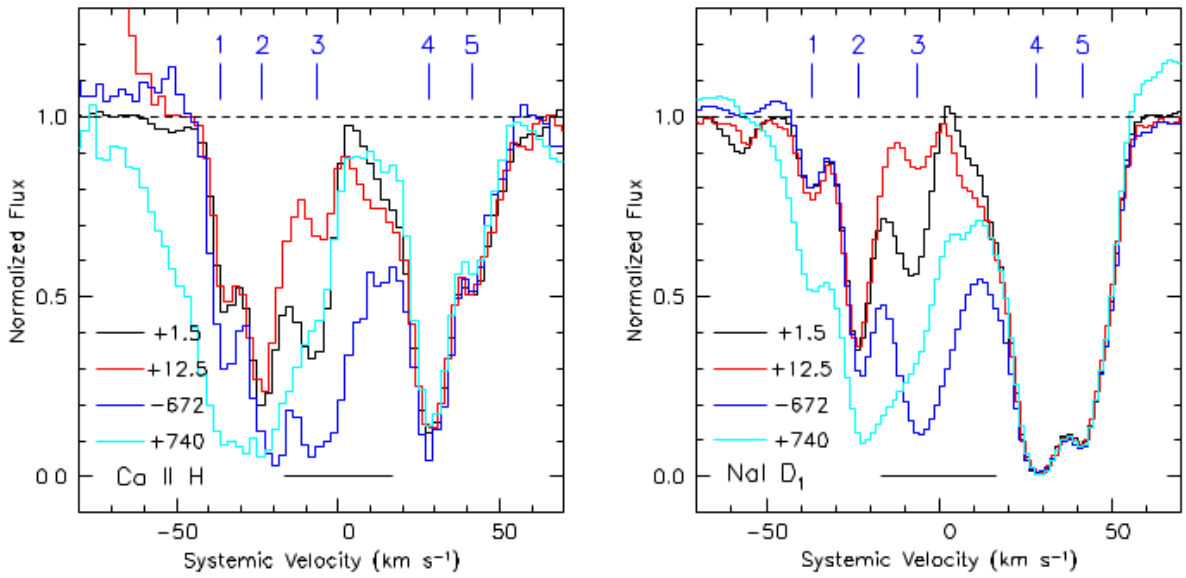

Figure 1.3: Absorption line evolution during the 2006 outburst of the recurrent nova RS Ophiuchi for Ca II H (left) and Na D_1 (right). The two lines show the same velocity components, which weaken during the outburst. After the outburst the highest velocity components strengthen and also have higher peak velocities, suggesting they form in the novae. During quiescence the lines also show red-shifted absorption. [Reproduced from Patat et al. (2011)]

Nova shells were put forward by Patat et al. (2007) as a possible explanation for the origin of the absorption lines in SN 2006X, an argument that is supported by the 2006 outburst of the recurrent nova RS Ophiuchi (RS Oph) (Patat et al., 2011). High-resolution spectra of RS Oph show blue-shifted absorption lines with velocities up to $v \sim 50\,\mathrm{km\,s^{-1}}$ (Fig. 1.3), similar to those seen in SN 2006X.

The credentials of RS Oph as a potential SN Ia progenitor extend further than a detection of circumstellar material. The nova ejected are consistent with having a low mass, $M \sim 10^{-7}\,M_\odot$ (Sokoloski et al., 2006) and high velocity, $v \approx 4000\,\mathrm{km\,s^{-1}}$ (Das et al., 2006; Anupama, 2008). Combined with a recurrence time of 20 yr (Rosino & Iijima, 1987), modelling of the novae suggests the white dwarf is close to the Chandrasekhar mass (Yaron et al., 2005). Measurements of the velocities of the red giant and white dwarf in RS Ophiuchi support a Chandrasekhar mass white dwarf, giving a mass for the red giant companion of $0.8\,M_\odot$ and a period of 453.6 days (Dobrzycka & Kenyon, 1994; Fekel et al., 2000; Brandi et al., 2009). As RS Oph is not an eclipsing system, the orbital elements put tight constraints on the inclination of the system, $i \approx 50°$ to within a fee

degrees (Brandi et al., 2009).

The extensive observing campaigns for RS Oph in outburst and quiescence make it an excellent candidate for testing whether the recurrent novae are compatible with the narrow absorption lines in supernovae. Estimates of the mass-loss rate from the red giant vary between $2 \times 10^{-8}\,M_{\odot}\,\mathrm{yr}^{-1}$ at $v \approx 8\,\mathrm{km\,s}^{-1}$ from dust modelling Evans et al. (2007), to $10^{-6}\,M_{\odot}\,\mathrm{yr}^{-1}$ at $v \approx 30\,\mathrm{km\,s}^{-1}$, estimated using emission lines during the 2006 outburst (Iijima, 2008) and the lower limit is roughly the minimum accretion rate required to power the outbursts (Yaron et al., 2005). Anupama & Mikołajewska (1999) suggest that mass-loss rates above $10^{-7}\,M_{\odot}\,\mathrm{yr}$ are required to explain the appearance of the white dwarf, which has a low effective temperature $T \approx 3 \times 10^{4}\,\mathrm{K}$, as measured in the UV (Dobrzycka et al., 1996).

Resolved imaging during the 2006 outburst of RS Oph using HST and radio interferometry show the nova was bipolar (Bode et al., 2007; O'Brien et al., 2008). While it may be possible that the ejecta were intrinsically bipolar, simulations of mass transfer in binaries show that the mass lost from the system is confined to the binary plane (Theuns & Jorissen, 1993). As novae interact with the wind they become bipolar (Walder et al., 2008; Orlando et al., 2009). Chapters 5 and 6 aim to tackle the question of whether the circumstellar medium formed by novae like RS Oph can be responsible for the variable absorption lines seen in SN 2006X and the absorptions in SNe Ia in general by using simulations of the circumstellar environment and the novae and the calculating the absorption line profiles that form within the circumstellar medium.

1.3 Supernova Remnants

Supernova remnants provide another way to probe the structure of supernovae. A clear example of this is that while the remnants of SNe Ia are round, core-collapse supernovae produce much more distorted remnants (Lopez et al., 2011). During their early evolution, the dynamics of supernova remnants is ejecta dominated. This remains true for several hundred years, until the supernova has swept up several times its mass (Gull, 1973; Dwarkadas & Chevalier, 1998). The remnants of SN 1006, Tycho's Supernova and Kepler's Supernova show evidence for asymmetries in the explosion (Warren et al., 2005; Chiotellis et al., 2012; Patnaude et al., 2012). The X-ray spectra of Tycho's

SNR and Kepler's SNR also show evidence for pre-supernova mass loss, suggesting they had single-degenerate progenitors (Chiotellis et al., 2012, 2013; Patnaude et al., 2012).

X-ray spectra of Kepler's supernova are best explained by models that include a 0.1 pc hole in centre of the mass loss (Patnaude et al., 2012). For a wind velocity of $20\,\mathrm{km\,s^{-1}}$, the gas would reach 0.1 pc in approximately 5×10^3 yr. This timescale is similar to the timescale on which the white dwarf evolves to explosion via the Urca process (Paczyński, 1972; Lesaffre et al., 2006), which is the minimum time to explosion in the spin-up, spin-down models of Justham (2011). This would also explain why no surviving companion consistent with a stripped giant star has been found for Kepler's Supernova (Kerzendorf et al., 2014).

Currently models for these SNRs are based upon spherical models for the mass loss and ejecta, which is not expected to be the case for single-degenerate progenitors, since the interaction between the supernova and companion may mean the ejecta are not spherical, and in a binary the wind is concentrated towards the binary plane (Podsiadlowski & Mohamed, 2007). García-Senz et al. (2012) used approximate models for the ejecta produced in the interaction between the ejecta and a Roche-lobe filling companion star, showing that the hole in the ejecta survives through to the remnant stage. In Chapter 6, the morphology of SNRs with single-degenerate progenitors are simulated, taking into account the asymmetries that arise to test whether they are consistent with the morphology of supernova remnants.

1.4 Thesis Outline

This thesis considers the prospects and constraints on single-degenerate progenitors of SNe Ia that arise due to effects that the companion star has on the ejecta and the surrounding medium. The specific problems tackled by each chapter are described below

Chapter 2 discusses the numerical methods used to tackle the problems involved in this thesis, including Smoothed Particles Hydrodynamics and the calculation of absorption line profiles from the simulation. Tests are presented that verify the codes used and the requirement for accurate calculations are discussed.

In Chapter 3 calculations of the interaction between supernova ejecta and companion stars

are presented for models appropriate for Tycho's SNR and RS Ophiuchi. The evolution and final morphology are presented and the gas stripped from the companion is analysed. A model of the Hα emission from the stripped companion material is then used to compare the emission from simple distributions of matter the more realistic one from the simulation.

Chapter 4 considers the morphology of supernova remnants formed as the ejecta interact with the interstellar or circumstellar medium. The ejecta structure from Chapter 3 is used, along with models for the circumstellar medium based upon the mass loss from RS Oph presented in Chapters 5 and 6. The resulting structure is then discussed in terms of Tycho's SNR.

Chapter 5 studies the mass transfer in RS Oph and the formation of the binary wind by its interaction with the gravitational potential of the binary. The ionization conditions in the gas are modelled and the resulting absorption lines are compared to observations of RS Ophiuchi. A model for the broad emission lines for Hα, which comes from close to the white dwarf, is discussed.

Chapter 6 uses the circumstellar medium formed in Chapter 5 as the background for the formation of nova shells in RS Oph. These are compared to the absorption lines seen before, during and after the 2006 outburst, which are used to constrain the mass loss from the system. The resulting nova structure is then used to calculate the absorption line profiles expected should RS Oph explode as a SN Ia while in the recurrent nova phase. These are discussed in the context of SN 2006X and the excess of blue-shifted absorption features seen in SN Ia.

Finally, in Chapter 7 the conclusions of the models are presented and the prospects for single-degenerate progenitors of SN Ia are discussed. Further models and tests, including radio and X-ray constraints, that could help determine whether the majority of SN Ia have single-degenerate progenitors are also discussed.

Chapter 2

Numerical Methods

2.1 Hydrodynamics

Many astrophysical processes are governed by the interplay of hydrodynamics with the gravity. From the stellar winds or supernova and their remnants, to accretion or the evolution and dynamics of galaxies, hydrodynamics has a role. Other physical processes, such as relativity, radiation and nuclear or chemical processes, and their interaction with hydrodynamics are often important. For the cases studied in this thesis, the additional physics included are radiative cooling and self-gravity.

In general, the equations which govern hydrodynamics are the Navier-Stokes equations. Except in the case of accretion discs, which are driven by viscosity, the effects of viscosity are usually negligible for astrophysical applications. When viscosity can be neglected, the equations reduce to the Euler equations, which including the effects of cooling and self-gravity can be written as

$$\frac{\partial \rho}{\partial t} + \boldsymbol{\nabla} \cdot (\rho \mathbf{v}) = 0, \tag{2.1}$$

$$\rho \left(\frac{\partial \mathbf{v}}{\partial t} + (\mathbf{v} \cdot \boldsymbol{\nabla}) \mathbf{v} \right) + \boldsymbol{\nabla} P = -\rho \boldsymbol{\nabla} \phi, \tag{2.2}$$

$$\frac{\partial E}{\partial t} + \boldsymbol{\nabla} \cdot [(E + p) \mathbf{v}] = -\rho \mathbf{v} \cdot \boldsymbol{\nabla} \phi - \Lambda. \tag{2.3}$$

Here ρ is the density, $\mathbf{v}$ is the velocity, P is the pressure and E is the energy per unit volume. The terms ϕ and Λ are the gravitational potential and net cooling rate. The energy per unit volume, E,

includes the kinetic and thermal energy, $E = \rho u + \frac{1}{2}\rho|\mathbf{v}|^2$, where u is the thermal energy per unit mass.

Equations (2.1) - (2.3) are expressed relative to an inertial co-ordinate system, generally known as an Eulerian Frame. They represent the changes in a physical quantity at a given point in space. An alternative formulation of the equations considers how the properties of a given fluid element change. If we define the quantity scalar $\varphi = \varphi(t, \mathbf{x})$, by the chain rule

$$\frac{\mathrm{d}\varphi}{\mathrm{d}t} = \frac{\partial\varphi}{\partial t} + \boldsymbol{\nabla}\varphi \cdot \frac{\mathrm{d}\mathbf{x}}{\mathrm{d}t}. \tag{2.4}$$

In an Eulerian Frame, the co-ordinates are fixed and $\frac{\mathrm{d}\mathbf{x}}{\mathrm{d}t} = 0$. If we choose $\mathbf{x}$ to be the position of a fluid element at time, t, then $\frac{\mathrm{d}\mathbf{x}}{\mathrm{d}t} = \mathbf{v}$ and $\frac{\mathrm{d}\varphi}{\mathrm{d}t} = \frac{\partial\varphi}{\partial t} + \mathbf{v} \cdot \boldsymbol{\nabla}\varphi$. This is known as the Lagrangian Frame, in which the equations become

$$\frac{\mathrm{d}\rho}{\mathrm{d}t} + \rho\boldsymbol{\nabla} \cdot \mathbf{v} = 0, \tag{2.5}$$

$$\frac{\mathrm{d}\mathbf{v}}{\mathrm{d}t} + \frac{1}{\rho}\boldsymbol{\nabla}P = -\boldsymbol{\nabla}\phi, \tag{2.6}$$

$$\frac{\mathrm{d}u}{\mathrm{d}t} + \frac{P}{\rho}\boldsymbol{\nabla} \cdot \mathbf{v} = -\Lambda. \tag{2.7}$$

2.2 Smoothed Particle Hydrodynamics

The following discussion is based upon Price (2012) and Rosswog (2009) and is restricted to three spatial dimensions, but can be generalized to an arbitrary number of dimensions. The idea behind Smoothed Particle Hydrodynamics is to choose a finite number of points (particles) to represent fluid elements and to derive equations of motion for these fluid elements. Each particle p_i has associated with it a position, $\mathbf{r}_i$; velocity, $\mathbf{v}_i$; mass, m_i and internal energy, u_i.

The density is calculated using an kernel interpolant, by summing over all 'neighbours',

$$\rho(\mathbf{r}) = \sum_i m_i W(\mathbf{r} - \mathbf{r}_i, h). \tag{2.8}$$

If $\int W(r,h)\,\mathrm{d}^3r = 1$ then

$$\int \rho(\mathbf{r})\,\mathrm{d}^3r = \sum_i m_i, \tag{2.9}$$

the total mass in the volume is just the sum of the masses of the particles.

A good choice of W should be smooth, monotonically decreasing, symmetric in r, $W(\mathbf{r}_a - \mathbf{r}_b, h) = W(\mathbf{r}_b - \mathbf{r}_a, h)$, and have $\left.\frac{\mathrm{d}W}{\mathrm{d}r}\right|_{r=0} = 0$. A natural choice for such a kernel is thus a Gaussian kernel, $W(r,h) \propto (1/h^3)\exp(-r^2/h^2)$. The downside to a Gaussian kernel is that it is infinite in extent, which means that the neighbours include all particles, even though the contribution to the density from all but the closest particles will be negligible. One choice of kernels that approximate a Gaussian and are identically zero beyond a certain distance were given by Schoenberg (1946). They can be generated from the Fourier transform

$$M_n(x,h) = \frac{1}{2\pi}\int_{-\infty}^{\infty}\left[\frac{\sin(kh/2)}{kh/2}\right]^n \cos kx\,\mathrm{d}k. \tag{2.10}$$

The functions M_n give rise to polynomials which are of order $n-1$ and are smooth up to $n-2$. The kernel can be written

$$W_n(r,h) = \sigma(h)\begin{cases} M_n(r,h) & r \le \frac{nh}{2}, \\ 0 & r > \frac{nh}{2}, \end{cases} \tag{2.11}$$

where $\sigma(h)$ is a normalizing coefficient. As the kernels are identically zero for $r > \frac{n}{2}h$, this allows the use of a subset of particles in equation (2.8). Usually $n = 4$, the cubic spline kernel, or $n = 6$ the quintic spline kernel are used. In the code GADGET-2 (Springel, 2005), which we use throughout this work, the cubic spline kernel is used. In this case

$$W(r,h) = \frac{1}{\pi h^3}\begin{cases} \frac{1}{4}(2-\frac{r}{h})^3 - (1-\frac{r}{h})^3 & 0 \le r < h, \\ \frac{1}{4}(2-\frac{r}{h})^3 & h \le r < 2h, \\ 0 & r \ge 2h. \end{cases} \tag{2.12}$$

The definition of the smoothing length, h, used here differs from that used by Springel (2005), by a factor of two. With this choice the smoothing length is equivalent to the one in the Gaussian kernel

that it approximates.

The smoothing length is set by solving the equation

$$\frac{4\pi}{3}(\eta h_a)^3 \sum_b W(\mathbf{r}_a - \mathbf{r}_b, h_a) = N_{\mathrm{NGB}}, \tag{2.13}$$

where ηh is the extent of the kernel, with $\eta = 2$ for the cubic spline kernel and N_{NGB} the number of neighbours used, which is a constant. This is equivalent to

$$\frac{4\pi}{3}(\eta h_a)^3 \rho = N_{\mathrm{NGB}} \frac{\sum_b m_b W(\mathbf{r}_a - \mathbf{r}_b, h_a)}{\sum_b W(\mathbf{r}_a - \mathbf{r}_b, h_a)} = N_{\mathrm{NGB}} \bar{m}, \tag{2.14}$$

as given by Springel (2005). This definition for the density represents an integral formulation to the continuity equation (Price, 2008). Taking the time derivative of equation (2.8) along with equation (2.13) verifies that this definition satisfies the continuity equation (equation 2.5).

The discretised form for the momentum equation (equation 2.6) is most easily derived from the Lagrangian, L. In the absence of source terms it is given by

$$L(\mathbf{r}, \mathbf{v}) = \sum_i m_i \left(\frac{1}{2} |\mathbf{v}_i|^2 - u(s, \rho) \right), \tag{2.15}$$

which corresponds to the continuum limit

$$L(\mathbf{r}, \mathbf{v}) = \int \frac{\rho}{2} |\mathbf{v}_i|^2 - \rho u(s, \rho) \, \mathrm{d}^3 r, \tag{2.16}$$

where s is the entropy per unit mass. For an ideal gas the pressure is given by $P = \rho^2 \left.\frac{\mathrm{d}u}{\mathrm{d}\rho}\right|_s$. In general, we must take care because ρ_i depends not only on the positions but also h_i. Following Springel & Hernquist (2002), equation (2.13) can be used to express $h_i = h_i(\{\mathbf{r}_j\})$. Writing $Q_j = \sum_i W(\mathbf{r}_j - \mathbf{r}_i, h_j)$, the constraints can then be included in the Lagrangian using Lagrange multipliers as

$$L(\mathbf{r}, \mathbf{v}, h) = \sum_i m_i \left(\frac{1}{2} |\mathbf{v}_i|^2 - u(s, \rho) \right) + \sum_i \lambda_i \left(\frac{4\pi}{3} (\eta h_i)^3 Q_i - N_{\mathrm{NGB}} \right), \tag{2.17}$$

where each of the terms in the second sum is zero and λ_i are the Lagrange multipliers. The Euler-Lagrange equations for h_i can be used to eliminate λ_i, giving

$$\lambda_i = m_i \left.\frac{\partial u_i}{\partial \rho_i}\right|_s \frac{3}{4\pi(\eta h_a)^3}\left[\frac{\partial Q_i}{\partial \rho_i} + \frac{3\rho_i}{h_i}\frac{\partial h_i}{\partial \rho_i}\right]^{-1}. \tag{2.18}$$

The Euler-Lagrange equations for $\mathbf{r}_i$ give the the momentum equation

$$\begin{aligned}
\frac{\mathrm{d}}{\mathrm{d}t}\left(\frac{\partial L}{\partial \mathbf{v}_i}\right) &= \frac{\partial L}{\partial \mathbf{r}_i}, \\
\frac{\mathrm{d}(m_i\mathbf{v}_i)}{\mathrm{d}t} &= -\sum_j m_j \left.\frac{\partial u_j}{\partial \rho_j}\right|_s \boldsymbol{\nabla}_i \rho_j + \sum_j \lambda_j \frac{4\pi}{3}(\eta h_j)^3 \boldsymbol{\nabla}_i Q_j, \\
&= -\sum_j m_j \frac{P_j}{\rho_j^2}\left[1 + \frac{h_j}{3Q_j}\frac{\partial Q_j}{\partial h_j}\right]^{-1} \boldsymbol{\nabla}_i \rho_j,
\end{aligned} \tag{2.19}$$

where $\boldsymbol{\nabla}_i$ is the gradient operator with respect to $\mathbf{r}_i$. Using the SPH interpolant for the density

$$\boldsymbol{\nabla}_i \rho_j = \sum_k m_k \boldsymbol{\nabla}_i W(\mathbf{r}_j - \mathbf{r}_k, h_j) = \sum_k m_k \frac{\partial W(r_{ij}, h_j)}{\partial r_{ij}}(\mathbf{r}_j - \mathbf{r}_k)(\delta_{ij} - \delta_{ik}). \tag{2.20}$$

Defining $\mathbf{r}_{ij} = \mathbf{r}_i - \mathbf{r}_j$, $r_{ij} = |\mathbf{r}_{ij}|$, $W_{ij}(h) = W(\mathbf{r}_{ij}, h)$ and $f_j = [1 + \frac{h_j}{3Q_j}\frac{\partial Q_j}{\partial h_j}]^{-1}$, the discretised momentum equation (2.19) becomes

$$\begin{aligned}
\frac{\mathrm{d}(m_i\mathbf{v}_i)}{\mathrm{d}t} &= -\sum_j \sum_k m_j m_k f_j \frac{P_j}{\rho_j^2} \boldsymbol{\nabla}_i W_{jk}(h_j)(\delta_{ij} - \delta_{ik}), \\
&= -m_i \sum_j m_j \left[f_j \frac{P_j}{\rho_j^2}\boldsymbol{\nabla}_i W_{ij}(h_j) + f_i \frac{P_i}{\rho_i^2}\boldsymbol{\nabla}_i W_{ij}(h_i)\right].
\end{aligned} \tag{2.21}$$

While equation (2.21) looks identical to the expression given by Springel (2005), it differs in the factors f_j. Springel (2005) gives $f_j = [1 + \frac{h_j}{3\rho_j}\frac{\partial \rho_j}{\partial h_j}]^{-1}$, which would be the correct expression if the equation $\frac{4\pi(\eta h_j)^2}{3}\rho_j = M$, where M is a constant, was used to set the smoothing length instead of equation (2.13). Writing

$$\frac{\rho_i}{Q_i}\frac{\partial Q_i}{\partial h_i}\frac{\partial h_i}{\partial \rho_i} = \frac{\sum_j \frac{\partial W(\mathbf{r}_i - \mathbf{r}_j, h_i)}{\partial h_i}}{\sum_j \frac{m_j}{\bar{m}}\frac{\partial W(\mathbf{r}_i - \mathbf{r}_j, h_i)}{\partial h_i}}, \tag{2.22}$$

we see that the two expressions are equivalent when equal particle masses, $m_j = \bar{m}$, are used. Otherwise, as implemented in GADGET-2, equation (2.21) introduces a small inconsistency in the equations of motion. The terms f_j, capture the difference between the equations of motion with fixed smoothing length and those with variable smoothing length and typically $f_j \approx 1$, which means the error introduced is small. In this work equal particles masses have been used, and the inconsistency can be neglected.

It is worth noting that since $\frac{\partial W_{ij}(h_j)}{\partial \mathbf{r}_{ij}}$ is anti-symmetric in i and j, $\sum_i \frac{\mathrm{d}(m_i \mathbf{v_i})}{\mathrm{d}t} = 0$ and the total momentum is manifestly conserved. The source term for the momentum equation, $-\boldsymbol{\nabla}_i \phi$, is added to the right hand side of equation (2.21), the calculation of which will be discussed later.

Finally, we need a discretised form for the energy equation (2.7). The simplest way to achieve this is to replace the internal energy associated with each particle u_i, with the entropy per unit mass, s_i. For an ideal gas the entropy is conserved in the Lagrangian frame. Thus we can label each particle with $A_i = A(s_i) = P_i/\rho_i^\gamma$, where γ is the adiabatic index. In the absence of viscosity and heating or cooling, A_i can be taken to be constant.

2.2.1 Artificial Viscosity

The derivation of the equations of motion explicitly assumes that the fluid properties are continuous, i.e., their derivatives are well defined. When a fluid contains shocks, then this is no longer the case and the equations break down. The Rankine-Hugoniot conditions can be used to express the fluid properties on either side of a shock. The relationship between the upstream density and pressure (ρ_1, P_1) and downstream values (ρ_2, P_2) are

$$\frac{\rho_2}{\rho_1} = \frac{(\gamma+1)P_2 + (\gamma-1)P_1}{(\gamma-1)P_2 + (\gamma+1)P_1} \tag{2.23}$$

which in the limit of a strong shock $P_2 \gg P_1$ gives the maximum density change $\rho_2 = \rho_1(\gamma+1)/(\gamma-1)$. Re-arranging and using $A = P/\rho^\gamma$ gives

$$\frac{A_2}{A_1} = \left(\frac{\rho_2}{\rho_1}\right)^\gamma \left[\frac{(\gamma+1)\rho_2 - (\gamma-1)\rho_1}{(\gamma+1)\rho_1 - (\gamma-1)\rho_2}\right], \tag{2.24}$$

which shows that entropy increases across the shock. The break down in entropy conservation at the shock reflects the fact that shocks are not reversible processes. Although the shock is adiabatic in the sense that $\delta Q = 0$, this only corresponds to $\delta A = 0$ for reversible processes.

As the SPH discretisation of the Euler equations enforce $\delta A = 0$, it does not allow non-reversible processes. As shocks are ubiquitous in astrophysical applications a modification to the equations is needed.

To find a solution we look to what occurs in nature. In reality a fluid is never totally inviscid. The presence of viscosity broadens shocks and couples the macroscopic flow to microscopic processes in an irreversible way. However, physical viscosity would do little to alleviate the problem as the shocks are too thin to be resolved. The solution, first proposed by von Neumann & Richtmyer (1950) is to use an artificial viscosity to broaden shocks to the resolution of the simulation. The idea is to introduce a viscosity which only acts at shocks. Away from shocks the viscosity should be zero to reproduce the inviscid flow.

The artificial viscosity is implemented by adding an extra pressure term to particles that approach each other. The viscous acceleration is

$$\left.\frac{\mathrm{d}\mathbf{v}_i}{\mathrm{d}t}\right|_{\mathrm{visc}} = -\sum_j m_j \Pi_{ij} \left(\frac{\boldsymbol{\nabla}_i W_{ij}(h_i) + \boldsymbol{\nabla}_i W_{ij}(h_j)}{2}\right), \tag{2.25}$$

and entropy generated by viscosity is given by

$$\frac{\mathrm{d}A_i}{\mathrm{d}t} = \frac{(\gamma-1)}{\rho^{\gamma-1}} \frac{1}{2} \sum_j m_j \Pi_{ij} \mathbf{v}_{ij} \cdot \left(\frac{\boldsymbol{\nabla}_i W_{ij}(h_i) + \boldsymbol{\nabla}_i W_{ij}(h_j)}{2}\right). \tag{2.26}$$

In GADGET-2,

$$\Pi_{ij} = \begin{cases} -\frac{(c_i + c_j - 3w_{ij})w_{ij}}{\rho_i + \rho_j} & w_{ij} < 0, \\ 0 & w_{ij} \geq 0, \end{cases} \tag{2.27}$$

where $w_{ij} = \mathbf{v}_{ij} \cdot \mathbf{r}_{ij}/|\mathbf{r}_{ij}|$ and $c_i + c_j - 3w_{ij} = v_{\mathrm{sig}}$, is an approximation to the signal velocity; the speed at which information travels between two particles. The signal velocity is based on a comparison to Riemann Solvers (Monaghan, 1997). The viscosity is further modified by the use of

a switch (Balsara, 1995), which reduces the viscosity in the presence of shearing flows. The switch,

$$f_i = \frac{|\boldsymbol{\nabla} \cdot \mathbf{v}|}{|\boldsymbol{\nabla} \cdot \mathbf{v}| + |\boldsymbol{\nabla} \times \mathbf{v}| + 10^{-4} c_i / h_i} \tag{2.28}$$

is included by making the substitution $\Pi_{ij} \rightarrow \frac{1}{2}(f_i + f_j)\Pi_{ij}$. The switch works as desired for pure bulk flows $|\boldsymbol{\nabla} \times \mathbf{v}| = 0$, and pure shearing flows $|\boldsymbol{\nabla} \cdot \mathbf{v}| = 0$, but reduces the viscosity where both are present. The presence of some viscosity in flows with a shearing component gives rise to spurious angular momentum transport, in much the same way the physical viscosity drives angular momentum transport in discs. The extent to which angular momentum transport can be an issue is problem dependant, but it is not expected to be significant in this work as the majority of the gas is out-flowing. In this case, $\boldsymbol{\nabla} \cdot \mathbf{v} > 0$ and $\Pi_{ij} = 0$, therefore viscosity only contributes where shocks are expected.

2.2.2 Contact discontinuities, instabilities and artificial conduction

As well as shocks, the Euler equations admit a second type of discontinuity, known as a contact discontinuity, in which the pressure and velocity are continuous, but the density and internal energy are not. Similarly to the case of a shock, the differential form of euler equations breaks down at the location of a contact discontinuity. Despite this, many standard implementations of SPH, including GADGET-2, make no attempt to treat the contact discontinuity in a special way.

Agertz et al. (2007) showed that if left untreated a spurious surface tension arises at the contact discontinuity. This separates particles on either side of the discontinuity, keeping them from interacting, which prevents the growth of instabilities at the interface. The surface tension arises because the density is calculated via an integral formulation, and is therefore smoothed over the discontinuity, while the internal energy is not. This gives rise to a characteristic pressure 'blip' and the pressure is multivalued at the discontinuity (see Fig. 2.2 or Fig. 4 from Hopkins, 2013). Springel (2010) showed that in tests where the internal energy is initially smoothed to ensure the pressure is continuous the instabilities grow as expected.

These results are further confirmed by tests of the Kelvin-Helmholtz instability in isothermal fluids.Price (2008) suggested that that including artificial conductivity can solve the problem by

bringing the system into pressure balance. Thermal conductivity can be included via adding the term

$$\left(\frac{\mathrm{d}u_j}{\mathrm{d}t}\right)_{\mathrm{cond}} = -\alpha_u \sum_i \frac{m_i}{\bar{\rho_{ij}}} v^u_{\mathrm{sig}} (u_j - u_i) \mathbf{r}_{ji} \cdot \boldsymbol{\nabla}_j W_{ij} \tag{2.29}$$

to the energy equation. A good choice for the signal velocity for thermal conduction is

$$v^u_{\mathrm{sig}} = \sqrt{\frac{|P_j - P_i|}{\bar{\rho_{ij}}}}. \tag{2.30}$$

This choice of signal velocity brings the pressure into equilibrium across the contact discontinuity, removing the surface tension, whilst tending to zero in smooth flow away. Price (2008) showed that Kelvin-Helmholtz discontinuities are correctly reproduced in simulations employing such a prescription.

However, artificial conduction has its drawbacks. For example, it is impossible to correctly simulate systems in hydrostatic equilibrium, as in stars, as thermal conduction changes the pressure structure within them, limiting the calculations to less than a dynamical timescale. The problem can be alleviated somewhat, if the signal velocity is modified to include the balance of pressure and gravitational potential. This comes at considerable computational expense, and due to the approximate nature of the self-gravity only partially relieves the issue.

Recently, there has been interest in alternative ways to remove the spurious surface tension, based upon modifying the volume element (Saitoh & Makino, 2013; Hopkins, 2013). This has the advantage that it does not require the addition of a source of unphysical source of dissipation. A generalized volume element can be written as

$$V_i = \frac{X_i}{\sum_j X_j W_{ij}}, \tag{2.31}$$

where $X = m$ gives the usual SPH volume element, m_i/ρ_i. By making a different choice for X, e.g. $X = u$ or $X = P^k$ for some power k, it is possible to construct a conservative form for the momentum equation that reduces the pressure 'blip' across the contact discontinuity. Such formulations have been shown to remove the surface tension, correctly reproduce instabilities and appear to result in a generally more accurate version of SPH (Saitoh & Makino, 2013; Rosswog, 2014).

However, there remains a fundamental difference between these the two approaches. Adding thermal conduction allows the exchange of energy and the associated entropy generation. This allows mixing to occur at the resolution scale (Springel, 2010). Conversely, while modifying the volume element allows instabilities to grow, mixing can only occur on resolved scales.

The two techniques provide a complimentary way of examining the importance of instabilities at the resolution scale. At resolved scales the two techniques produce concordant results in classic tests such as Kelvin-Helmholtz and Rayleigh-Taylor instabilities, and blob destruction tests. At the resolution scale simulations with artificial conduction mimic grid codes, producing a smoother flow than those using modified kernels.

In the majority the simulations presented in this work no attempt to treat the contact discontinuity has been made. However, test calculations are presented using artificial conductivity of the form of equation (2.29) to demonstrate that this does not significantly affect the results.

2.2.3 Self-Gravity

The gravitational field due to a set of point masses is given by $\phi(\mathbf{r}) = -G\sum_i m_i/|\mathbf{r}-\mathbf{r}_i|$. In order to avoid the computational expense from the strong forces as particles approach each other, the force can be softened by considering the mass of each point to be spread out over a finite volume. In this case, the potential can be written as

$$\phi(\mathbf{r}) = G\sum_i m_i \varphi(|\mathbf{r}-\mathbf{r}_i|, \epsilon), \tag{2.32}$$

where ϵ is the softening length. The force is then given by

$$\mathbf{F}_j = -G\sum_i m_i \frac{\mathbf{r}_j - \mathbf{r}_i}{|\mathbf{r}_j - \mathbf{r}_i|}\varphi'(|\mathbf{r}-\mathbf{r}_i|, \epsilon). \tag{2.33}$$

Since $\nabla^2\phi = 4\pi G\rho$, a natural choice for φ is given by $\frac{1}{4\pi}\nabla^2\varphi = W(r)$, or $\varphi'(r,\epsilon) = (1/r^2)\int W(|\mathbf{r}-\mathbf{r}'|,\epsilon)\,\mathrm{d}^3\mathbf{r}'$, where W is the SPH smoothing kernel. Furthermore, for $r > 2h$ the potential reduces to the Newtonian potential, which is not the case for Plummer softening $\phi \propto 1/(r+\epsilon)$ (Dehnen, 2001).

The functional form for φ', for the cubic spline kernel is

$$\varphi'(r,\epsilon) = \begin{cases} 1/\epsilon^2(\frac{4}{3}q - \frac{6}{5}q^3 + \frac{1}{2}q^4) & 0 \leq q < 1, \\ 1/\epsilon^2(\frac{8}{3}q - 3q^2 + \frac{6}{5}q^3 - \frac{1}{6}q^4 - \frac{1}{15q^2}) & 1 \leq q < 2, \\ 1/r^2 & q \geq 2, \end{cases} \tag{2.34}$$

where $q = r/\epsilon$. In GADGET-2 the softening length can either be chosen to be constant, or set to follow the smoothing length of the gas, $\epsilon = h_i$. In the latter case, the expressions presented above do not explicitly conserve momentum, as for $h_i \neq h_j$ the force between two particles $F_{ij} \neq -F_{ji}$, for $r_{ij} < \min(h_i, h_j)$. This can be solved by setting $\epsilon = (h_i + h_j)/2$ or by replacing $\varphi(r_{ij}, \epsilon)$ with $(\varphi(r_{ij}, h_i) + \varphi(r_{ij}, h_j))/2$ in equation (2.33). Furthermore, in order to ensure energy conservation grad-h terms similar to those in equation (2.21) must be derived from the Lagrangian (Price & Monaghan, 2007).

2.2.4 Barnes-Hut Tree

Direct evaluation of the gravitational force at the location of each particle is an $O(N^2)$ process, which is prohibitively expensive and would limit the number of particles that can be used in a simulation to around 10^5. Similarly, evaluation of the hydrodynamic forces is an $O(N^2)$ process, if the neighbours are found by comparing the distance to all particles. In one dimension, neighbour finding can be sped up by pre-sorting the particles, which makes neighbour look up an $O(\log(N))$ process. A similar idea can be applied in higher dimensions, by grouping particles in a tree structure.

GADGET-2 does this using an oct-tree (Barnes & Hut, 1986). The root cell of the tree is a cubical node, which contains all of the particles present. Cells are recursively divided in half along each dimension until there is at most one particle in a cell, at which point the division stops and the cell is known as a leaf cell. By storing the largest smoothing length of each particle in a given cell, neighbours can be found by comparing the region of influence of each cell with the location of a particle, discarding cells that do not overlap the location. Cells which overlap the location are then opened and their sub-cells considered recursively until the leaf cells are reached. This means that the neighbours for a given point can be found in $O(\log(N))$ operations, making the total time

for hydrodynamic forces $O(N \log(N))$.

Similarly, the tree can be used to approximate the gravitational force felt by a particle. The basic idea is to group together particles that are sufficiently far away, approximating the force from the group as force from a single particle at the centre of mass of the group. The leading order error from such a grouping is the quadrupole moment, which is $O(r^{-4})$. In order to calculate the gravitational force in this way the total mass and centre of mass of each cell is stored and the gravitational force is calculated via a tree walk. In GADGET-2 cells are opened according to a criterion relative to their previous acceleration,

$$\frac{GM}{r^2}\left(\frac{\ell}{r}\right)^2 \leq \alpha|\mathbf{a}|, \tag{2.35}$$

where ℓ is the size of the cell, and α is a parameter controlling the force accuracy. The criterion compares a rough estimate of the quadrupole moment of the cell to the total acceleration, with the aim of limiting the absolute force error introduced by each-particle interaction. When the gravitational forces are close to cancelling more nodes are opened, which helps maintain an accurate estimation of the absolute force (Springel, 2005). Using the tree also reduces the total force cost to $O(N \log(N))$, allowing simulations with up to, or more than, 10^7 particles to be feasible with modest resources.

2.2.5 Long Range Gravitional Forces - The Particle-Mesh

For relatively uniform distributions of particles, the calculation of the forces from distant particles can be accelerated by using Fourier transforms. The frequency space gravitational field is split up according to $\tilde{\phi}(k) = \tilde{\phi}^l(k) + \tilde{\phi}^s(k)$, where

$$\tilde{\phi}^l(k) = \tilde{\phi}(k)\exp(-k^2 r_s^2). \tag{2.36}$$

Choosing the cut-off scale, r_s, to be larger than the grid size ensures the Fourier transform provides a good representation of the long range forces. The short range forces can then be calculated using

the tree algorithm, with the modified potential

$$\phi^s(r) = -G\sum_i \frac{m_i}{r_i}\mathrm{erfc}\left(\frac{r_i}{2r_s}\right). \tag{2.37}$$

As $\mathrm{erfc}(x)$ tends rapidly to zero, the contribution to the gravitational field from from distant cells, $r \gg r_s$, can be ignored.

For the long range forces the particles are interpolated to a mesh for Fourier transform using the Cloud-in-Cell method. This considers particles to be spread out over a cube with the same size as the grid cells. The contribution to the density of each cell is calculated by considering the overlapping volumes. The long range potential is calculated by taking the Fourier transform of the density distribution, multiplying by the Fourier space Green function, along with the cut-off and then taking the inverse transform

$$\phi^l(x) = -\frac{1}{(2\pi)^3}\int \frac{4\pi G\tilde{\rho}(k)}{k^2}e^{-k^2r_s^2}e^{ikx}\,\mathrm{d}^3k. \tag{2.38}$$

Once ϕ^l has been calculated, the force at a given cell is calculated using a four point differencing rule

$$\mathbf{F}_x|_{ijk} = -\left.\frac{\partial\phi^l}{\partial x}\right|_{ijk} = -\frac{1}{\Delta x}\left[\frac{2}{3}(\phi_{i+1,j,k}-\phi_{i-1,j,k}) - \frac{1}{12}(\phi_{i+2,j,k}-\phi_{i-2,j,k})\right], \tag{2.39}$$

which is accurate to $O(\Delta x^4)$. The cell-centred force is then interpolated back to the location of the particles using the Cloud-in-Cell algorithm.

2.2.6 Time Integration

Integrating the ordinary differential equations presented above involves finding a trade off between accuracy and computational cost. For large scale simulations the two main constraints on the time-integration method come from the computational expense of evaluating the derivatives and the memory required to store sub-step solutions. The leap-frog, or Störmer-Verlet method, is an explicit second-order method that requires only one force evaluation per time-step and only requires storing the current positions and velocities of particles. The idea is to construct a step which is symmetric under time reversal to ensure conservation of energy. Using the Taylor expansion of $r(t)$

to find $r(t + \Delta t)$ and $r(t - \Delta t)$ we find

$$r(t + \Delta t) = 2r(t) - r(t - \Delta t) + a(t)\Delta t^2. \tag{2.40}$$

Using time-centred differences, we can write the velocities at the half step

$$v(r - \Delta t/2) = \frac{r(t) - r(t - \Delta t)}{\Delta t} \quad \text{and} \quad v(r + \Delta t/2) = \frac{r(t + \Delta t) - r(t)}{\Delta t}. \tag{2.41}$$

Using equation (2.40), the second expression can be written as

$$v(r + \Delta t/2) = v(r - \Delta t/2) + a(t)\Delta t, \tag{2.42}$$

and is a velocity kick received. Equation (2.40) can be re-written as

$$r(t + \Delta t) = r(t) + v(t + \Delta t/2)\Delta t, \tag{2.43}$$

representing a drift in the particles positions. The positions and velocities are updated half a step apart, leaping over each other. The first step has to be treated differently as $v(-\Delta t/2)$ is not defined. This is done through setting $v(\Delta t) = v(0) + a(0)\Delta t/2$.

The leap-frog integrator manifestly conserves energy and angular momentum down to the precision of the equations, which helps to conserve the qualitative properties of the system (Hairer et al., 2006; Rosswog, 2009)

Time-step control

In order to maintain accuracy, the time-step must be limited to ensure the physical quantities do not change much over a single step, i.e. the acceleration must be approximately constant. The step is limited to

$$\Delta t \leq \sqrt{\frac{2\eta\epsilon}{|\mathbf{a}|}}, \tag{2.44}$$

where ϵ is the gravitational softening length and η is a parameter controlling the accuracy. Furthermore, to ensure consistency the time-step must be small enough that information cannot cross the

particle before it has time to respond. The limit

$$\Delta t \leq C \frac{2h}{\max(v_{\rm sig})}, \tag{2.45}$$

is known as the Courant-Friedrichs-Lewy condition, where $v_{\rm sig}$ is the signal velocity and the coefficient, $C < 1$, is usually chosen to be $C = 0.15$.

In the presence of variable time-steps the symplectic nature of the leap-frog integrator is no longer exact. Springel (2005) showed that the kick-drift-kick ordering gives the best results, in which case equation (2.42) becomes

$$v(t + \Delta t_n/2) = v(t - \Delta t_{n-1}/2) + a(t)\frac{\Delta t_n + \Delta t_{n+1}}{2} \tag{2.46}$$

and equation (2.43) becomes

$$r(t + \Delta t_n) = r(t) + v(t + \Delta t_n/2)\Delta t_n. \tag{2.47}$$

Individual particle time-steps

The large dynamic range present in astrophysical systems can result in very different time-steps required for different particles in a simulation. Particles in dense regions typically require much smaller time-steps than their often diffuse surroundings, which can mean that a small fraction of the particles need small time-steps relative to the rest of the system.

Depending on the problem, allowing particles to have their own time-steps can greatly reduce the number of force evaluations. This can speed up the simulations by up to two orders of magnitude (Rosswog & Price, 2007). Using individual time-steps breaks the exact conservation properties, but the errors introduced are small and individual particle time-steps can allow the structure of the whole system to be reproduced more faithfully given the same computational time.

In GADGET-2 the time-steps are constrained such that the total time of the simulation is a power of two multiple of the step size. Furthermore, the steps are kept synchronized, i.e. they are only allowed to increase to a if an integer number of the new step size remains.

When evaluating the tree-based gravity and pressure forces for a subset of the simulation containing n particles, the computation scales as $O(n\log(N))$, where N is the size of the simulation, making force evaluations from the subsets efficient to calculate. However, this is not the case for the long-range forces as the Fourier transforms require all particles to be interpolated to the grid for each step. As the Hamiltonian can be split into long and short-range components

$$H = \sum_i \left(\frac{1}{2}m_i|\mathbf{v}_i|^2 + u_i + \phi_i^s + \phi_i^l\right) = T + H^s + H^l, \tag{2.48}$$

the motion under the long and short-range forces can be evaluated on different time-steps and still preserve the symplectic nature (Springel, 2005). As long-range forces tend to change more slowly, they can then be evaluated less frequently than the short-range forces using an operator-split approach. First the momenta are updated according to equation (2.42), using just the long-range forces. Then, the short-range kicks and drifts (equation (2.43)) are sub-cycled until the next time at which the long-rang force needs to be calculated.

2.2.7 Generating Initial Conditions

One of the key challenges in running accurate SPH simulations is the generation of accurate, self-consistent initial conditions. The difficulty arises since the density is derived from the particle positions and masses. In comparison to grid codes where the density can be specified independently for each cell, modifying the particle positions affects the density of all neighbours. While varying the particle masses is a simple way to reproduce the initial density distribution, this results in noise in the velocity distribution since particles with low mass bounce off high mass particles. Therefore, it is preferred to use a fixed particle mass to vary the particle positions to produce the desired density distribution.

Direct solution involves solving a non-linear system of N equations in $3N$ unknowns, which despite the sparsity of the problem introduced by compact kernels is intractable for moderately large N. Since there are more unknowns than equations, there is considerable flexibility in choosing the distribution of particles for a given density field. For the simplest case of a uniform density field there are two natural choices for distribution of particles, either using a grid-like lattice, or an

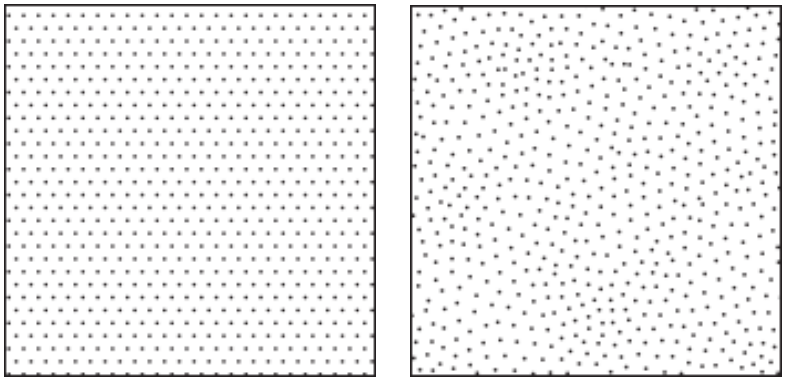

Figure 2.1: Two different representations of a constant density field with equal mass particles using a hexagonal close-packed lattice (left) and an amorphous glass (right) in 2D. [Figures reproduced from Price (2012)]

amorphous glass-like distribution (Fig. 2.1). For grid-like or lattice initial conditions the best choice is a hexagonal close-packed lattice as simple cubic lattices are in general less stable, excepting the use of triangular kernels that severely overestimate the density (Price, 2012; Rosswog, 2014). Grid initial conditions have the advantage of being simple to construct. However, since the grids have preferred directions they behave differently when compressed along or across to these directions. The amorphous nature of glass-initial conditions means they have no preferred direction making them the natural choice for problems with no inherent symmetry.

A uniform glass can be generated by randomly drawing particle positions in a cubic box, but this produces a density distribution that is much more noisy than desired. In order to force the particles towards a noise free distribution the particles can be evolved in time under the effects of a repulsive force. Tests indicate that evolving particles under pressure forces at fixed temperature, or under gravity with the sign of the force reversed results in the particle positions moving asymptotically towards a uniform distribution. In this work, the glasses have been constructed using the gravitational force method, which is available in GADGET-2.

It is then possible to produce a desired density distribution by warping an initially uniform density glass. Since the problems discussed in this work can be built up from a series of spherical mass distributions, it is only necessary to distort the glass in one dimension. If we label the radii of particles in the initial uniform glass such that $r_{i-1} < r_i < r_{i+1}$. The desired radius of the particle, r_i', can be found from the integrated mass distribution, $M(< r) = \int 4\pi\rho(r)r^2 \mathrm{d}r$, such that

$M(< r'_i) = im$, where m is the particle mass. The new particle position is set to $\mathbf{r'_i} = \mathbf{r_i} r'_i / r_i$. This saves the glass-like nature of the underlying particle distribution resulting in a smooth representation of the density as long as the change in density over a smoothing length is not too large.

Once the density distribution has been set, the internal energy and velocity can be set according to the position. In the case a system which is in hydrostatic equilibrium, as in the case of star, the particle distribution needs to be relaxed. The relaxation is achieved by evolving the star in isolation, with a damping force applied. The damping force is applied by reducing the velocity by a factor of $1 + \lambda$ after each force evaluation. The resulting velocity kick is

$$\mathbf{v}_{n+1/2} = \frac{\mathbf{v}_{n-1/2} + \mathbf{a}_n \Delta t}{1 + \lambda}, \tag{2.49}$$

which brings the particles slowly into equilibrium with $\mathbf{v} \to 0$ as $t \to \infty$. The damping parameter $\lambda = 0.5$ and the velocities are monitored to ensure they do not become too large. During the relaxation the star reaches a stable equilibrium and the noise in the density distribution is significantly reduced.

2.2.8 Shock tube test

The shock tube test (Sod, 1978) has become a standard problem to test the ability of hydrodynamic codes to follow basic physical phenomena. The test begins with two regions of an ideal gas separated by a discontinuity and initially at rest. On one side of the discontinuity ($x < 0$) the gas is initially in a high-pressure, high-density state ($P_l = 1$, $\rho_l = 1$), while on the other side ($x > 0$) the gas is in a low-pressure and low-density state ($P_r = 0.1795$, $\rho_r = 0.25$). The adiabatic index, $\gamma = 5/3$. The solution evolves in a self-similar manner and contains a shock, contact discontinuity and rarefaction wave.

The shock tube is set up in three dimensions using periodic boundary conditions in the y and z directions. Figure 2.2 shows the results of the test for low resolution simulations using a uniformly spaces grid (red) and glass-like (blue) initial conditions. The glass-like initial conditions are an amorphous representation of a constant density medium. The glass-like initial conditions are created by drawing particle positions randomly and evolving them under gravity with the sign of

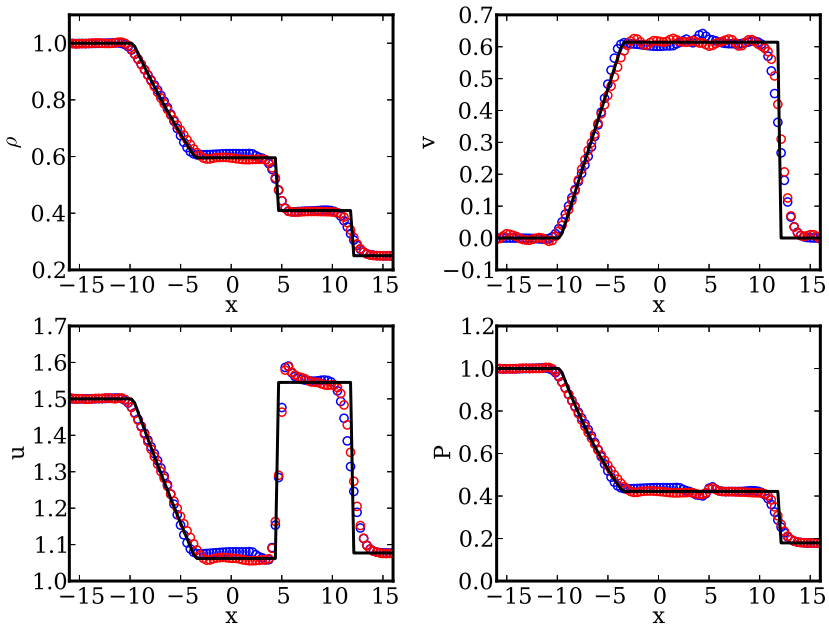

Figure 2.2: Low resolution shock tube test at $t = 7.5$, with mean particle spacing 1/3 in the high density region. The panels show the density, velocity, internal energy and pressure, which are evaluated using the kernel sum over neighbouring particles. The black line is the analytical solution. The blue circles correspond to cubic grid initial conditions and the red circles to glass initial conditions. The shocks are broadened as expected but the main features are reproduced.

the force reversed, which drives them into a uniform distribution.

The resolution in the high density region is 3 particles per unit length, corresponding to a linear resolution of roughly 100 particles over the range $-20 < x < 20$. Both simulations reproduce the main features of the solution, with the discontinuities spread over a few smoothing lengths. The simulation with glass initial conditions is noticeably more accurate in the region between the end of the rarefaction wave ($x \approx -4$) and the contact discontinuity ($x \approx 4.5$). The pressure blip at the contact discontinuity occurs as excess thermal energy is generated before the shock is resolved. This can be removed, either by smoothing the initial discontinuity or by using an artificial conductivity (Price, 2008).

The additional noise in the post-shock velocity distribution arises as the shock compresses the particles anisotropically. Small perturbations in the positions cause the particles to re-mesh to a more isotropic distribution, giving rise to the noise in the velocity distribution. This is a direct result of using the conservative form of the momentum equation (2.21), which helps to maintain

particle order. In most cases this noise is not a problem. In cases where it important, it can be reduced by using a smoother kernel, for example the quintic spline kernel (Price, 2012).

2.2.9 Sedov Blast Wave

A more stringent test of a code's ability to follow shock is based upon Sedov's point explosion (Sedov, 1959). The test involves the expansion of a strong shock into a cold medium, making it an appropriate test case for supernova remnants and novae. A large amount of energy is injected into a small volume at the centre of a uniform medium. The blast wave evolves self-similarly, with the radius, R, given by

$$R(t) \approx 1.1527 \left(\frac{E}{\rho}\right)^{1/5} t^{2/5} \tag{2.50}$$

in 3D for a gas with adiabatic index $\gamma = 5/3$, where E is the energy injected and ρ is the background density.

The SPH simulation is set up using $N = 128^3$ particle glass in a unit box. The particle mass $m = 1/N$, is set so that $\rho_0 = 1$. The thermal energy in the background is chosen to be $u = 10^{-3}$, such that it remains negligible throughout the simulation and $E = 1$. Following Durier & Dalla Vecchia (2012), the energy is smoothed over a number of particles ($N_{\rm ngb} = 64$) in the centre of the computational domain. The particle energies, u_i, are set using the smoothing kernel,

$$u_i = \frac{E}{m_i} \frac{W(r_i, h)}{\sum_i W(r_i, h)}, \tag{2.51}$$

where the smoothing length, $h = 0.5 \max(r_i)$, such that the kernel drops to zero at the outermost particle. Alternatively, the energy can be injected by giving the particle radial velocities, $v_i = \sqrt{2u_i}$, which is arguably more appropriate for calculations of supernova remnants. Smoothing the initial energy makes the test less severe, but reflects the initial conditions used in calculations supernova remnants, where the supernova ejecta are resolved.

Fig. 2.3 shows the evolution of the Sedov solution for a simulation with viscous parameter $\alpha = 3$. The high viscosity is needed to damp out the post-shock oscillations for the high Mach number shock, which can be seen in velocity at $t = 0.02$ and $t = 0.04$. If a more traditional value

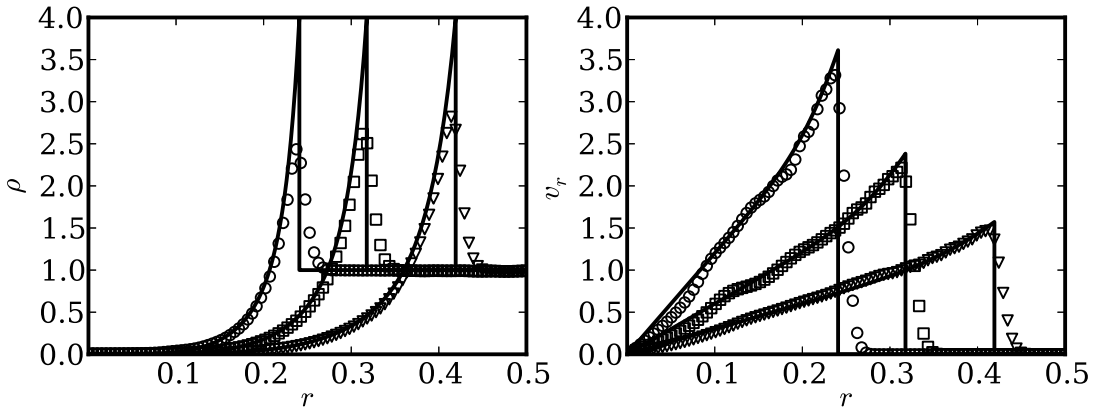

Figure 2.3: Sedov solution evolution with viscous parameter $\alpha = 3$, at times $t = 0.02, 0.04$ and 0.08 (circles, squares, triangles).

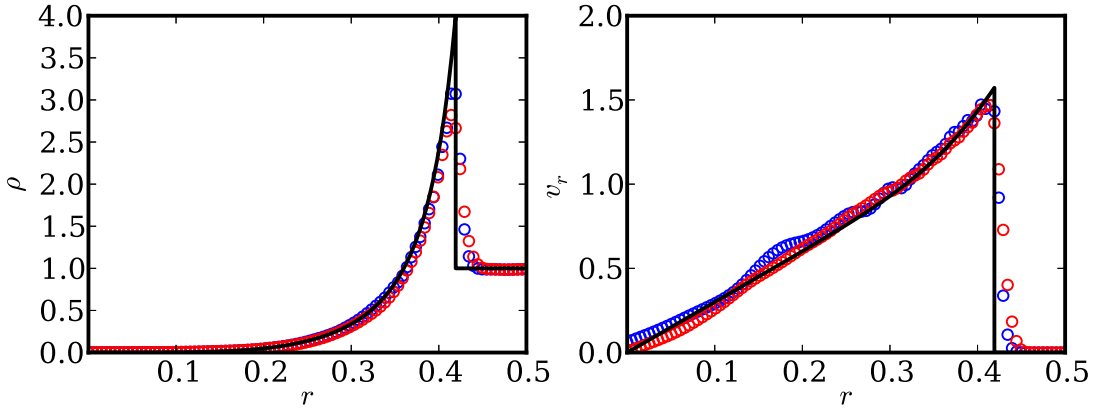

Figure 2.4: Sedov solution at $t = 0.08$ for simulations with $\alpha = 1.2$ (blue) and $\alpha = 3$ (red). The higher viscosity is needed to remove the post-shock oscillations, at the expense of further broadening of the shock.

viscosity parameter is used the shock in narrower and a higher peak density is reached, but the oscillations survive (Fig. 2.4).

In order to achieve the accuracy in the solution presented in Fig. 2.3 the maximum allowed time-step has been kept to $\mathrm{d}t = 10^{-5}$. The need for such a small time-step arises due to the use of individual particle time-steps. In the cold medium, the time-steps are limited by the Courant condition $\mathrm{d}t = C(h/c_s) \approx 10^{-2}$., which are much longer than those required by particles in the shock front (10^{-6}). This results in a violation of Newton's third law (Saitoh & Makino, 2009), as the cold medium is unable to react to the passage of shock front, resulting in particle penetration and violation of energy conservation.

The problem arises because particles on long time-steps are not able to react to the changing environment. Limiting the maximum time-step, or using the same step for all particles is able to overcome this difficulty, though at considerable computational cost (Durier & Dalla Vecchia, 2012). A natural solution to this problem is to redo the steps with the step-size reduced when particles find that they need smaller step sizes at the end of the step than the beginning. For large simulations such iterations are too costly, therefore Saitoh & Makino (2009) advocate allowing particles to reduce their step size mid-step. While this does not explicitly conserve energy, as long as the time-steps are reduced sufficiently early the error can be kept to reasonable levels. Limiting the time-step of a particle to be no more than a few times that of any of it's neighbours allows the particles to react before the shock front reaches them and provides the required accuracy at much lower computational cost than using iteration or global time-steps (Saitoh & Makino, 2009; Durier & Dalla Vecchia, 2012).

2.3 Radiation

In order to test theories we must be able to compare the simulations to observations, which requires a way of linking the light received with quantities like density, velocity and temperature that naturally arise in simulations. In the case of resolved objects, the kinematic structure or morphology can often be utilized directly. However, for unresolved objects we need to link the simulations to spectra or spectral features. The interaction between radiation and the gas is governed by the radiation-

transfer equation

$$\left(\frac{1}{c}\frac{\partial}{\partial t} + \mathbf{n}\cdot\boldsymbol{\nabla}\right) I(\mathbf{x}, t, \mathbf{n}, \nu) = \eta(\mathbf{x}, t, \mathbf{n}, \nu) - \chi(\mathbf{x}, t, \mathbf{n}, \nu) I(\mathbf{x}, t, \mathbf{n}, \nu) \tag{2.52}$$

where I is known as the specific intensity, and is the energy flux per unit solid angle, per unit frequency, ν, in the direction, $\mathbf{n}$. The emissivity, η, includes spontaneous and stimulated emission, as well as scattering, and $\chi = \kappa + \sigma$ is the sum of the absorption coefficient, κ, and the scattering coefficient, σ.

Besides the immediate difficulty involved in solving the full six-dimensional radiative transfer equation, the problem is much worse as in general η and χ depend on the local radiation field, I. The problem can usually be solved iteratively, by calculating the radiation intensity for given η and χ, and updating η and χ based upon the new intensity.

In three spatial dimensions computing the full solution is extremely computationally intensive, therefore two principal simplifications are made. Scattering is neglected, and the emissivity and opacity are not solved for along with the radiation intensity, removing the need for iterative solution. Under these assumptions the radiative transfer equation can be reduced to an integral along rays through the medium

$$\frac{\mathrm{d}I_\nu(s)}{\mathrm{d}s} = \eta_\nu(s) - \chi_\nu(s) I_\nu(s), \tag{2.53}$$

where s denotes the position along rays in the medium and time-dependence has been neglected. The solution can be written in terms of the optical depth, $\mathrm{d}\tau_\nu = \chi_\nu \,\mathrm{d}s$,

$$I_\nu(s_1) = I_\nu(s_0) e^{-(\tau_\nu(s_1) - \tau_\nu(s_0))} + e^{-\tau_\nu(s_1)} \int_{\tau_\nu(s_0)}^{\tau_\nu(s_1)} e^{\tau_\nu} \frac{\eta_\nu}{\chi_\nu} \,\mathrm{d}\tau_\nu. \tag{2.54}$$

In order to calculate flux seen by an observer in a given direction, equation (2.54) is integrated over all lines of sight to the observer. Therefore, line profiles can be calculated by solving a four-dimensional problem for a few representative directions, rather than the full six-dimensional problem.

2.3.1 Implementation

As SPH simulations can cover a dynamic range in density of many orders of magnitude, solving the radiative-transfer equation efficiently requires the integration to follow the local resolution of the simulation. This can be achieved by recursively sub-dividing regions until the cell size is a given fraction, f_h, of the minimum smoothing length of particles which overlap the cell. For simplicity, this is done only in the plane of the sky. The radiative transfer equation can then be solved along the centre of the cell, under the approximation that the conditions are constant across the cell.

Integration of equation (2.54) along a ray is done using an algorithm based upon Kessel-Deynet & Burkert (2000). From the current point on a ray, s_0, the next point, s_1, is selected by considering each of the SPH neighbours, i, to s_0. The angle between the line that goes through each neighbour, i and s_0 is calculated, and the particle, j, with the smallest angle is chosen. The point j is then projected onto the ray, giving the new point, s_1. This method correctly finds steep density gradients, whereas using a criterion based upon the local smoothing length can result in too large steps when going from a less dense to more dense region. The algorithm has also been modified to allow taking steps which are a fraction of the step given by the above criteria, which is usually taken to be the same as f_h.

In the presence of steep gradients care has to be taken when integrating equation (2.54). A particular case of this occurs when the ray leaves a dense, optically thick region and enters an optically thin region. Upon leaving the optically thick region the intensity is given by $I_\nu = \eta_\nu/\chi_\nu$, whereas in the optically thin region the intensity is roughly $I_\nu = I_{\nu 0} + \int \eta_\nu \, \mathrm{d}s$. Sharp transitions are spread out over roughly a smoothing length by the SPH interpolation of physical quantities, which helps alleviate the problem. Furthermore, the smoothing also means that the emissivity and opacity can be approximated to be linear across the cell, which allows analytical solutions to equation (2.54) to be used removing the need for small integration steps.

In the case of a line profile, the emissivity and opacity can be written as

$$\kappa_\nu(x) = \kappa(x)\phi(\nu', \Delta\nu_\mathrm{D}) \tag{2.55}$$

$$\epsilon_\nu(x) = \epsilon(x)\phi(\nu', \Delta\nu_\mathrm{D}), \tag{2.56}$$

Parameter	Value
η_0	1000
η_1	10
κ_0	1000
κ_1	50
Δx	0.1
Δv_D	20

Table 2.1: Parameters for ionization front test, given by equations (2.57) and (2.58).

where $\phi(\nu, \Delta\nu_\mathrm{D})$ is the Doppler frequency, ϕ is the intrinsic line profile, and $\nu' = \nu(1 - \frac{v(x)}{c})$ is the frequency in the rest frame of the gas. Ordinarily a Doppler profile or Voigt profile is used. As the profiles decay rapidly away from the line centre $|\nu' - \nu_0| > \Delta\nu_\mathrm{D}$, the contribution to intensity at a given frequency can change rapidly across a cell. Changing the integration variable to $\mathrm{d}q = \phi(\nu')\,\mathrm{d}s$, and assuming η, κ are linear in q give better conservation properties, but can cause the profile to be stepped (see Fig. 2.7).

2.3.2 Radiation Tests

Ionization Front

The first test mimics the conditions seen in an ionization front, along with the changes in a line profile. The source function, $S_\nu = \eta_\nu/\kappa_\nu$, drops across a region, causing the line to go from emission into absorption. The emissivity and opacity, are taken to be

$$\eta = \frac{\eta_0 + \eta_1}{2} + \frac{\eta_1 - \eta_0}{2} \tanh\left(\frac{x}{\Delta x}\right), \tag{2.57}$$

$$\kappa = \frac{\kappa_0 + \kappa_1}{2} + \frac{\kappa_1 - \kappa_0}{2} \tanh\left(\frac{x}{\Delta x}\right), \tag{2.58}$$

which are modified by a Doppler profile

$$\phi(v) = \frac{1}{\sqrt{\pi}\Delta v_\mathrm{D}} \exp\left(-\frac{(v - v_0)^2}{\Delta v_\mathrm{D}^2}\right) \tag{2.59}$$

of width $\Delta v_\mathrm{D} = 20\,\mathrm{km\,s^{-1}}$. The spatial domain is $-1 \leq x \leq 1$, with $I_\nu(x = -1) = 0$. The gas is assumed to be at rest ($v_0 = 0$), and the constants used are provided in Table 2.1.

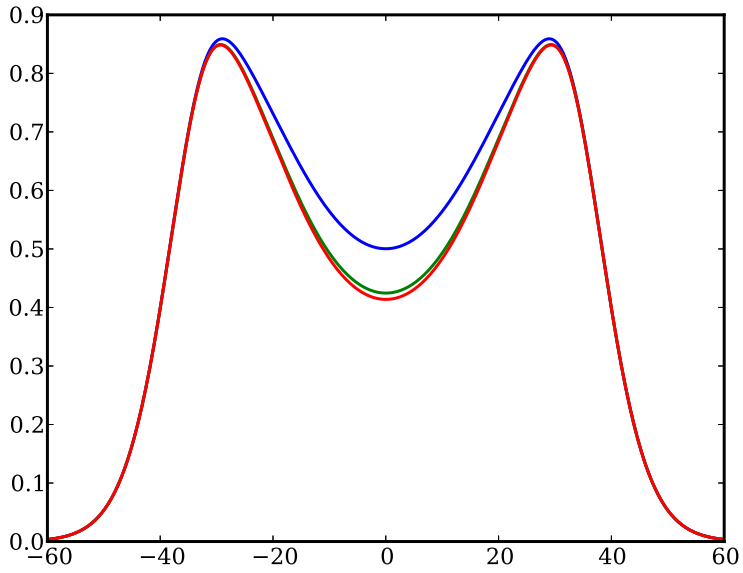

Figure 2.5: Ionization front problem, with a spatial resolution of 5 (blue), 10 (red) and 100 (green) points. The differences occur due to the different effective widths of the ionization front that arise due to the coarse sampling. Prior to reaching the transition near $x = 0$, the profile is given by $I_\nu = (\eta_0/\kappa_0)(1 - \exp(-\tau_0\phi(v))$, which saturates in the line centre. For $x > 0$, the line centre is absorbed as $\eta_1/\kappa_1 < \eta_0/\kappa_0$.

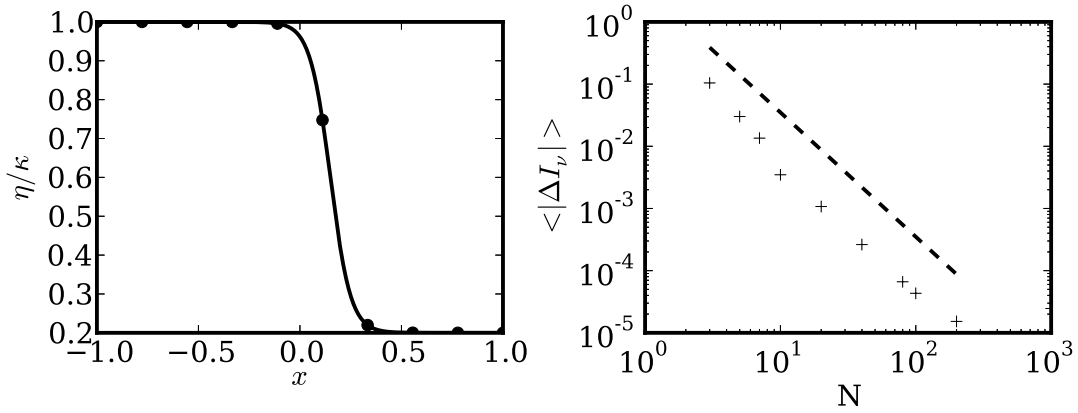

Figure 2.6: *Left:* Source function sampling points for the ionization front problem. The points selected are the sampling points for $N = 10$. *Right:* Convergence of the mean error for the ionization front problem. The convergence rate is close to $O(N^{-2})$, as shown by the dashed line.

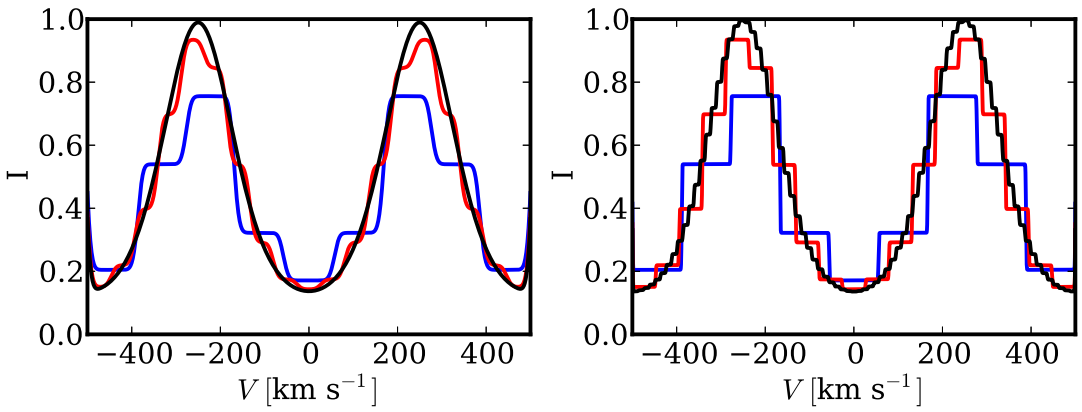

Figure 2.7: Line transfer test with a large velocity gradient. The different lines show the profiles using different numbers of cells used: 10 (blue), 20 (red) and 80 (black). *Left*: $T = 10^4\,\mathrm{K}$, $\Delta v_\mathrm{D} \approx 12\,\mathrm{km\,s^{-1}}$; *Right*: $T = 10^2\,\mathrm{K}$, $\Delta v_\mathrm{D} \approx 1.2\,\mathrm{km\,s^{-1}}$.

The profile is calculated for a range of models, in which η and κ have been sampled at a varying number of points. Fig. 2.5 shows the convergence to the profile created by the ionization front. The convergence is slowest in the line centre, as this is where the optical depth through the transition region is highest. The $N = 10$ profile is already close to exact solution with a maximum error of less than two per cent, which shows that a few points around a steep gradient is sufficient to capture the main properties (Fig. 2.6). The convergence is roughly $O(N^{-2})$, as expected for linear interpolation.

Velocity Test

In a supersonic gas the bulk fluid velocities can be much larger than the local Doppler velocity ($v > v_\mathrm{D}$, for Mach number, $M > \sqrt{10/18}$ in a gas with $\gamma = 5/3$), in which case the strength of the line profile can change significantly across a cell. The assumption that $\Delta v_\mathrm{D}/\frac{\mathrm{d}v}{\mathrm{d}r}$ is larger than the typical length scale over which the fluid properties change forms the basis of the Sobolev method (Sobolev, 1947).

The code's performance in such a scenario can be tested by considering a medium with a large, constant velocity gradient. Emission is neglected, only the absorption against a uniform source, $I_\nu(0) = 1$, is considered, with $\kappa(x) = \kappa_0 \cos^2(2\pi x)$. The velocity varies from $-500 < v < 500\,\mathrm{km\,s^{-1}}$ over $0 < x < 1$ and κ_0 is chosen such that the optical depth is close to saturation at $x = 0$.

The profiles calculated using a variety of spatial resolutions are shown in Fig. 2.7. While the total optical depth is conserved to within a few per cent, the line profile becomes boxy when $\Delta v > \Delta v_{\rm D}$. This can be understood by considering

$$s = \int_{r_0}^{r_1} \phi \left(v(0) + \frac{{\rm d}v}{{\rm d}r} r \right) dr = \Delta v_{\rm D} \frac{{\rm d}r}{{\rm d}v} \int \phi(x) dx. \tag{2.60}$$

In this case when $\delta r \frac{{\rm d}v}{{\rm d}r} \gg \Delta v_{\rm D}$, the integral is close to unity if the signs of $x(r_0)$ and $x(r_1)$ differ, or zero if they are the same. For the $T = 10^4\,{\rm K}$, 80 points is enough for $\Delta v_{\rm Doppler} \approx \Delta v$, and the resulting profiles are smooth, with the maximum error at around 0.5 per cent. For low temperatures, such a criterion can be very strong. However, the $T = 10^2 K$ case shows that as long as the underlying velocity distribution is well sampled then the resulting line profile is close to the real profile. In this case it can be better to approximate the line profile as a δ-function, which results in a smooth profile.

Infall Test

A final test, which considers emission from gas infalling spherically in a potential due to a point mass is used to explore the ability of the code to reproduce line profiles from SPH distributions. The density is chosen to give a constant accretion rate

$$\rho(r) = \frac{\dot{M}}{4\pi r^2 |v(r)|}. \tag{2.61}$$

Pressure is neglected in calculating the velocity, $v = -\sqrt{2GM/r + 2E_0}$, and E_0 is sum of the gravitational and kinetic energy, which is a constant. The emission is chosen to be proportional to the Case B recombination rate for hydrogen $\eta = f n_{\rm H}^2 \alpha_B(T) h\nu$, with $f = 0.5$, which is roughly consistent with Hα emission (Storey & Hummer, 1995). Absorption is neglected for simplicity, as in this case the analytical expression for emission from a shell can be used to calculate the luminosity at a given frequency

$$\frac{{\rm d}L_\nu}{{\rm d}r} = \frac{\pi r^2 \eta(r) c}{\nu v(r)} \left({\rm erf}(x_1) - {\rm erf}(x_0) \right), \tag{2.62}$$

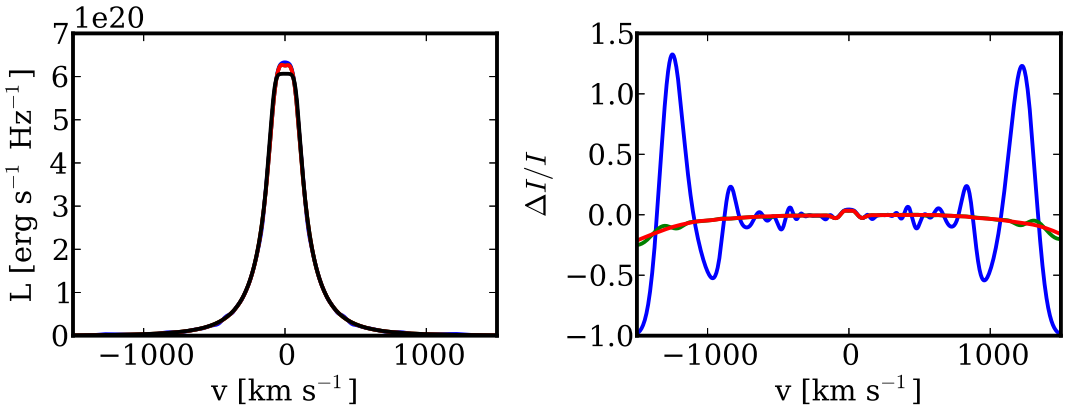

Figure 2.8: *Left*: Line profile from a gas in spherical infall. *Right*: Relative error in the line profile for different calculations. In each case the gas is represented by the same sphere taken from a 64^3 SPH glass. The black line gives the semi-analtyical solution. The coloured lines give the solution for different resolution parameters (see text), 2 (blue), 0.5 (green), 0.2 (red).

where $\mathrm{erf}(x)$ is the error function and $x_{1/0} = \frac{\nu(1\pm v/c)-\nu_0}{\Delta\nu_\mathrm{D}}$, where ν_0 is the rest frame frequency of the line.

The infalling gas profile is represented by equal mass SPH particles. The density distribution is calculated by cutting a sphere from a 64^3 or 128^3 glass, and then warping the particle radii to give the desired mass distribution. The density and smoothing lengths are calculated using GADGET-2, and the velocities are set according to the free-fall velocity. The temperature evolution is assumed to be adiabatic, and calculated assuming $T = 5 \times 10^4\,\mathrm{K}$ at the outer radius.

The line profiles are then calculated using a range of different grid resolutions $f_h = 2$, 0.5 and 0.2, which are shown for the 64^3 grid in Fig. 2.8. The profiles show good general agreement with the analytical solution, apart from near the centre of the line and in the line wings, where the error is higher. The line profile converges for $f_h = 0.5$, with little improvement seen for $f_h = 0.2$.

The error in the line wings occurs due to the relatively low mass at high velocities, reflecting the deviation from the true density that is present in the SPH discretisation. The error near the line centre arises due to edge effects in the mass distribution. The finite smoothing length at the outer edge means the particles contribute to a non-zero density beyond the edge of the mass distribution, which results in an over-estimation of the line profile from the outermost particles. For the 128^3 case, the errors are reduced to a few per cent, which is the typical error due to the SPH discretisation.

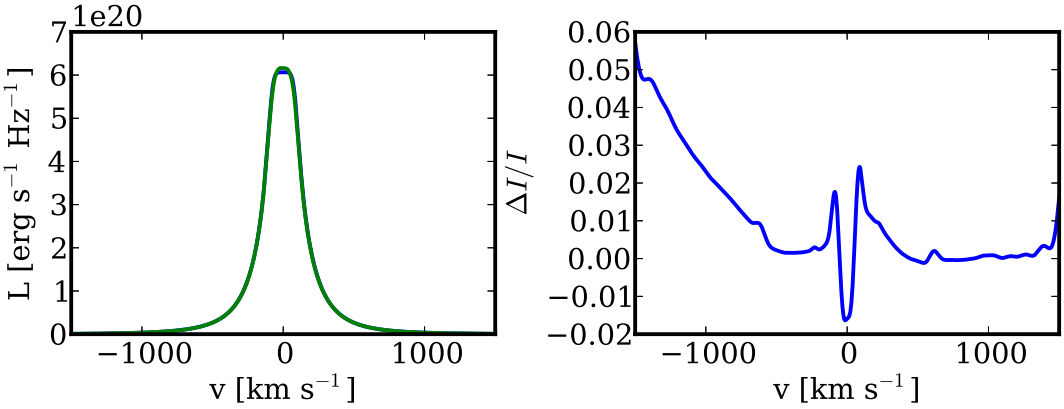

Figure 2.9: Infall problem using 128^3 particles. *Left*: Line profile; *Right*: Relative error.

Chapter 3

Supernova-Companion Interaction and Stripped Hydrogen

The presence of a Roche-lobe filling companion star in the single degenerate channel for Type Ia supernovae has interesting prospects for the structure of supernovae and their remnants, as well as the companion star. Considerable effort has been put into examining the effects a Type Ia supernova (SN Ia) has on its companion star, including analytic models (Wheeler et al., 1975), and several computational studies (e.g. Marietta et al., 2000), although they have only recently begun to use model stars that have been evolved with appropriate mass loss (Pan et al., 2012) and binary evolution (Liu et al., 2012). Even so, there has been little focus on investigating systems that correspond to the archetypal systems in our Galaxy.

In this chapter models for a potential companion for Tycho's supernova and the galactic recurrent nova RS Ophiuchi are constructed. The interaction of the supernova and companion star are calculated using SPH, as described in Section 2, along with the final structure of the ejecta that eventually freezes in. Finally the observational prospects are considered, taking into account the structure from the simulations.

3.1 Initial models

Realistic stellar models for the companion were set up using a stellar evolution code that takes into account mass loss due to the binary evolution (Podsiadlowski et al., 2002). The stellar models have been chosen to be analogues to well known Galactic systems. The first is a $0.842M_{\odot}$, $9.3R_{\odot}$ sub-giant star (SG1), which has been chosen to be a potential progenitor for Tycho's Supernova Remnant. Extensive searches for surviving companions have been conducted for Tycho's SNR (Ruiz-Lapuente et al., 2004; Kerzendorf et al., 2009, 2013), and while there is no clear case for a surviving companion the one candidate is Tycho-G. In order to explain its low rotational velocity the companion star's envelope must have been stripped by the supernova; therefore, it must have a large radius and weakly bound envelope (Kerzendorf et al., 2009).

The second model is a red giant (RG1), which has been chosen to represent the companion star to the recurrent-nova RS Ophiuchi (RS Oph). RS Oph is an excellent candidate for a Type Ia supernova progenitor as the low mass and high velocity of the nova ejecta point to a white dwarf that is close to the Chandrasekhar mass (Yaron et al., 2005). Spectroscopically determined orbital parameters give a mass ratio $q = 0.59$ (Brandi et al., 2009), which gives a mass for the red giant of $\sim 0.8M_{\odot}$. The radius of this star is $100R_{\odot}$, which is consistent with the star being close to filling its Roche lobe; as a period of 453.6 days implies Roche-lobe radius of $R_{\rm RL} \approx 110R_{\odot}$. The mass stripped from a red giant depends only weakly on the binary separation (Pan et al., 2012); therefore, an uncertainty of roughly 10 per cent in separation should have little effect on the simulations.

The density and pressure from the stellar models are mapped onto a 3D glass, using a constant particle mass of $2 \times 10^{-6}M_{\odot}$. An extra model of the sub-giant (SG2) has been constructed using a smaller particle mass ($10^{-6}M_{\odot}$) to verify the resolution is sufficient. The internal energy of the particles is set according to the pressure and density from the stellar model. This results in a different temperature structure for the star as the SPH calculation uses an ideal gas equation of state with $\gamma = 5/3$. The smoothing length is set so that each particle has 64 neighbours and self-gravity is calculated using the tree with adaptive softening lengths. For the main calculations no artificial conduction is added. The resulting structure is shown in Fig. 3.1. The SPH model of the star is then relaxed to remove any initial noise from the set-up and ensure that the initial model is

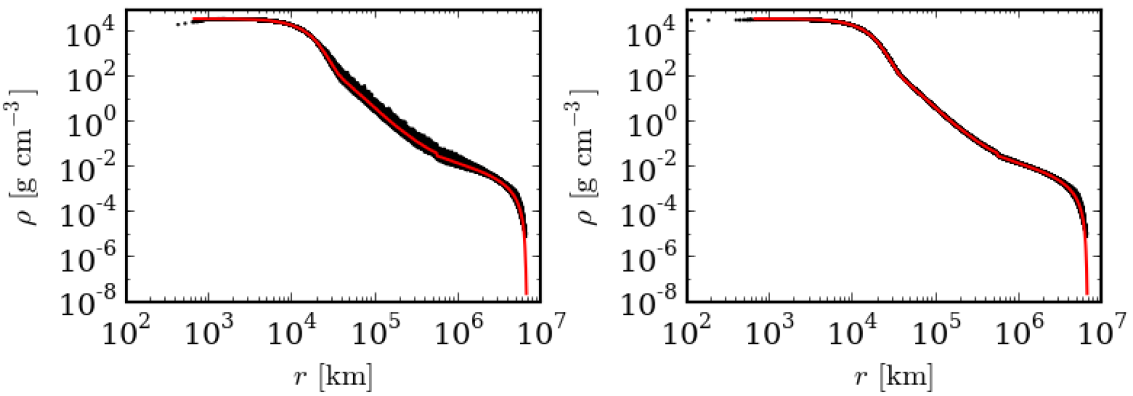

Figure 3.1: SPH model of stellar density profile for model RG1, using a particle mass of $10^{-6}M_{\odot}$. *Left*: Before relaxation; *Right*: After relaxation the density distribution is considerably less noisy.

stable.

The red giant has a core that is strongly bound and much smaller than the total size of the star, $R_{\rm core}/R \approx 10^{-4}$. Modelling the full star is prohibitively expensive as the very high densities in the core result in tiny time-steps relative to particles in the envelope. To overcome this difficulty, the core of the star is removed and replaced with a point mass. The core is filled with gas of the same density at its edge, and pressure set so that the core supports the atmosphere. The point mass is allowed to move under the force of gravity, but pressure forces are neglected.

Prior to the supernova the companion star is close to filling its Roche-lobe. In this case the stellar structure is altered by the presence of the companion. Liu et al. (2012) found that for main-sequence stars the effects are negligible; much more mass is stripped than is present in the layers where the structure is significantly perturbed. The evolved sub-giant and red giant stars presented here are considerably more centrally condensed, and have more extended envelopes than those presented by Liu et al. (2012).

Perturbation theory (Sterne, 1939; Schwarzschild, 1965) can be used to estimate the distortion of the envelope by the white dwarf. Using Eggleton's formula for the separation at which the star fills its Roche-lobe (Eggleton, 1983), the distortion is a few per cent in the outer layers. The distortion at the base of the stripped region, which is much smaller than the distortion at the edge of the star, is more important for determining the stripped mass. Taking the Wheeler et al. (1975) estimate for stripped mass, $M_{\rm Wh}$, the important radius can be estimated by considering the radius, $r_{\rm Wh}$

Table 3.1: Key stellar model parameters.

Model	$n_{\rm star}$	$M_{\rm tot}$	$M_{\rm core}$	$M_{\rm strip}$	$M_{\rm strip}/M_{\rm env}$	$M_{\rm est}/M_{\rm env}$
SG1	421155	0.842	0.31	0.46	0.87	0.86
SG2	844490	0.842	0.31	0.48	0.90	0.86
RG1	190552	0.8	0.42	0.37	0.97	0.97

$n_{\rm star}$ is the number of SPH particles used in the star, $M_{\rm tot}$ is the total stellar mass, $M_{\rm core}$ is the mass of the core, $M_{\rm strip}$ the mass stripped by the SN ejecta and $M_{\rm est}$ is the mass stripped as estimated by the method Wheeler et al. (1975). The particle mass is the same for each of these stars, $m_{\rm part} = 2 \times 10^{-6} M_\odot$, except for SG2, for which $m_{\rm part} = 10^{-6} M_\odot$.

,at which the mass external to that radius is $M_{\rm Wh}$. The distortion at this radius, $\delta r/r < 10^{-3}$, therefore the change in structure can be neglected.

The W7 model (Nomoto et al., 1984) is used to represent the Type Ia supernova. The model has $M_{\rm SN} = 1.38 M_\odot$ and kinetic energy, $E_{\rm kin} = 1.37 \times 10^{51}$ erg. The density and velocity structure are taken from 31 days after explosion, once the supernova is in free expansion and the evolution is self similar. The SPH representation is constructed by radially warping a glass, using the same particle mass as the star. The radius is then rescaled such that the outer edge of the supernova is almost touching the companion star. The density structure is not relaxed. Although this results in some noise in the density distribution, the supernova initial conditions are not in equilibrium so relaxation is not critical. The internal energy is set to 10 per cent of the kinetic energy. As long as the thermal energy is not too large the choice does not affect the dynamics, which are dominated by ram-pressure.

3.2 Supernova - Companion Interaction

The evolution of the supernova-companion interaction for the SG1 model is shown in Fig. 3.2. The evolution for the red-giant model is similar and is therefore not discussed in detail. The simulation uses a total of 1.1 million particles to represent the star and supernova.

Initially the companion star is in equilibrium, located at $x = -27.8$. The supernova is centred on the origin. When the supernova reaches the companion star, it drives a shock through the envelope. The shock travels fastest through the low-density envelope, causing it to wrap around the core. As

the shock travels towards the core it is slowed due to the steep density gradient and eventually stalls. The outer layers of the envelope are stripped immediately by the passage of the shock. By $t = 15000\,\mathrm{s}$ the supernova and stripped companion material have reached free expansion and the evolution has become approximately self-similar, with $v \propto r$.

The final structure of the of the model is shown in Fig. 3.3. There remains a hole in the ejecta in the region shadowed by the companion star, as was noted by Marietta et al. (2000). The hole is surrounded by a bow shock, which appears as a high density arc. The bow shock consists mainly of the supernova ejecta that was blocked by the companion star, along with a small amount of entrained companion material. The majority of the stripped companion material remains at low velocity and does not mix with the supernova ejecta, as is shown in Fig. 3.3.

The supernova strips $0.48 M_{\odot}$ from the sub-giant star, which is roughly 90 per cent of the envelope. This is much higher than $0.2 M_{\odot}$ reported by Marietta et al. (2000) for their sub-giant model (HCVL), although close to analytical estimate (see Table 3.1). There are key differences between the model SG1 and the HCVL model, which was simply an un-evolved star with its envelope removed. The sub-giant presented here is evolved consistently accounting for mass-loss, and is both lower in mass and larger in radius. This means the envelope is less strongly bound, which explains the greater amount of mass stripped. Of the more recent calculations, only Liu et al. (2012) take into account the full binary evolution. The closest match to the SG1 star is their model ms_20a, which is a considerably more compact sub-giant with a radius of $1.7 R_{\odot}$. They find the supernova strips more mass than from the sub-giant than any of their other models, albeit only $0.18 M_{\odot}$.

The supernova strips the entire envelope of the red giant star. This is expected as the envelope is more weakly bound than the sub-giant envelope and is consistent with previous work (Marietta et al., 2000; Pan et al., 2012). As only ~ 6000 particles remain bound to the envelope of the RG1 model the remaining structure is poorly resolved. Therefore the entire envelope can be considered to be stripped, and therefore the actual mass of the stripped material is a lower limit. However, due to the steep density gradient in the core this is likely to be a good estimate. The value also agree well with the estimated mass stripped based upon Wheeler et al. (1975), which uses the entire star; adding further weight to the argument.

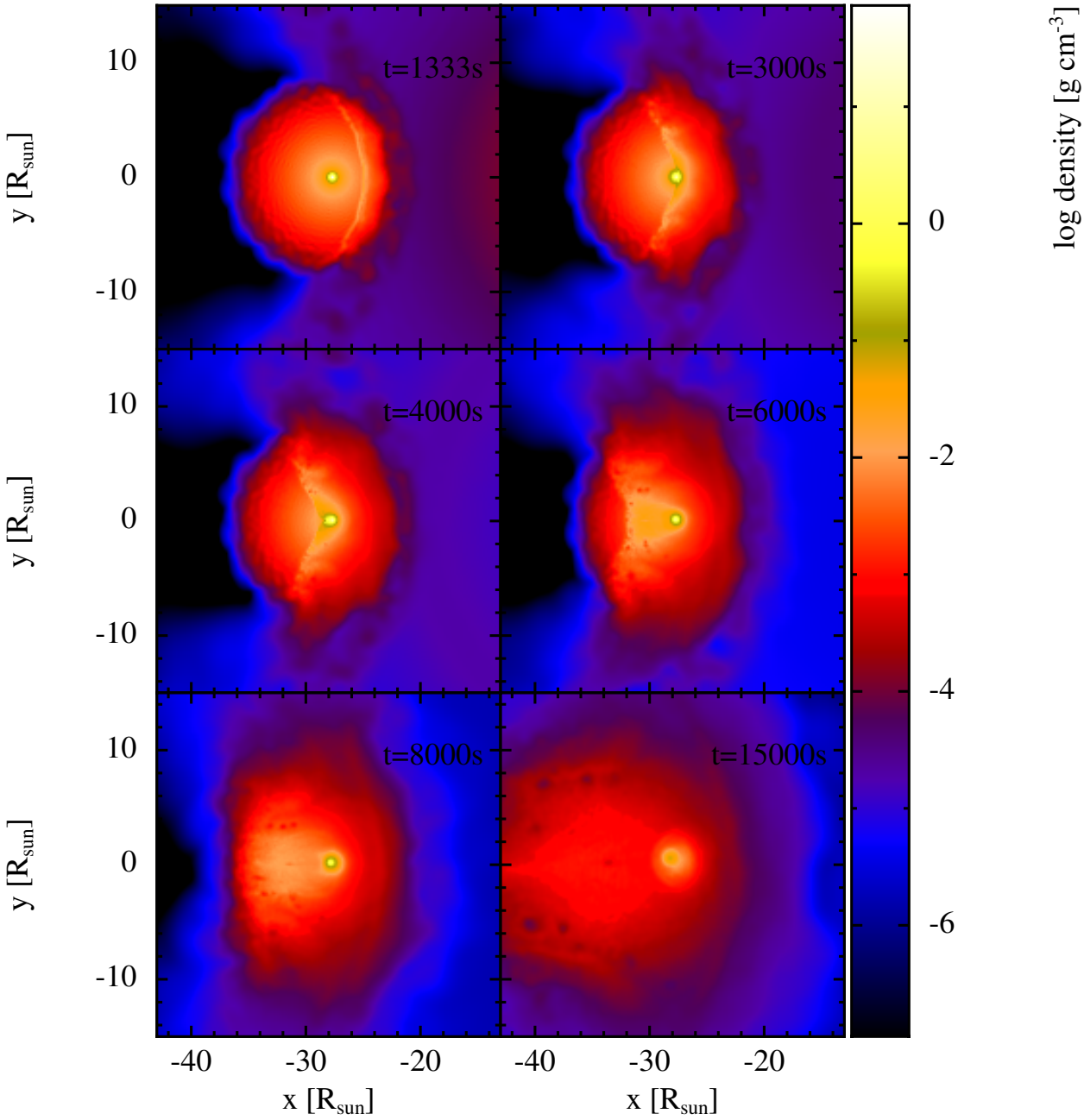

Figure 3.2: Passage of the shock wave through the sub-giant star (SG1), showing a density cross section through the core of the companion. As the shock passes through the star it wraps around the core and strips most of the stellar envelope. The evolution is very similar for the red giant, but at times a factor of ten later due to the larger separation.

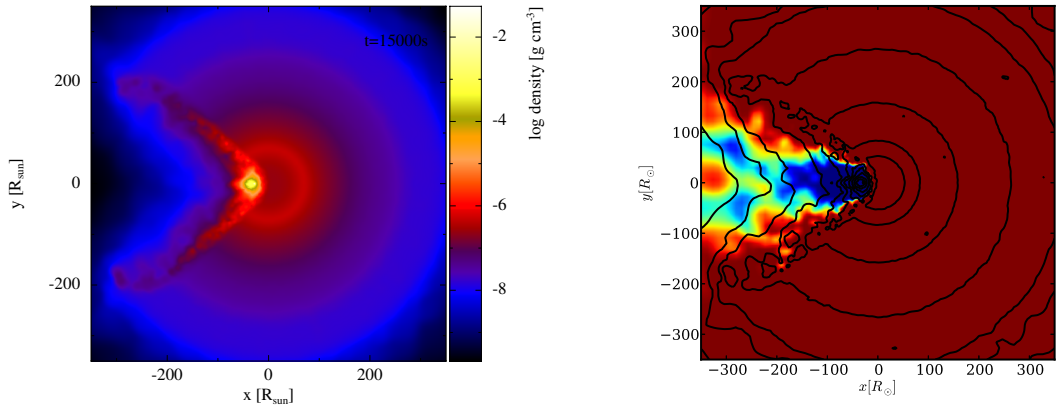

Figure 3.3: Cross-sections through the SG1 model once it has reached free expansion ($t = 15000\,\mathrm{s}$). *Left*: Density. There is a hole in the ejecta in the region that was shadowed by the companion star. *Right*: Composition of the SG1 model. Red is pure supernova ejecta, blue is pure stripped companion material. The contours show lines of constant density.

Tests conducted including artificial conduction during the supernova-companion interaction phase produce broadly similar results. The main difference are a slightly narrower bow shock, and smoother flow in the stripped companion material. The velocity distribution and mass stripped show good agreement, with the stripped mass differing by 2 per cent. The origin of this difference is due to both a modification to the temperature structure of the star and the improved treatment of instabilities.

Even with artificial conduction the SPH simulations poorly resolve instabilities, as they are prevalent in the low density regions behind the companion (see Marietta et al., 2000). However, while instabilities introduce turbulence into the flow, they are not important for capturing the general features, since they arise after the gas has been stripped from the companion. This is further confirmed by the concordance of the stripped mass and velocity distributions in SPH and grid methods found by Pakmor et al. (2008), who did not make any attempt to capture the instabilities in their SPH methods.

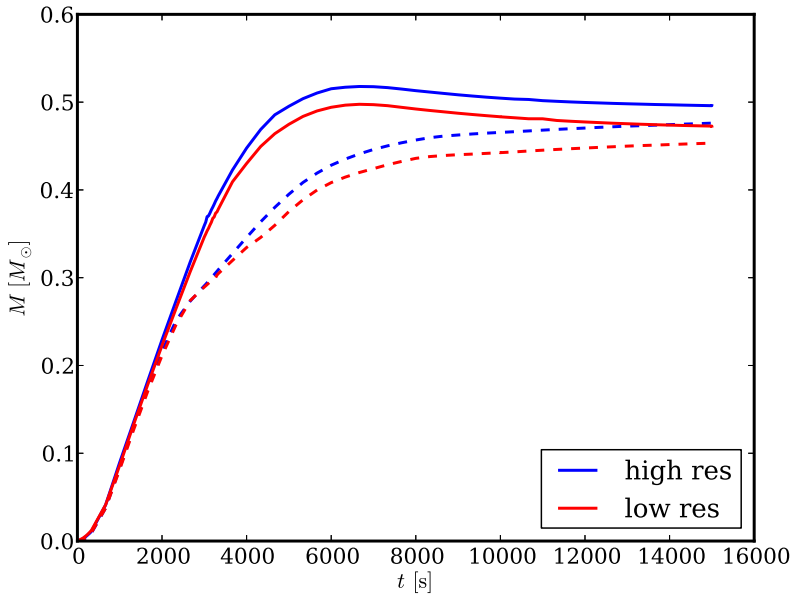

Figure 3.4: Evolution of the mass stripped from the sub-giant star. The mass stripped is defined as gas that was originally part of the companion which has a total energy greater than zero. The solid lines include the contribution from internal energy, whereas the dashed lines include only the kinetic and potential energy. The two methods give the same result until the shock reaches the companion's core ($t = 2000\,\mathrm{s}$), at which point it heats up the core. The increased pressure then drives further mass stripping, until at late times the two methods converge towards each other. The blue lines refer to the SG2 model ($M_{\mathrm{part}} = 10^{-6} M_\odot$) and the red lines refer to the SG1 model ($M_{\mathrm{part}} = 2 \times 10^{-6} M_\odot$), which give a four per cent difference in mass stripped.

3.3 Stripped Companion Material

The companion material is stripped by a combination of ram pressure stripping and ablation, which form the basis for the analytic model of Wheeler et al. (1975). The unbound mass as a function of time is shown in Fig. 3.4. Particles are flagged as unbound if their total energy is greater than zero. When the internal energy is included in the total energy the stripped mass peaks at 6000 s and then decreases, whereas the unbound mass continually increases until the asymptotic value is reached when thermal energy is neglected. Once the shock reaches the core it begins to stall and the momentum transferred to gas is no longer enough to strip it immediately. At this point the two criteria begin to diverge. The additional pressure in the post-shock gas then drives the expansion of gas away from the core. Some of this gas eventually reaches a velocity sufficient to escape the

companion. By the end of the simulation the unbound masses calculated by the two methods are converging, however they differ by $0.02 M_\odot$. The final unbound mass must be between these two values, and is taken to be the average.

The SG1 and SG2 models for the sub-giant give good agreement until 4000 s, after which the unbound mass starts to differ by $0.02 M_\odot$. As this represents only a small fraction of the unbound mass and the morphologies are very similar, a resolution of $M_{\rm part} = 2 \times 10^{-6}$ is sufficient.

For the red-giant model, the evolution of the unbound mass is similar, however the time-scale is a factor of ten longer due to the larger radius and separation. In this case the peak in the unbound mass including the thermal energy occurs at around 6.5×10^4 s, and the two measures converge to $M_{\rm strip} = 0.35 M_\odot$ within $0.01 M_\odot$ by 3×10^5 s.

The velocity distribution of the stripped companion material at the end of the simulation is shown in Fig. 3.5. The distribution of velocities is similar for both the sub-giant and red-giant models. The majority of the stripped gas is considerably denser than the surrounding ejecta and remains at $v < 500\,{\rm km\,s^{-1}}$, however there is a tail beyond $v \approx 2000\,{\rm km\,s^{-1}}$ in the negative x-direction, i.e. behind the companion. The asymmetry can be seen by in the final panel of Fig. 3.3. The stripped companion material remains close to the centre of the supernova.

The stripped companion material dominates the ejecta at velocities below $1950\,{\rm km\,s^{-1}}$, somewhat higher than the approximately $1600\,{\rm km\,s^{-1}}$ at which Marietta et al. (2000) find that the supernova becomes ejecta dominated. This can be partly reconciled by the fact that we use higher energy for the supernova model, 1.37×10^{53} erg, instead of the 1.2×10^{51} erg used by Marietta et al. (2000). The remaining difference is likely to be due to the differing evolution of our stars. Additionally, we find that the stripped companion material accounts for 0.2 to 0.3 per cent of the mass at $10^4\,{\rm km\,s^{-1}}$, within the range found by Marietta et al. (2000). Most of this high velocity material is found within the region behind the companion star, where the fraction of hydrogen rich material is near unity. Very little mass mixed into the ejecta (less than 100 particles), even in the simulations with artificial conduction.

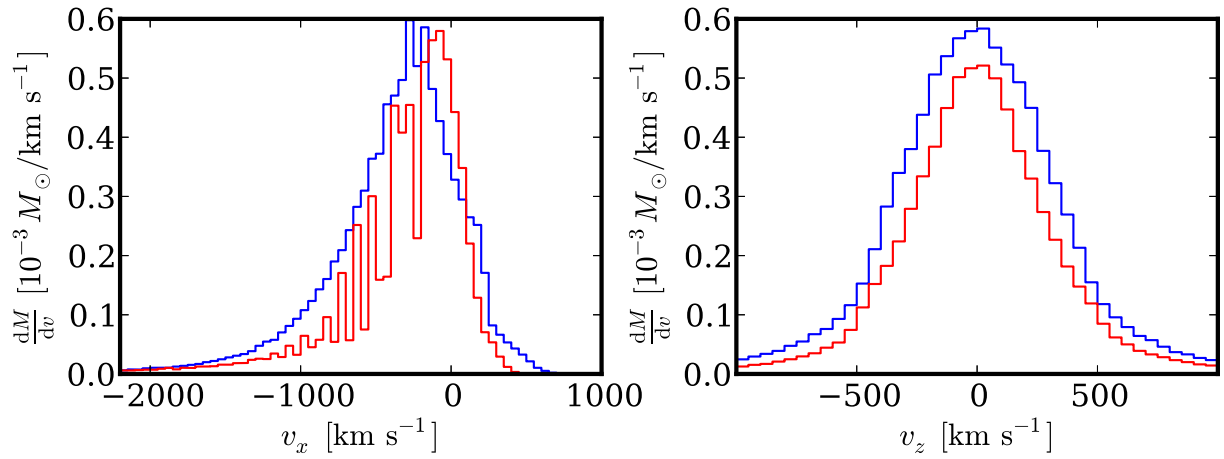

Figure 3.5: Velocity distribution of stripped companion material for the SG1 (blue) and RG1 (red). The high velocity tail in the x-direction arises from the material stripped, with the lower velocity material being made up of ablated material.

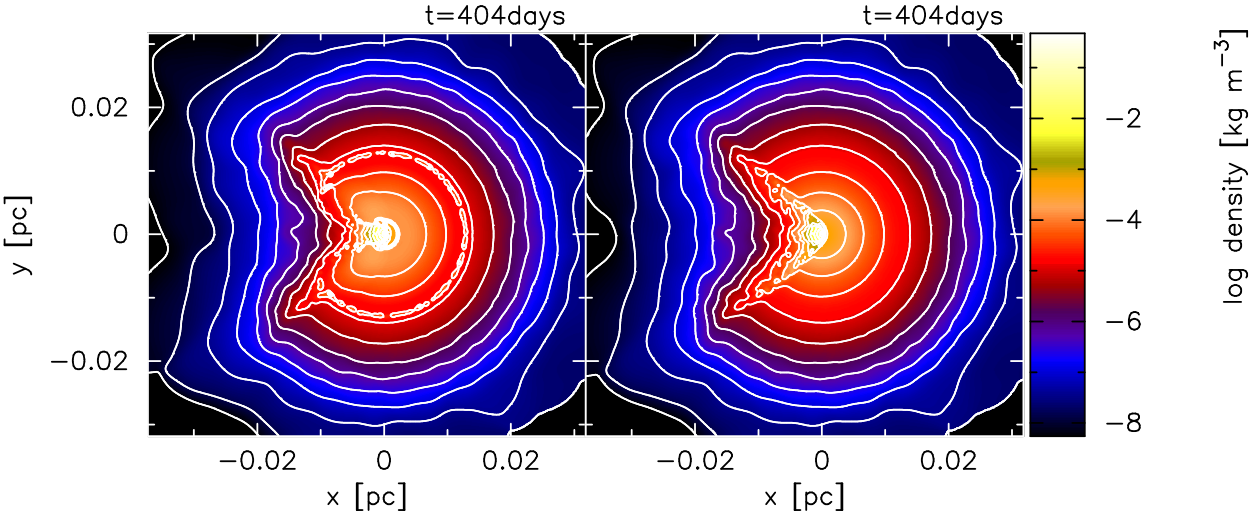

Figure 3.6: Comparison of density cross-sections in simulations with (left) and without (right) ^{56}Ni heating, for the sub-giant companion. For details see section 3.4. Cross sections are taken perpendicular to the binary axis at 404 days. Both the contours and colour indicate log density. There are minor differences. In the simulation with heating, the base of the high density paraboloid is broadened. Ring shaped artefacts can be seen in the density at the edge of the heated regions.

3.4 Impact of Radioactive Heating

For both sub-giant and red-giant models the supernova-companion interaction is complete within a few days of the explosion, and the ejecta evolve more or less independently of the companion star. Once this has occurred the material that remains bound to the companion star can be removed from the simulation. This greatly reduces the computational time, as the time-steps required to compute the hydrostatic equilibrium of the remaining star are much shorter than those needed for the evolution of the supernova. The surrounding medium can be neglected until the supernova sweeps up a significant fraction of its mass, and the ejecta and stripped companion material can be considered to evolve independently of it.

During this time, the supernova's light curve is powered by the radioactive decay of ^{56}Ni produced in the explosion. The decay processes is $^{56}\mathrm{Ni} \rightarrow {}^{56}\mathrm{Co} \rightarrow {}^{56}\mathrm{Fe}$ (electron-capture, β^+-decay). The two steps have e-folding times of 8.80 and 111.4 days, releasing 1.7 and 3.6 MeV energy each, mainly as γ-rays. The ^{56}Co decay also releases a positron 19 per cent of the time (Milne et al., 2004), which can be assumed to absorbed locally (e.g. Ambwani & Sutherland, 1988; Mazzali & Lucy, 1993; Lucy, 2005). Initially the supernova is opaque to the γ-rays, but by about 40 days after the supernova the optical depth through the ^{56}Ni layers has dropped to $\tau_\gamma \approx 1$. Therefore, a proper treatment of the energy deposition requires full radiative transfer.

A simple model is sufficient for verifying that the effects on the structure of the supernova are small, as long as the deposited energy is reproduced reasonably well. Half of the decay energy is released within $t_f = 40 - 50\,\mathrm{day}$, after which an increasing fraction of the γ-rays escape (Lucy, 2005). As the optical depth, $\tau_\gamma \propto t^{-2}$, the fraction of γ-rays absorbed drops quickly once the ejecta start to become optically thin. Therefore, we assume all the decay energy is captured locally before 40 days and completely escapes after then. The ^{56}Ni distribution is chosen to approximate the actual distribution in the W7 model (Nomoto et al., 1984), with $0.6\,\mathrm{M}_\odot$ of ^{56}Ni distributed in the low velocity ejecta in the mass range $0.1 - 0.9\ \mathrm{M}_\odot$, assuming a constant ^{56}Ni fraction. Cooling and radiative diffusion are neglected, which accentuate the effects at the edge of ^{56}Ni region by over-estimating pressure gradients. By varying t_f, it has been verified that the results are not sensitive to this value. As the effect is similar for the both the sub-giant and red-giant models only the

sub-giant is presented here.

Fig. 3.6 shows a snapshot of the density in simulations with and without the heating at 404 days after the explosion. The arc formed by the bow shock has become broadened in the heated region, causing the hole to partially close at low velocity. Density jumps occur at the edges of the heated region, which appear as two rings of blobs in the contours. The density jumps are an artefact of neglecting radiative diffusion, which would smooth out the strong temperature gradients that arise.

The changes occur gradually throughout the duration of the heating, which means that the partial closing of the hole is most relevant after maximum light. While the different structures are likely to lead to a slight difference in spectra, the difference is likely to be small as the difference in structure appears on the time-scale over which the ejecta become optically thin. Furthermore, as radiation can escape most easily through the hole the pressure gradient should be less than the one that arises in the simulations. This further supports the idea that the effects can be viewed as an upper limit.

These effects will be neglected in further calculation as the artefacts introduced by the heating outweigh the benefit of including the small effects.

3.5 Observational Prospects: Nebular Phase Emission

As noted by Marietta et al. (2000), a significant proportion of hydrogen rich material in the ejecta of SN Ia is an interesting prospect for observations. Since the stripped material remains deep inside the ejecta recent searches for hydrogen have been conducted during the nebular phase, once the supernova ejecta have become optically thin. One of the most stringent limits on hydrogen rich material comes from the nearby SN 2011fe, which limits the total Hα flux to $10^{35}\,\mathrm{erg\,s^{-1}}$ at roughly 300 days after the explosion (Shappee et al., 2013). By scaling models that replace the core of the supernova in spherical models with uniform hydrogen material (Mattila et al., 2005; Lundqvist et al., 2013), Shappee et al. (2013) suggest this limits the total mass stripped as $10^{-3}M_{\odot}$.

The nebular phase emission of Type Ia supernovae depends on the interplay of γ-ray deposition and ionization by the UV continuum with line emission (Mazzali et al., 2001). Due to the high UV opacity due the Fe-group elements in the ejecta, the UV contribution to the ionization can

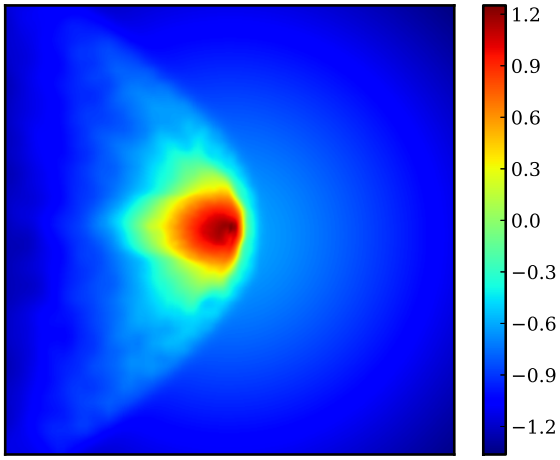

Figure 3.7: Optical Depth to γ-rays for ^{56}Ni decay 300 days after the explosion. The colour scale shows $\log_{10}(\tau_\gamma)$.

usually be neglected. In this section a simple model for the Hα emission is constructed, in which the ionization dominated by the local γ-ray deposition.

3.5.1 γ-ray Deposition

The conditions within the stripped companion material are expected to be very different to the surrounding ejecta due to the different composition, higher density and higher optical depth to γ-rays. The γ-ray optical depth to the centre of the stripped companion material $\tau_\gamma \approx 5$ at $t = 300\,\mathrm{day}$ (Fig. 3.7). For non-negligible optical depths, accurately calculating the γ-ray deposition normally requires Monte-Carlo radiation transfer techniques, as photons are predominantly scattered rather than absorbed.

For simplicity, we develop an approximation for the γ-ray deposition, which is motivated by the fact that the optically thick part of the core only occupies a small fraction of the volume in the supernova. If the ejecta were completely transparent to γ-rays, the Green function, $G(\mathbf{r}, \mathbf{r}')$, for the flux would be the same as that for Poisson's equation

$$G(\mathbf{r}, \mathbf{r}') = \frac{1}{4\pi|\mathbf{r} - \mathbf{r}'|^2} = \frac{1}{4\pi} \cdot \frac{1}{r^2 + r'^2 - 2rr'\cos(\theta)}, \tag{3.1}$$

where θ is the angle between the vectors. In the optically thick case, the Green's function is multiplied by $\exp(-\tau_\gamma(\mathbf{r},\mathbf{r}'))$, where τ_γ is the optical depth to γ-rays. Approximating the distribution of ^{56}Ni as spherical we find

$$F_\gamma(\mathbf{r},t) = \frac{1}{2}\int \frac{n_{\rm Co}(r',t)}{t_{\rm Co}} \exp(-\tau_\gamma(\mathbf{r},\mathbf{r}')) \frac{r'^2}{r^2+r'^2-2rr'\cos(\theta)}\,{\rm d}r\,{\rm d}(\cos(\theta)), \tag{3.2}$$

where $n_{\rm Co}(t)$ and $t_{\rm Co}$ are the number density of ^{56}Co atoms and the timescale for radioactive decay. In practice the contribution from ^{56}Ni is also included, but it is small during the nebular phase. Motivated by the fact that most of the volume is optically thin, we look for an expression based upon the solution for $\tau_\gamma = 0$,

$$F_\gamma(r,t) \approx \frac{1}{2}\int \frac{n_{\rm Co}(r',t)}{t_{\rm Co}} \frac{r'}{r} \log\left|\frac{r+r'}{r-r'}\right| {\rm d}r. \tag{3.3}$$

This expression can be easily evaluated for any $n_{\rm Co}(r)$, and forms the basis of the γ-ray deposition. Neglecting any dependence of θ on τ_γ, we find

$$F_\gamma(r,t) \approx \frac{1}{2}\int \frac{n_{\rm Co}(r',t)}{t_{\rm Co}} \frac{r'}{r} \log\left|\frac{r+r'}{r-r'}\right| \exp(-\tau_\gamma(r,r'))\,{\rm d}r. \tag{3.4}$$

The accuracy of this approximation depends on how well τ_γ can be chosen to match the angle-averaged value. For the majority of the volume, $\tau_\gamma \ll 1$, and therefore is not sensitive to choice. In the centre, where $\tau_\gamma > 1$, the choice has a greater effect on the flux. We choose the minimum value for $\tau_\gamma = \int_{r'}^{r} n_e(r)\sigma_\gamma\,{\rm d}r$, resulting in an upper limit for the γ-ray flux in the core. We note that this gives the correct limit for $r \to 0$, as well as at the edge of the optically thick region, where $\tau_\gamma \to 0$. As discussed in the later, the consequences of such a choice are minor.

The distribution of ^{56}Ni and ^{56}Co used is the same as in Section 3.4, $M(^{56}{\rm Ni}) = 0.6M_\odot$, which is spread over particles that were initially the mass range $0.1 < M/M_\odot < 0.9$. The ^{56}Ni density, $n_{\rm Co}(r)$, is then estimated by averaging the ^{56}Ni distribution over angle and solving the decay chain $^{56}{\rm Ni} \to^{56}{\rm Co} \to^{56}{\rm Fe}$ for the number of Co atoms.

The ionization rate from γ-rays is then calculated from the number of scatterings. Each scattering ejects a high-energy electron, which typically causes 10^4 secondary ionizations. Kozma &

Fransson (1992) provide convenient fitting formulae for the effective ionization, excitation and heating rate by γ-rays, which we make use of. Following Xu et al. (1992) we write

$$\Gamma_\gamma = F_\gamma \sigma_\gamma \eta_I(x_e), \tag{3.5}$$

where the factor $\eta_I(x_e)$, takes into account the ionizations *and* excitations from secondary electrons. The γ-ray scattering cross-section, σ_γ, used is the electron scattering cross-section averaged over the distribution of photon energies released in the radioactive decay (Milne et al., 2004). The efficiency of ionization and excitation depends on the electron fraction x_e. For $x_e = n_e/n_\mathrm{H} = 10^{-4}$, 90 per cent of the energy is available, at $x_e = 0.1$ this reduces to 40 per cent. The remaining fraction of energy goes into heating the electrons.

3.5.2 Model Atom

In order to calculate the emissivity and opacity of Hα we follow the models for the emission from hydrogen excited by non-thermal deposition by Xu et al. (1992) and Kozma & Fransson (1992). Although these models were constructed for the Type II supernova SN 1987A, the physics involved is sufficiently similar, in particular that the gas is hydrogen rich. Similarly, the spherical models presented by Mattila et al. (2005) and Lundqvist et al. (2013) that have been used to constrain the stripped mass from the companions of Type Ia supernovae were based on Kozma & Fransson (1992).

As the typical velocities ($v \sim 10^3\,\mathrm{km\,s^{-1}}$) are much larger than the random motions ($\Delta v_\mathrm{D} \sim 3\,\mathrm{km\,s^{-1}}$) the Sobolev approximation can be used to solve the radiative transfer (Sobolev, 1947; Castor, 1970). In this approximation, the optical depth in a line can be calculated purely locally. The Sobolev optical depth for $v \propto r$ is given by

$$\tau_S = \frac{\pi e^2}{m_e c} f_{lu} \lambda_0 t \left(1 - \frac{g_l n_u}{g_u n_l}\right), \tag{3.6}$$

where f_{lu} and λ_0 are the oscillator strength and rest frequency of the transition, e and m_e are the mass and charge on the electron and c is the speed of light. This can then be used to calculate the

probability that a photon escapes the region:

$$\beta_S = \frac{1 - e^{-\tau_S}}{\tau_S}. \tag{3.7}$$

For resonance lines such as Lyman α, the optical depth can be very large, requiring many scatterings before the photon can escape. In this case, the photon may first escape through continuum absorption. Following (Hummer & Rybicki, 1985) the continuum destruction probability is

$$\beta_C = \frac{k_C}{k_L} F\left(\frac{1}{\tau_S}, \frac{k_C}{k_L}\right), \tag{3.8}$$

where k_C is the continuum opacity and k_L is the mean opacity of the line and

$$F\left(\frac{1}{\tau_s}, \frac{k_C}{k_L}\right) = 1.87\left(a\frac{k_L}{k_C}\right)^{1/4}, \tag{3.9}$$

for the case of partial redistribution (Chugai, 1987). The Voigt parameter, a, is the ratio of natural broadening, γ, to Doppler broadening, $a = \gamma/\Delta\nu_{\rm D}$. Including the continuum destruction probability $\beta_S \to (1 - \beta_C)\beta_S + \beta_C$.

The high densities mean that the ℓ-states are well mixed and the electrons are distributed within them according to statistical weight, therefore averaged transition probabilities can be used. The dominant mechanism for ionization and excitation is from the non-thermal electrons generated by γ-rays (Xu et al., 1992). In this case the population of the ground state can be calculated through

$$\Gamma_\gamma\, n_1 = n_2[A_{2\gamma} + A_{21}\beta_{21} + n_e C_{21}], \tag{3.10}$$

where $A_{2\gamma} = 4.69 \times 10^8\,\mathrm{s}^{-1}$ and $A_{21} = 2.05\,\mathrm{s}^{-1}$ are the ℓ-averaged Lyman α and two-photon decay rates. The electron density is given by n_e. At temperatures of a few $10^3\,\mathrm{K}$ collisional ionization and excitation can be neglected; however, the collision de-excitation rate $n_2 n_e C_{21}$ is included. At $1000\,\mathrm{K}$, $C_{21} = 1.6 \times 10^{-7}\,\mathrm{cm}^3\,\mathrm{s}^{-1}$ (Vriens & Smeets, 1980). Recombinations to the ground state result in the re-ionization of a H-atom as the stripped material is optically thick to the Lyman continuum and therefore are also neglected. Similarly, due to the high optical depth photons emitted in the

Lyman series will be reabsorbed and can be neglected. Thus the population of the $n = 1$ state arises through balance of both ionization and excitation (included in Γ_γ) with decays from the $n = 2$ state.

From Xu et al. (1992), the population of the $n = 2$ state is given by

$$n_2[A_{2\gamma} + A_{21}\beta_{21} + n_e C_{21} + \zeta_2] = n_e n_+ \alpha(T) + n_1 \Gamma_\gamma f_2(x_e), \tag{3.11}$$

where n_+ is the number of H^+ ions. The factor $n_1\Gamma_\gamma f_2(x_e)$ is the rate of excitation from the $n = 1$ to the $n = 2$ level, $f_2(x_e) \approx 0.37$ when the ionization fraction $x_e = 10^{-4}$ and $f_2(0.1) \approx 0.41$ (Kozma & Fransson, 1992). The parameter ζ_2 is included to take care of photoionization from the $n = 2$ state, and $\alpha(T)$ is the effective recombination coefficient, which ignores recombinations to the ground state. Equation (3.11) arises from assuming the gas is optically thick to the Lyman continuum, which results in all decays to the ground state going through the $n = 2$. In this case all excitations and ionizations populate the $n = 2$ state. Under this approximation, the rate of excitations from the $n = 2$ state is balanced by de-excitation to the $n = 2$ state, therefore doesn't appear in equation (3.11).

Assuming the population of states with $n > 2$ is negligible, then $n_1 + n_2 + n_+ = n_{\rm H}$ and $n_e = n_+$. The ionization fraction is then calculated by balancing the ionization rate from the $n = 1$ and $n = 2$ states with the recombination rate

$$n_1\Gamma_\gamma + n_2\zeta_2 = n_+ n_e \alpha(T). \tag{3.12}$$

For $n_1 \gg n_2$, $n_1 \approx n_H(1 - x_e)$, giving rise to a quadratic equation for x_e,

$$n_H(\Gamma_\gamma + \frac{n_2}{n_1}\zeta_2)(1 - x_e) = (n_H x_e)^2 \alpha(T), \tag{3.13}$$

which has the solution

$$x_e = 2\left[1 + \sqrt{1 + 4\frac{n_H\alpha}{\Gamma_\gamma(1 - f_2) + n_2\zeta_2/n_1}}\right]^{-1} \approx \sqrt{\frac{\Gamma_\gamma(1 - f_2) + n_2\zeta_2/n_1}{n_H\alpha}} \tag{3.14}$$

where $n_{\rm H} = n_1 + n_2 + n_+$ and the approximation holds for $x_e \ll 1$. As Γ_γ, f_2 and n_2 depend on

x_e, the solution must be iterated.

As shown by Xu et al. (1992) for a uniform density gas, once the optical depth to Hα, $\tau_{\mathrm{H}\alpha} > 300$ then a the gas becomes optically thick to the Balmer continuum. Once this happens the two-photon emission, can ionize hydrogen from the $n = 2$ and contribute significantly to the photo-ionization rate. Since 71 per cent of the two-photon emission lies in the Balmer continuum (Nussbaumer & Schmutz, 1984; Xu et al., 1992), the photo-ionization rate from the $n = 2$ level is

$$n_2\zeta_2 = n_2[0.71A_{2\gamma}(1 - P(\tau_{2\gamma})) + A_{21}\beta_C + \xi_2]. \tag{3.15}$$

The destruction of Lyα by photoionization of the $n = 2$ state has been included using the continuum destruction probability from equation (3.8), although this contributes less than the two-photon emission. Following Xu et al. (1992) an extra term (ξ_2) has been included to allow for photo-ionization from other sources. An accurate calculation of the two-photon escape probability for the full geometry requires full radiative transfer, so a simple estimate is used. Approximating the core as spherical, as in the γ-ray deposition, the optical depth can be estimated with $\tau_{2\gamma} = \int n_2(r)\sigma_B \, \mathrm{d}r$, where σ_B is the photoionization cross-section for the $n = 2$ state. The cross-section at the edge of the Balmer continuum is used and is calculated using the gaunt factors from Johnson (1972). The escape probability is estimated using the formula for a uniform spherical nebula (Osterbrock, 1989)

$$P(\tau) = \frac{3}{4\tau}\left(1 - \frac{1}{2\tau^2} + \left(\frac{1}{\tau} + \frac{1}{2\tau^2}\right)\exp(-2\tau)\right). \tag{3.16}$$

Since the stripped companion material is densest in the centre this must overestimate the escape probability in the centre and underestimate it at the edge. During the optically thick phase the two photon emission is insensitive value of the escape probability and once the optical depth becomes small the ionization from two-photon emission is small, which means the error in the population fractions should not be too large. Furthermore, the ionization by two-photon emission is always less than 20 per cent of the total non-thermal ionization rate.

While a proper calculation of the emissivity of Hα requires modelling several levels of the H atom; a reasonable estimate can be made by assuming each excitation to $n \geq 3$ and each recombination

releases a Hα photon. While the gas is optically thick to the Balmer continuum this is a reasonable approximation as photons emitted in higher Balmer series lines will be re-absorbed and branch to form a Paschen series line and Hα. Once the stripped material is optically thin to the Balmer continuum this overestimates the emissivity by a factor of two, as the line ratios tend to their case B values (Xu et al., 1992; Storey & Hummer, 1995). The transition occurs at roughly 350 days for models with $M = 0.5 M_{\odot}$.

The Hα volume emissivity is therefore

$$\epsilon_{\mathrm{H}\alpha} = [n_1 \Gamma_{\gamma}(1 - f_2) + n_2 \zeta_2] \beta_{\mathrm{H}\alpha}. \tag{3.17}$$

The luminosity can then be calculated by $L = \sum_i \frac{N_i}{n_{\mathrm{H},i}} \epsilon_i$, where N_i is the number of hydrogen atoms corresponding to particle i, and the sum is over all SPH particles that make up the stripped companion material. The ratio $N_i / n_{\mathrm{H},i}$ is independent of the mass of the stripped material and can be thought of as a volume element. While Hα is optically thick $\beta_{\mathrm{H}\alpha} \approx 1/\tau_{\mathrm{H}\alpha} \approx (n_2 a_0 f_{21} \lambda_{21} t)^{-1}$ and

$$\begin{aligned} \epsilon_{\mathrm{H}\alpha} &\approx \frac{n_1 \Gamma_{\gamma}(1 - f_2) + n_2 \zeta_2}{n_2 a_0 f_{21} \lambda_{21} t} \\ &\propto \frac{1}{t} \cdot \frac{(1 - f_2) + n_2 \zeta_2 / (\Gamma_{\gamma} n_1)}{A_{2\gamma} + A_{21} \beta_{21} + C_{21} n_e}, \end{aligned} \tag{3.18}$$

which is roughly independent of the rate of γ-ray deposition. The dependency on the γ-ray deposition is reduced to its effect on the electron fraction, which only effects emissivity when collisional de-excitation dominates the decay of atoms from $n = 2$ to $n = 1$.

3.5.3 Results

In order to compare this to previous work (Mattila et al., 2005), a simple model is constructed using $0.05 M_{\odot}$ of hydrogen distributed uniformly in the region $v < 1000\,\mathrm{km\,s^{-1}}$. The resulting H$\alpha$ luminosity is shown in Fig. 3.8 and $L \sim 3 \times 10^{34}\,\mathrm{erg\,s^{-1}}$ remains roughly constant until until Hα becomes optically thin, when it begins to decay exponentially.

The difference in emission at late times arises from the γ-ray optical depth, which is proportional

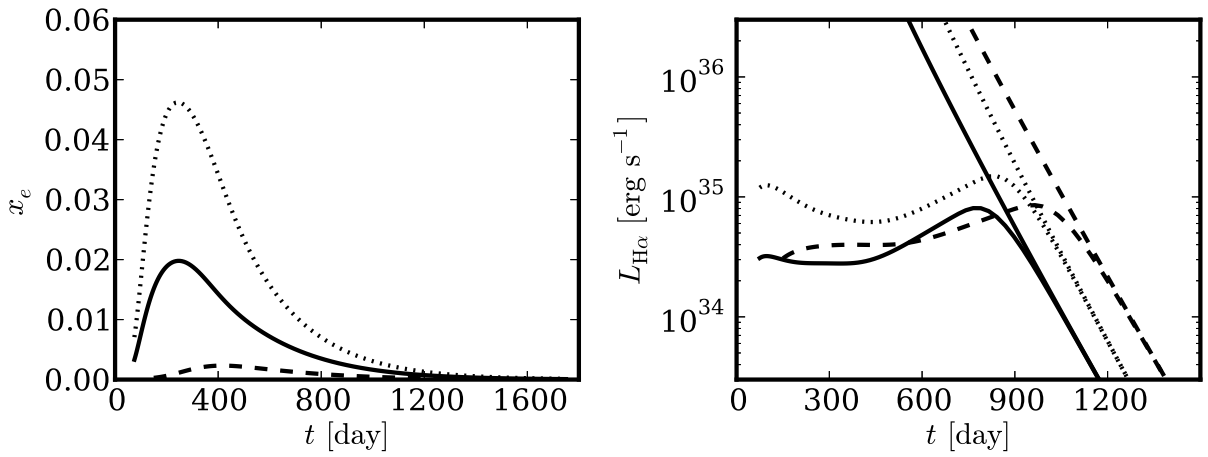

Figure 3.8: Ionization fraction (left) and Hα luminosity for uniform stripped hydrogen density. Two models have $0.05M_\odot$ (solid, dotted), and the other has $0.5M_\odot$ (dashed) of stripped companion material. While the mass affects the ionization fraction but has little effect on the luminosity. The most luminous model has a non-zero photo-ionization component, ξ_2, as described in the text. The bumps in the luminosity at around 450 days occur as the dominant depopulation mechanism for the $n = 2$ state changes from collisional de-excitation to 2-photon emission. The emission is more or less independent of mass; however, the more massive model transitions to optically thin emission later.

to mass once the ejecta become optically thin. Perhaps somewhat surprisingly, during the period while the gas is optically thick to Hα, the emission appears to be weakly dependent on the mass. This can be verified from equation (3.18). While the material is optically thick to γ-rays $\Gamma_\gamma \propto N_{\mathrm{H}}^{-1}$, which means even the electron density is independent of mass. Therefore even though the depopulation of the $n = 2$ is dominated by collisions the emissivity is roughly constant. The transition to depopulation by two-photon emission occurs at roughly 400 days in the $0.05M_\odot$ model, causing the dip in the luminosity. This transition does not occur in the $0.5M_\odot$ models until later as by this time the gas is becoming optically thin to γ-rays.

The emission using the density distribution from the sub-giant simulation is shown in Fig. 3.9,.for models with $\xi_2 = 0$, and ξ_2 is set such that the γ-ray deposition is maximally efficient. The γ-ray deposition and $\tau_{2\gamma}$ have not been modified. As the stripped mass is $0.42M_\odot$, these should be compared to the $0.5M_\odot$ uniform model.

The model based on the structure from the sub-giant simulations predicts a much higher luminosity than the uniform models, with $L \sim 10^{36}$ for $\xi_2 = 0$. The origin for the difference can

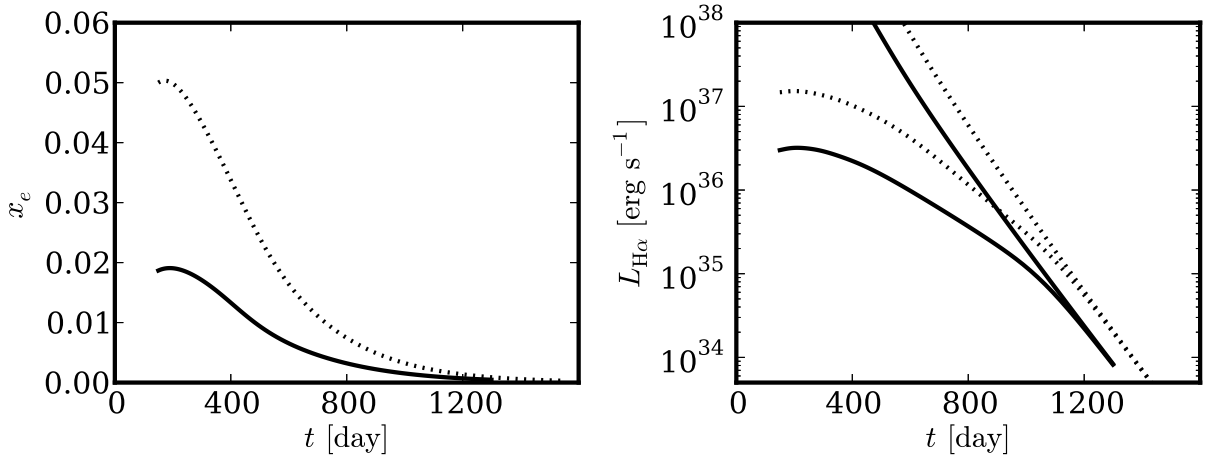

Figure 3.9: Same as Fig. 3.8, but using the density distribution from the sub-giant simulations., For $\xi_2 = 0$ (solid), and $\xi_2 \neq 0$ (dotted, see text). In both cases, the peak luminosity is above the threshold for detection in SN 2011fe.

be seen by comparing the escape probability of Hα between the models. For the uniform model $\beta \approx 10^{-4}$. However, for the sub-giant models it is only this small near the centre of the ejecta, where the density is highest. The escape probability reaches unity for the gas at $v \sim 5 \times 10^4\,\mathrm{km\,s^{-1}}$, which corresponds to the peak in the flux. The line profile is much broader than the models of Mattila et al. (2005). For observers viewing parallel to the hole, the line has a width of $10^4\,\mathrm{km\,s^{-1}}$, which roughly corresponds to 100Å. For observers viewing perpendicular to the hole, the line profile is flat-topped out to $2000\,\mathrm{km\,s^{-1}}$, with the flux dropping to half its peak value by approximately $2700\,\mathrm{km\,s^{-1}}$. The broader lines mean that the flux relative to the continuum is lower for a given luminosity and is also wider than the width of the Hα lines that previous searches have considered (Leonard, 2007; Shappee et al., 2013). As there are features on the scale of 100Å in SN 2011fe the limits on stripped hydrogen may not be as strong as suggested.

We note that the the luminosity of the uniform model produced by these calculations is considerably less than the luminosity that was found by Mattila et al. (2005) and Lundqvist et al. (2013), for similar models. Mattila et al. (2005) which for $M = 0.05 M_\odot$ is $\sim 10^{36}\,\mathrm{erg\,s^{-1}}$ at 300 days after the explosion. One possible explanation for this is that the present calculations neglect photo-ionization. A rough limit for the additional photo-ionization rate can be found by adding the remaining fraction of γ-ray decay energy to the ionization rate from $n = 2$. For $x_e \sim 10^{-2}$, this

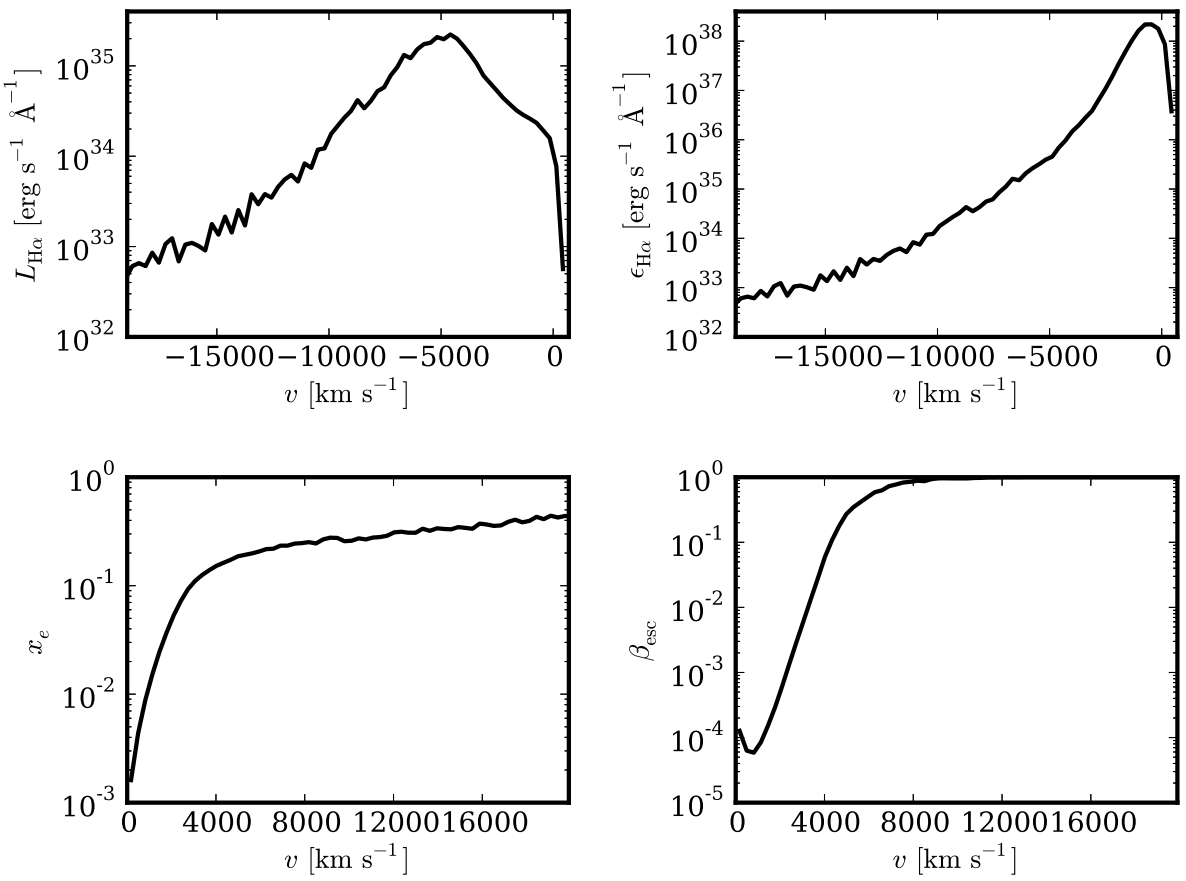

Figure 3.10: Variation of the emitting conditions as a function of velocity 300 days after the explosion for the inhomogeneous model with $\xi_2 = 0$. In the top panels the velocity is for an observer viewing the system down the hole in the ejecta, while the radial velocity is used in the bottom panels. *Top Left*: Emergent luminosity. *Top Right*: Emitted luminosity, neglecting the optical depth in Hα. *Lower Left*: Ionization Fraction. *Lower Right*: Hα escape probability. The peak in the luminosity arises at the velocity where the ejecta become optically thin, even though the majority of the mass is at much lower velocity.

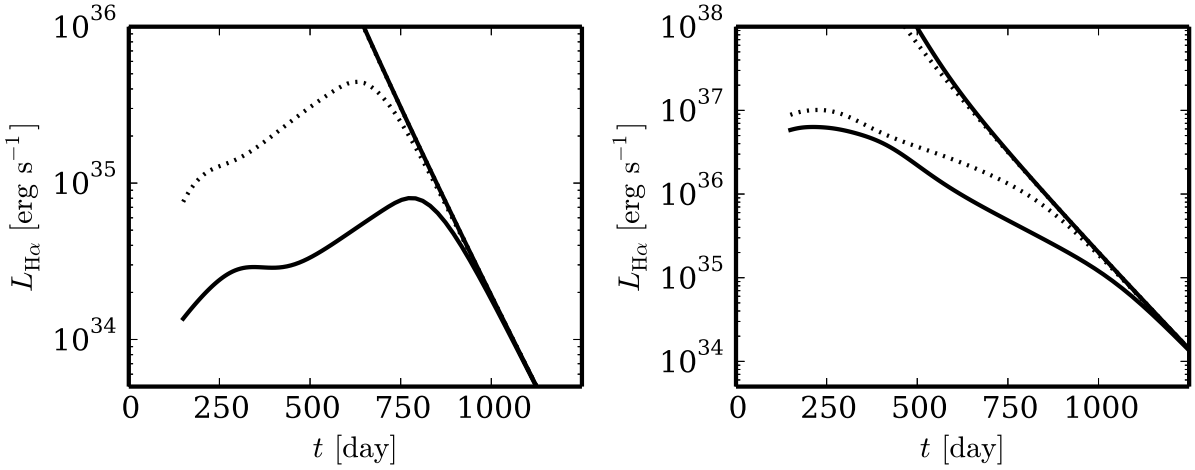

Figure 3.11: Like Figure 3.8, except for models for a $0.5M_{\odot}$ uniform core (left) and the sub-giant star (right). Shown are the canonical model (solid lines) and a model where the absorption of Lyα by Fe II lines has been included. The increased Lyα escape translates into an increased Hα escape probability, resulting in more luminous lines. The lower unabsorbed flux in the sub-giant model arises as the absorption of the Balmer continuum is less effective, resulting in a slightly lower ionization rate.

represents 30 per cent of the energy deposited. As the ionization potential from $n = 2$ is one quarter of the ionization potential from the ground state, this represents the most efficient deposition of energy as for ionizing hydrogen, and roughly corresponds to $\xi_2 \approx 1.5\Gamma_{\gamma}$, roughly doubling the ionization rate. This results in a $L \sim 10^{35}\,\mathrm{erg\,s^{-1}}$, which is still considerably smaller than the that of Mattila et al. (2005).

The most likely source for the discrepancy is the escape probability for Lyman α. If our models under predict the escape probability for Lyman α, then the overpopulation of the $n = 2$ level resulting in a greater optical depth and weaker lines. A possible origin effect is the overlap of the Lyman α with nearby lines. As Lyman α photons scatter and diffuse in frequency they can be absorbed in nearby lines. Jerkstrand et al. (2012) estimate that nearby Fe II and Cr II lines may result in an escape probability for Lyman α of $\beta = 10^{-8}$, which can dominate the Sobolev or continuum destruction escape probability.

Fig. 3.11 compares models with and without the line overlap term. While line overlap makes a significant difference in uniform models, bringing them closer in luminosity the models reported by Mattila et al. (2005), the effects are less prevalent for the sub-giant models. This can be explained

because a large fraction of the luminosity comes from higher velocities, where the optical depth to Lyman α is lower.

Even with this term included the luminosity of the uniform model remains an order of magnitude lower than the Mattila et al. (2005) results. As the luminosity is only weakly dependent on the mass or γ-ray luminosity, the remaining discrepancy may still be due to Lyman α escape probability. We therefore note that an accurate treatment of Lyman α is important for producing robust results about the emission from stripped hydrogen in the centre of Type Ia supernovae.

However, the relatively small effect that the different models have on the realistic density distribution means that the results for such a model may be more robust. Furthermore, we find that these models are insensitive to a moderate increase increase in γ-ray deposition, supporting the conclusion. The models therefore suggest that the luminosity of hydrogen rich material stripped from relatively giant stars is likely to be detectable. However, current observational limits may be weakened if the line profiles are wider than previously thought, suggesting that robust multi-dimensional models and thorough cross-checking of observations are needed to fully resolve the issue.

3.6 Summary

The interaction of a Type Ia supernova with its companion star has been modelled using SPH with companions chosen to represent the possible progenitors for specific systems. An evolved sub-giant star, which is chosen to be the possible progenitor of Tycho-G and a red giant star is also chosen, which corresponds to the best known parameters for RS Ophiuchi.

The supernova-companion interaction models are consistent with the recent simulations that use suitably evolved companion stars (Liu et al., 2012; Pan et al., 2012), and agree with analytical estimates (Wheeler et al., 1975). The results show that most of the envelopes should be stripped by the supernova. The majority of the mass stripped remains at low velocities relative the supernova ejecta ($v \lesssim 1000\,\mathrm{km\,s^{-1}}$).

Despite the large amount of mass stripped, it is unlikely that the presence of solar material can be detected until the nebular phase as electron scattering will spread out the emission lines. Simple models seem to produce lower luminosities than those of Mattila et al. (2005); however, the calcu-

lations predict higher luminosities for more realistic distributions of material from the simulations. However, it is possible that the line profiles are significantly broader than those previously expected, which may significantly weaken previous constraints. These calculations highlight the need for realistic multi-dimensional simulations of nebular spectra for constraining the mass stripped from the progenitor.

Chapter 4

The Circumstellar Medium and Tycho's Supernova Remnant

Supernova remnants (SNR) provide unique possibilities for studying supernovae. Due to their long life-times many are known in the Galaxy. They provide a unique opportunity to see the resolved structure of the supernovae, which allow us to probe different aspects of the supernovae to those that can be probed using spectra and light curves of distant supernovae.

One of the youngest known Galactic SNRs thought to host a Type Ia supernova is Tycho's Supernova Remnant, thought to be the remnant of a supernova observed by Tycho Brahe in 1572. Young supernova remnants are good probes for supernovae, as during the first few hundred years of their evolution the dynamics is dominated by the ejecta density and velocity. As they age and cool, they go from being ejecta dominated to interstellar medium dominated, which makes extracting information about the host supernova more difficult (Woltjer, 1972).

The dynamics of a SNR can be characterised in one dimension and has a distinctive two-shock structure. The supernova drives a shock through the interstellar medium, known as the forward shock (FS), and at the same time a second shock is driven into the ejecta, the reverse shock (RS). Separating the shocked supernova and the shocked interstellar medium is the contact discontinuity (CD). In one dimension, the contact discontinuity appears as discontinuity in the density and internal energy but the pressure and velocity are continuous, as in the contact discontinuity in the

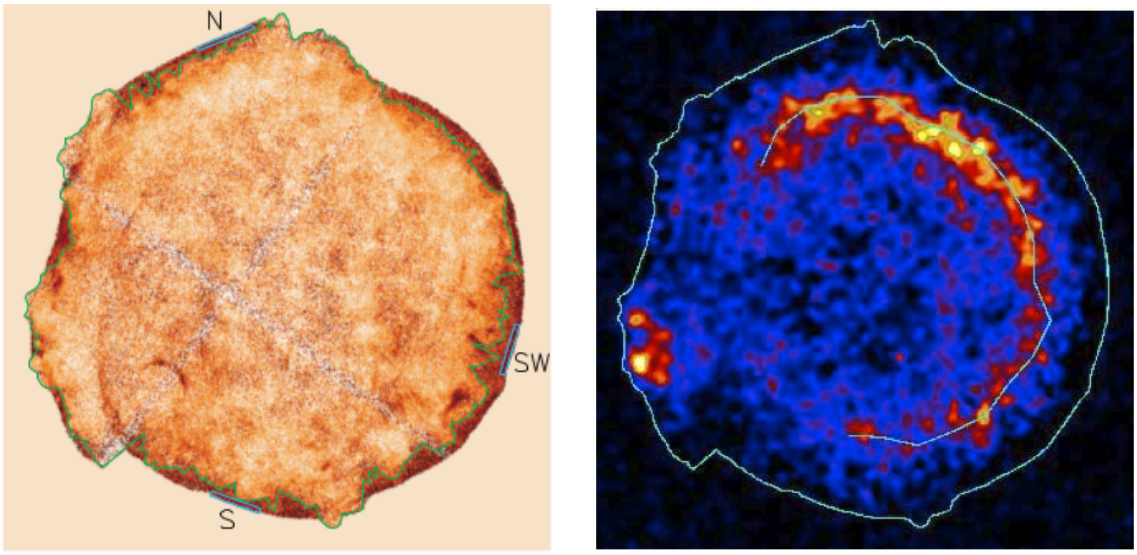

Figure 4.1: *Left*: X-ray image of Tycho's supernova remnant, showing the continuum dominated shocked ISM (dark) and line dominated ejecta (light). The contact-discontinuity is traced by a green line. A number of narrow features can be seen tracing internal shocks. *Right*: Continuum subtracted Fe Kα emission from Tycho's SNR. The Fe Kα line traces the shocked iron-rich ejecta, which shows a curious structure consisting of a broken ring and a high velocity knot. The white lines show the location of the forward and reverse shocks, as traced by non-thermal X-ray emission and the Fe Kα line respectively. [Reproduced from Warren et al. (2005)]

shock tube problem presented in Section 2.2.8.

However, the contact discontinuity is subject to the Rayleigh-Taylor instability. The growth of the instabilities at the contact discontinuity has been studied using two- and three-dimensional simulations in some detail, but using spherical models of the ejecta and interstellar medium. Wang & Chevalier (2001) use pure hydrodynamic simulations to show that Rayleigh-Taylor instabilities have little effect on the passage of the forward shock. This is discrepant with X-ray observations of Tycho's SNR, which suggest that fingers of ejecta extend beyond the forward shock (Warren et al., 2005). If the ejecta contains clumps with a density ratio of approximately 100, then these could survive the passage of the reverse shock and could protrude the forward shock (Wang & Chevalier, 2001), thus explaining the ejecta fingers.

The forward shock in Tycho's SNR also appears to be closer to the contact discontinuity than expected from hydrodynamic models. Warren et al. (2005) find $r_{\rm FS}/r_{\rm CD} \approx 0.93$ and suggest that this could be explained by cosmic-ray acceleration at the shock front. This would reduce the post-

shock temperature and allow the shocked interstellar medium to reach higher densities than are possible for an adiabatic should. Since the contact discontinuity is closer to the forward shock, this may also help the ejecta fingers protrude the forward shock. However, so far no consistent model of the SNR structure and X-ray emission has been devised.

As well as the narrow band of shocked interstellar medium, Warren et al. (2005) also found a narrow band of Fe Kα emission that can be used to trace the reverse shock (their Fig. 1, reproduced as Fig. 4.1). The Fe emission makes an incomplete ring in the region of the remnant that has the most uniform X-ray properties, as well as a fast moving knot. The origin of this structure is currently unexplained. In this chapter we consider the prospects for forming this via the supernova-companion interaction.

The high $r_{\rm FS}/r_{\rm CD}$ ratio could also be explained if the forward shock is now entering a more dense region of the interstellar medium than before, which would be possible in a pre-supernova wind swept out a cavity in the interstellar medium. However, one-dimensional models for the X-ray emission suggest the opposite, that the forward shock has entered a low-density interstellar medium, having previously interacted with a dense wind from the companion star that was ejected in the 0.25 Myr prior to the explosion (Chiotellis et al., 2013).

Chiotellis et al. (2013) used one-dimensional models to determine the best fitting model for the environment, which may be appropriate for the region of the SNR that the X-ray spectra were taken from. If Chiotellis's hypothesis is correct, then this would be strong evidence that the progenitor of Tycho's Supernova was single degenerate. As we have already seen in Chapter 3, the resultant ejecta structure is not spherical. Furthermore, pre-supernova winds from these systems are not expected to be spherical (see Chapter 5). The morphology of supernova remnants produced by single-degenerate progenitor scenarios is the subject of this chapter.

4.1 Initial Models for the Supernova Remnant

The supernova remnant is modelled using three-dimensional Smoothed Particle Hydrodynamics. The initial supernova structure is taken from the final stages of the supernova-companion interaction results in Chapter 3. Calculations using both the sub-giant and red giant models have been

conducted, producing similar SNR structures. For brevity, only the models using the sub-giant are presented and discussed in this chapter, but the results should for other non-degenerate companions.

The material that remains bound to the companion star has been removed from the simulations to save the computational cost of maintaining hydrostatic equilibrium in the star. While this has no effect on the dynamics, the hole left at the location of the companion star can be seen in some of the figures.

Three models for the environment around the supernova are constructed. A constant density medium representing an unperturbed interstellar medium, with $n_{\rm H} = 1\,{\rm cm}^{-3}$, which can be compared to the two-dimensional calculations by García-Senz et al. (2012); a spherically symmetric wind with a mass-loss rate of $\dot{M} = 10^{-6} M_{\odot}$ and velocity $v_{\rm w} = 50\,{\rm km\,s}^{-1}$ and a non-spherical model for the circumstellar medium around a recurrent nova progenitor, which is based upon the models presented in Chapters 5 and 6.

The recurrent nova model is constructed using alternating periods of mass-loss via a wind from a red giant and novae. The wind has a mass-loss rate $\dot{M} = 10^{-7}\,M_{\odot}\,{\rm yr}^{-1}$, which is focussed into the binary plane via gravitational interaction with the binary and novae that are ejected every 18 yr and have a mass of $2 \times 10^{-7}\,M_{\odot}$. The novae sweep up the red giant wind, forming an elliptical structure (see Fig. 6.2).

The environment around the supernova is set up using glass-like initial conditions (Section 2.2.8). For a constant density interstellar medium the uniform glass is used directly. The spherical wind model is produced by warping the glass radially. The transformation $r' = Kr^3$, is used to convert the density from a uniform distribution to a $\rho = \frac{\dot{M}}{v}\frac{1}{4\pi r^2}$ wind, where r is the radius of a particle in the uniform density glass, r' is its radius in the wind and K is a constant.

Since the particle mass used in the recurrent nova calculations is $m \approx 10^{-12} M_{\odot}$, which is 6 orders of magnitude smaller than the particles used in the supernova calculation, the models cannot be used directly. Therefore, an approximate model for the large scale structure needs to be used. Since the novae eventually reach a constant velocity, the large scale structure can be approximated as a static wind, but with the mass-loss rate and velocity varying as a function of angle. The circumstellar medium formed by the recurrent nova is bipolar but approximately axial-symmetric,

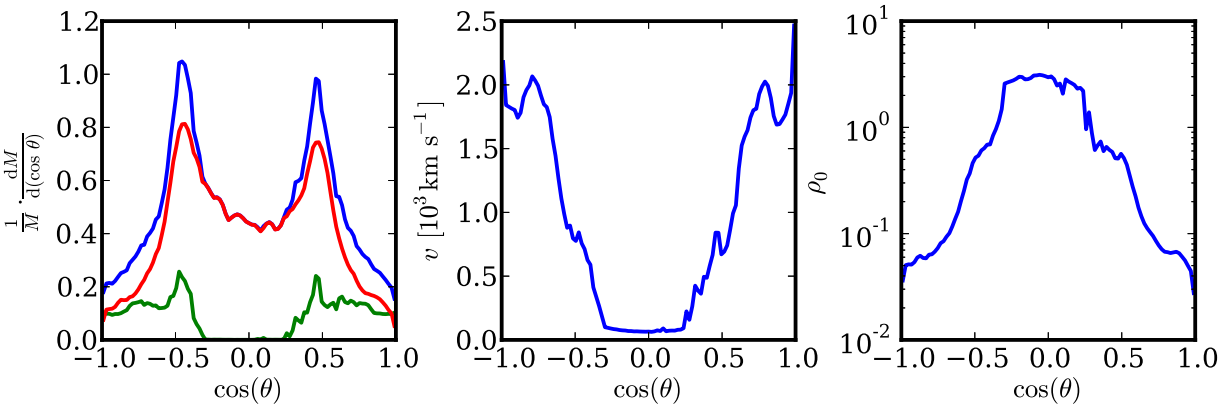

Figure 4.2: Mass distribution and velocity for the recurrent nova model as a function of polar angle. *Left*: Mass Distribution, showing the gas from the red-giant wind (red), nova (green) and total (blue). *Middle*: Average velocity of the mass as a function of angle. *Right*: Relative density as a function of angle, $\rho_0 \propto \frac{\dot{M}}{v}$.

so only the variation as a function of polar angle is needed.

Most of the mass in the recurrent nova model is contained within half of the solid angle, close to the binary plane, and the mean velocity is approximately 250 km s^{-1} (Fig. 4.2). The recurrent nova simulation uses a total mass-loss rate of $\dot{M} = 10^{-7}\,M_\odot\,\mathrm{yr}^{-1}$. This would result in a total mass of $M \sim 10^{-3}\,M_\odot$ within the approximately 15 pc that the supernova would reach in 400 yr, assuming the supernova is freely expanding. This is significantly less than the total mass in the supernova, which including the material stripped from the companion star is $M \approx 1.8 M_\odot$ and would have little effect on the supernova.

However, comparisons with observations suggest that the mass-loss rate in the wind phase may be as much as a factor of 10 higher than that used in the simulations (see Chapters 5 and 6). As the mass is much larger than the mass in the nova, this increases the total mass in the circumstellar medium for the recurrent nova by approximately a factor of 10. Also, as the nova shell dominates the momentum, momentum conservation reduces the velocity by a similar factor. The new velocity, v', is estimated to be

$$v' = \frac{v_0(m_\mathrm{N} + m_\mathrm{W}) + m_\mathrm{W} v_\mathrm{W}(f-1)}{m_\mathrm{N} + m_\mathrm{W} f}, \tag{4.1}$$

where m_N and m_W are the original mass in the wind, v_0 is the average velocity found from the simulations and v_W is the wind velocity prior to the novae, taken to be 20 km s^{-1} and $f = 10$ is

the factor that wind mass loss rate is multiplied by. We see that this gives the correct results for $f = 1$ and $f \gg 1$. The factor $f - 1$ is used because v_0 already includes a contribution to the total momentum from the wind.

The new density arising from increasing the mass-loss rate in the wind is 100 times higher than before, since the new average velocity is roughly $50\,\mathrm{km\,s^{-1}}$. This means the mass in the surrounding medium is similar to the pure wind case. However, the majority of the mass is close to the binary plane.

The interstellar medium for the nova model is constructed by first warping the uniform glass radially, as in the pure wind case. The polar angle of the particle positions is then warped to give the correct mass distribution. The initial conditions are completed by adding the supernova to the model interstellar medium, which is extrapolated to a year after the explosion and any interstellar medium particles within the supernova are removed. At this time the mass swept up is negligible compared to the supernova mass, and the density in the outer layers of the supernova is much greater than the density in the interstellar medium models, so any error introduced should be small.

4.2 Results

The evolution of the supernova into a constant density medium is shown in Fig. 4.3. Away from the hole in the ejecta, the evolution of the remnant is similar to one-dimensional models, forming spherical forward and reverse shocks. Rayleigh-Taylor instabilities cause the contact discontinuity to warp, although the evolution of the instability is suppressed since no artificial conduction has been used in the simulations (Price, 2008). At the edge of the hole, the high density region formed by the bow-shock is distorted to reduce the size of the hole at the largest radii. The radius of the forward shock is two per cent larger out at the edge of the hole, but due to the low density in the hole it is 15 per cent lower. The hole partially closes at radii larger than the radius of the contact discontinuity. While this is partially due to the initial distribution of material (see Fig. 3.3), the distortion is enhanced by Rayleigh-Taylor and Kelvin-Helmholtz instabilities.

The interstellar medium penetrates deep into the hole, driving the reverse shock into the stripped companion material. The interaction produces a distinct structure for the remnant, with the ma-

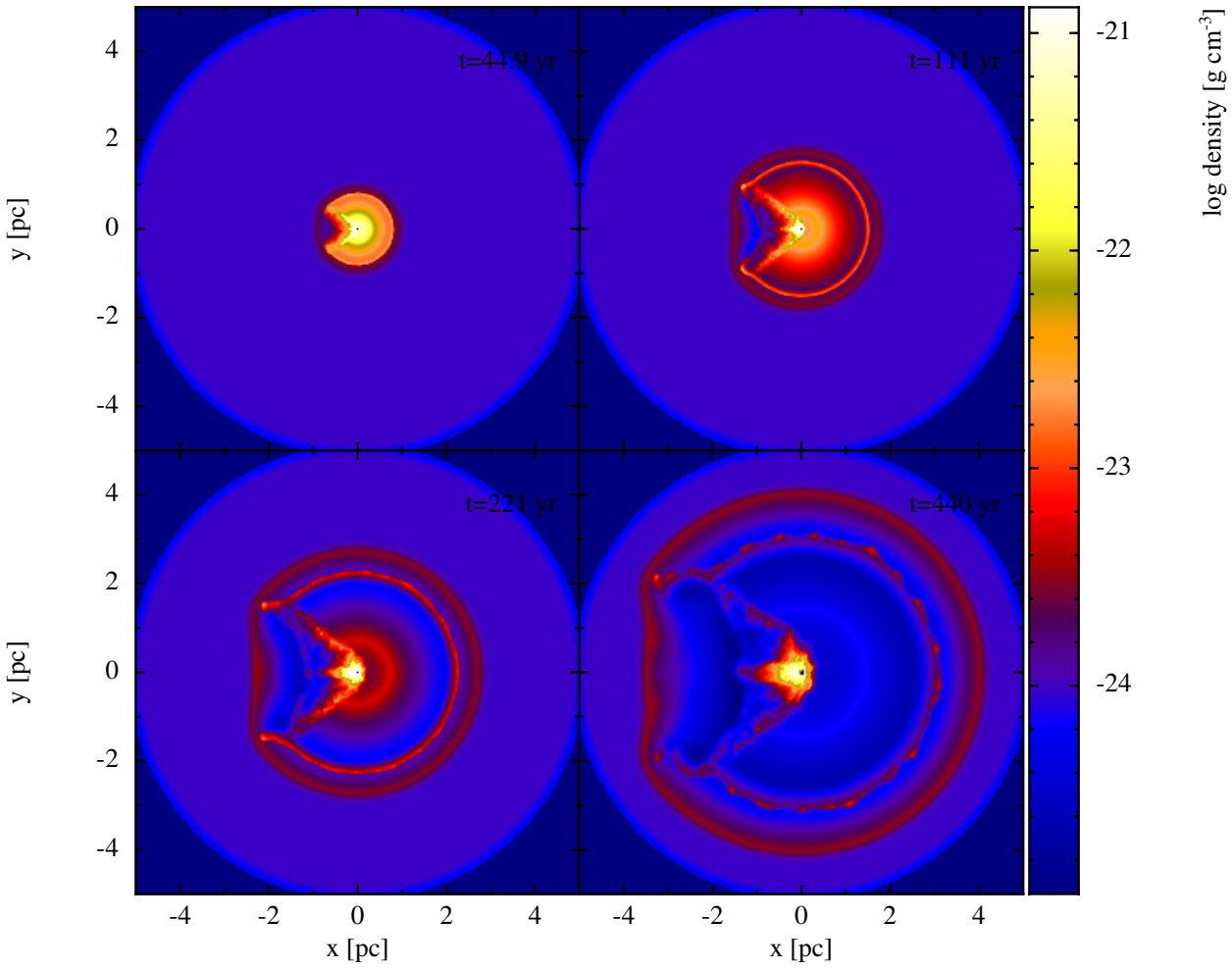

Figure 4.3: Evolution of the supernova remnant into a constant density medium up to the age of Tycho's Supernova Remnant, 440 yr. Rayleigh-Taylor instabilities are enhanced near the edge of the hole, where there is a large density gradient. Ejecta fingers can extend to the forward shock near the edge of the hole, which does not happen in spherical models of supernova remnants. By the end of the simulations the shock is starting to reach the stripped companion material.

jority of the hole filled by interstellar material. The location of the supernova, stripped companion and interstellar material is shown in Fig. 4.4. The presence of a large amount of hydrogen rich material deep within the SNR may be detectable observationally, a prospect supported by the suggestion that the shocked interstellar medium in Tycho's SNR can be traced by non-thermal X-ray emission (Warren et al., 2005). However, as the density is lower within the hole, the emission from the hydrogen rich material may be too faint.

In addition to the presence of shocked ISM deep into the remnant, the partially complete

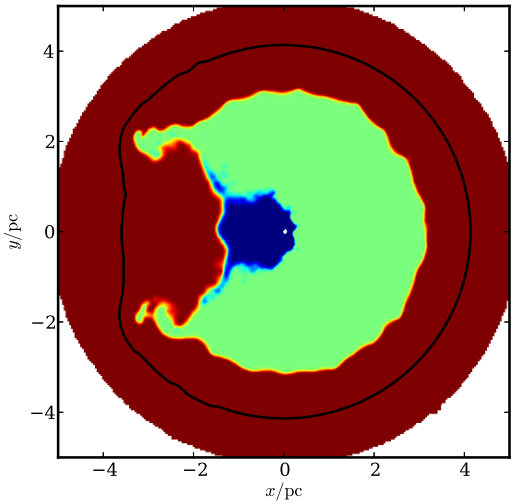

Figure 4.4: Composition of the supernova remnant for the constant density material. Blue denotes the stripped companion material, green the supernova ejecta and red the circumstellar material. The black line denotes the location of the forward shock.

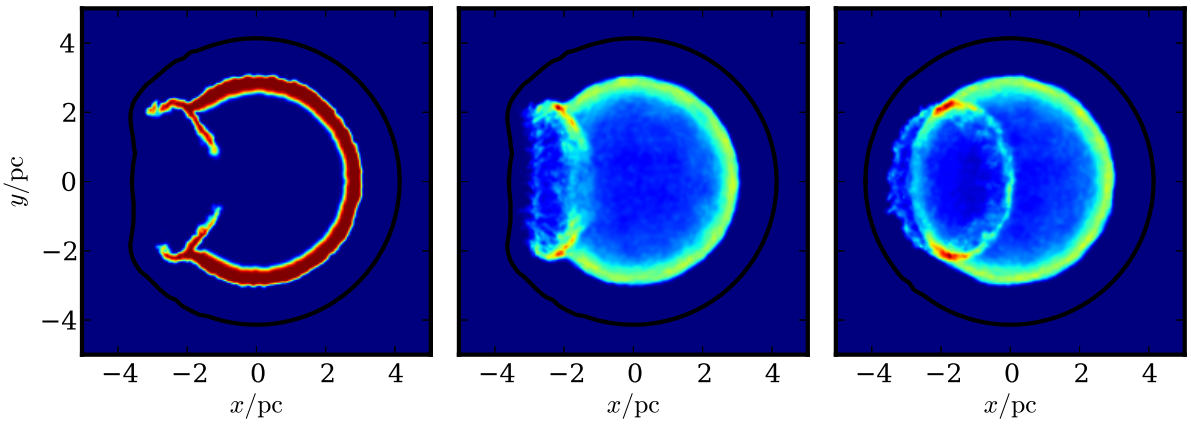

Figure 4.5: Location of shocked iron-rich ejecta in the remnant with a constant density medium. The black lines denote the location of the forward shock. *Left*: Cross-section through the ejecta. *Middle*: Column density of iron-rich ejecta at an inclination $i = 0°$. *Right*: Column density at $i = 45°$. The largest column densities are shown as red.

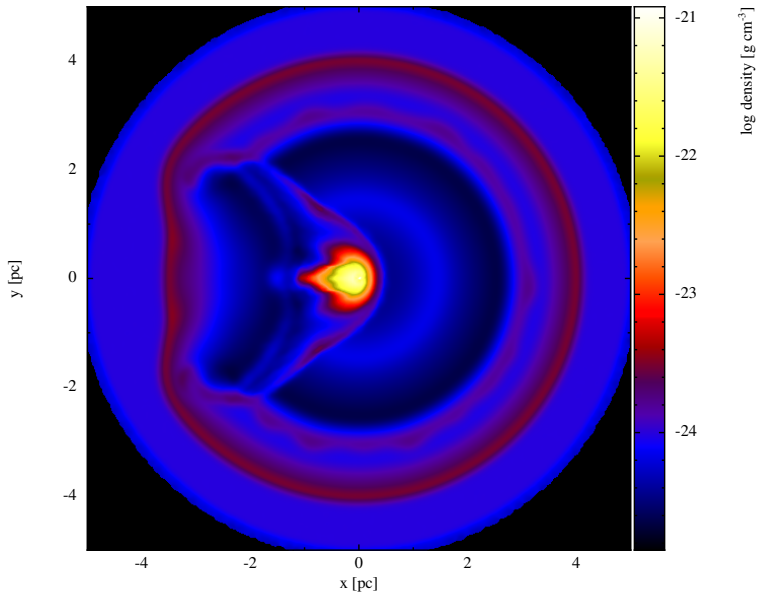

Figure 4.6: As the last panel in Fig. 4.3, but simulated using artificial conduction. The resulting structure is smoother, especially in the dense regions of the stripped companion material. The reverse shock has not penetrated as far into the hole, and instabilities are starting to grow.

reverse shock shows an interesting correspondence to the Fe Kα structure that was found by Warren et al. (2005, Fig. 4.1). The location of the shocked iron-rich ejecta in the constant density medium model is shown in Fig. 4.5, which naturally produces a ring structure for all inclinations. The models also produce a feature that arises in the bow-shock, which appears as a second, complete ring for observers viewing the for inclinations of $i \sim 45$.

Simulations have been conducted including artificial conduction to investigate the importance of instabilities. The models with conduction show similar, but smoother results. By the end of the simulation Rayleigh-Taylor instabilities are starting to grow at the contact discontinuity (Fig. 4.6). The instabilities grow more slowly than in the 2D calculations of García-Senz et al. (2012). This may be in part due to the use of three dimensions instead of two; however, the main difference is that short wavelength modes grow more rapidly, so our lower resolution means that the modes have not had sufficient time to grow. While the 2D models of García-Senz et al. (2012) show large scale instabilities at late times, these have not had time to grow by the age of Tycho's SNR.

The relatively good agreement between models that include artificial conduction and those that do not is indicative that the large scale structure is dominated by pressure forces and that

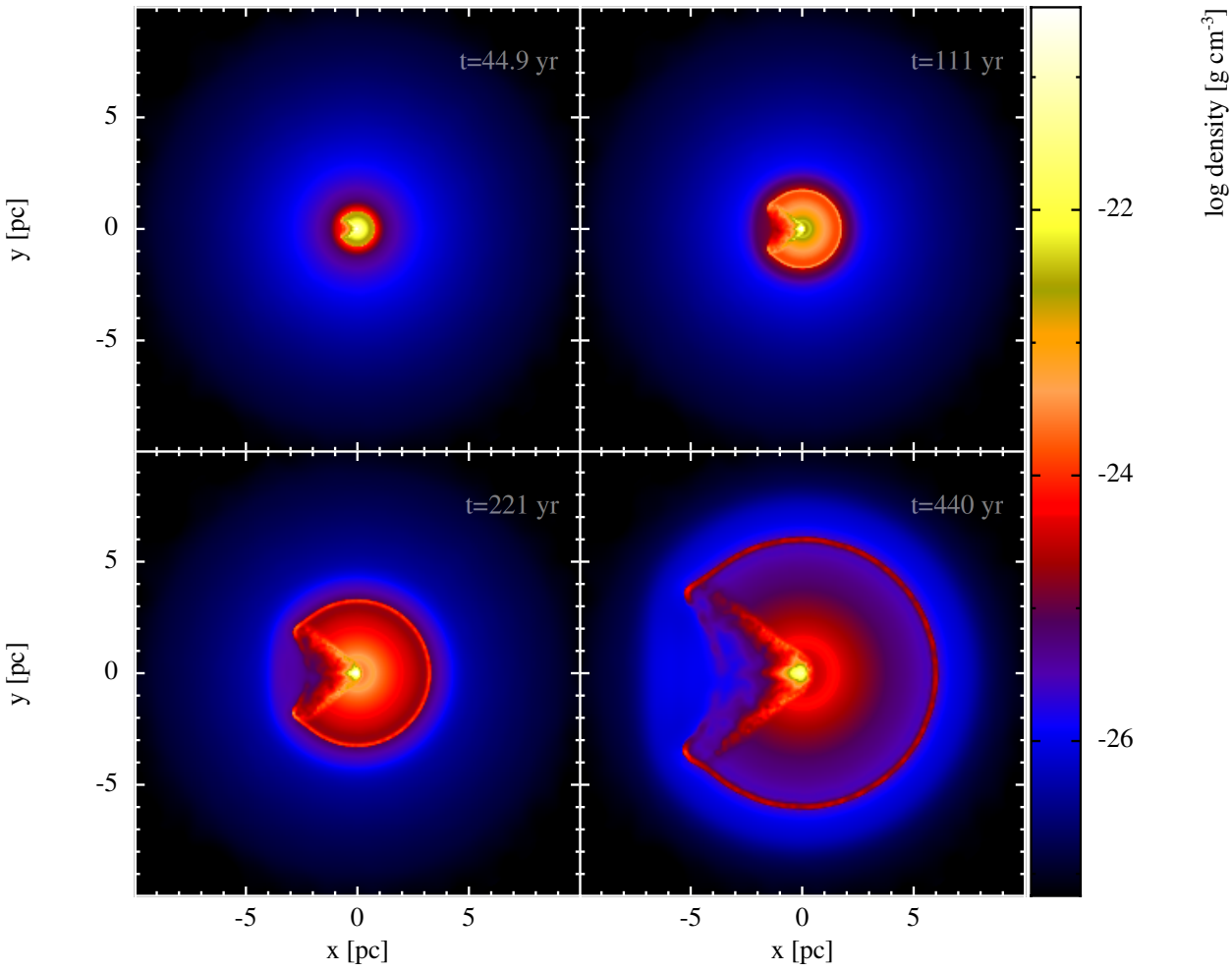

Figure 4.7: As Fig. 4.3, but the constant density interstellar medium is replaced by a $\dot{M} = 10^{-6}\,M_{\odot}\,\mathrm{yr}^{-1}$ wind.

instabilities have not affected the structure. The amount of material in the hole has biggest impact on the evolution of the remnant, with the calculations presented here most closely matching the calculations of García-Senz et al. (2012) in which the hole was partially filled with low density material.

Pure wind models differ from the constant density model mostly due to the lower mass in the circumstellar medium, resulting in a reverse shock is closer to the contact discontinuity (Fig. 4.7). The lower mass also means the reverse shock does not push as far into hole, resulting in a remnant that is slightly more spherical. However, the results are different in the non-spherical nova model, resulting in an elliptical structure for the remnant (Fig. 4.8). Observers at low inclinations

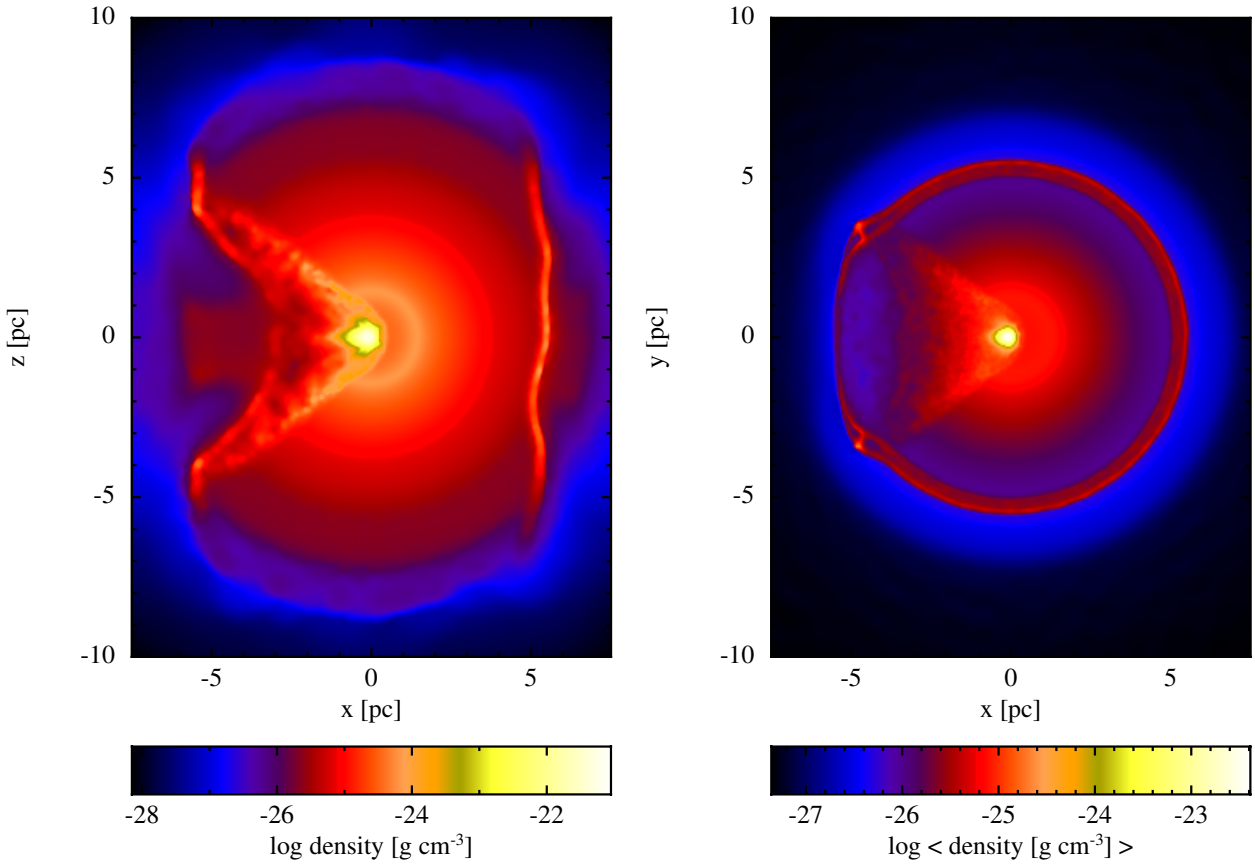

Figure 4.8: Density in the nova circumstellar model 440 yr after the supernova. *Left*: Density cross-section in the x-z plane, showing the elliptical structure. *Right*: Density averaged over the z direction, showing multiple shells in the direction of the hole.

relative to the progenitor binary would see a similar structure to the pure wind model, but with an apparently higher mass loss rate. In the polar direction and the supernova expands almost freely, while the reverse shock is driven deep into the ejecta in the plane of the binary. In contrast to the spherical cases, the density gradient causes the hole to open further in the polar directions.

4.3 Discussion

The supernova-companion interaction structure that freezes in during the first few days of the supernova survives as the supernova transition to supernova remnant, as was reported based upon simplified models. (García-Senz et al., 2012), In the constant density case, the simulation shows a similar morphology to Tycho's SNR, producing a broken reverse shock that could be traced by

the Fe Kα line (see Fig. 4.1). However, the models currently fail to explain the iron-rich knot ejected in the direction of the hole. While high density arc formed by the bow-shock helps bring supernova material closer to the forward shock, only the outer ejecta, which are not iron-rich, reach the shock front. An alternative origin for the broken reverse shock and ejecta knot may be an intrinsic asymmetry in the explosion.

While the proportion of the remnant that contains the spherical part of reverse shock is slightly larger than that seen in Tycho's SNR, the difference could be explained if the companion star was more massive and the mass ratio $q \gtrsim 1$, as this would reduce the ratio $R_{\rm RL}/a$, where $R_{\rm RL}$ is the Roche-lobe radius, and a is the separation of the binary.

A more massive companion would agree with the AGB star wind just prior to explosion, as suggested by Chiotellis et al. (2013). However, the low velocity of an AGB wind should result in it being concentrated close to the binary plane (Podsiadlowski & Mohamed, 2007, see also Chapter 5). The resulting structure of the circumstellar medium will be similar to the nova model presented, resulting in an elliptical structure for the remnant. As the structure in Tycho's SNR is not elliptical, this would suggest that we must be seeing Tycho's SNR from a low inclination. Further coincidences are two limb-brightened shocks also observed in the direction where the hole would be and the remnant also appears to be extended in that direction (Warren et al., 2005). The extension of the remnant in the direction of the hole is seen in Fig. 4.8. However, while the simulation also contain multiple limb-brightened multiple shocks in Fig. 4.8, they are commonly seen in SNRs and could be associated with variations in the interstellar medium, as could the extension of the remnant in that direction.

A further issue is that the majority of remnants of Type Ia supernovae appear close to circular on the sky (Lopez et al., 2011). While the remnant RCW 86 is elliptical (Williams et al., 2011), even its structure does not resemble that produced in the simulations. A possible way to reconcile the shapes of supernova remnants with prior AGB mass loss arises from the fact that the interstellar medium has been neglected. As the wind or novae sweep up the interstellar medium, a shell forms, which slows the wind. The shell itself will be more spherical than the current nova models, and once the supernova has reached this shell, it will interact with the unperturbed interstellar medium,

resulting in a more round remnant.

While there are some striking resemblances between the models and Tycho's SNR, there remain important differences that need to be reconciled before an AGB wind from the progenitor can be considered to be a complete explanation for Tycho's SNR. Perhaps the most important is the presence of the iron-rich ejecta knot near the rim of Tycho's SNR. While the ejecta knot may be explained assuming asymmetries in the underlying explosion, such asymmetries may also be responsible for the broken shell of reverse shocked ejecta. However, the current resemblances are promising for recurrent nova progenitors for Tycho's Supernova.

Chapter 5

RS Ophiuchi in quiescence

RS Ophiuchi (RS Oph) is an archetypal example of a potential Type Ia supernova progenitor (SN Ia) within the single degenerate channel. The high velocity and low ejecta mass during the novae, along with the orbital parameters, suggest that the white dwarf is close to the Chandrasekhar mass (Shore et al., 1996; Brandi et al., 2009). Furthermore, there is similarity between the behaviour seen in the absorption lines of RS Oph during the 2006 outburst and a few SN Ia (Patat et al., 2011). Therefore, understanding the mass transfer and formation of the line profiles during quiescence is important for understanding SN Ia.

RS Oph is an example of a recurrent nova and a symbiotic binary, a binary system which consists of a star accreting from a red giant companion. RS Oph underwent nova outbursts in 1898, 1933, 1958, 1967, 1985, and 2006; approximately every 20 years. From the high velocity and low mass ejected during the novae (Sokoloski et al., 2006; Yaron et al., 2005), it is clear that RS Oph must harbour a white dwarf with mass close to the Chandrasekhar limit. Spectroscopic determinations of the orbital parameters support this hypothesis and give a mass of $0.8\,M_{\odot}$ for the red giant (Shore et al., 1996; Fekel et al., 2000; Brandi et al., 2009).

If the red giant is filling its Roche-lobe in RS Oph, then its radius will be $105\,R_{\odot}$, which implies the star is co-rotating with the binary (Zamanov et al., 2007). However, it appears this may be inconsistent with the best estimate for the distance to RS Oph of 1.6 kpc (Barry et al., 2008). So far no ellipsoidal variations have been seen in the light-curve of RS Oph. Ellipsoidal variations are

signatures of distortion of the photosphere by a companion star, which indicate the star is close to filling it's Roche-lobe. For this reason the red giant is likely to under-fill its Roche-lobe, with mass transfer occurring by Roche-lobe overflow of its atmosphere.

The aim of this chapter is to understand how the mass-transfer and mass loss from RS Oph gives rise to line profile features in the spectra. Rather than focussing on on the entire spectra, of which large parts are dominated by the red giant and hot-component photospheres, the chapter considers the formation of individual features that cannot be attributed to either of the stars, with the aim of understanding of where and how they form in the circumstellar medium. This is done by constructing line profiles based upon the velocity distribution found from simulations of the mass-transfer.

To approach the problem, the key spectral features are described in Section 5.1. Then the mass transfer model is described in Section 5.2. The line profile features are then discussed, and a consistent picture for the circumstellar line formation is presented.

5.1 Key Spectral Features

The overall spectral properties of symbiotic systems including RS Oph have been studied in considerable detail. The defining features of the spectra are the presence of two distinct components including a hot-component from an accreting star and a component from a cool giant companion star. In many systems including RS Oph, it is not known whether the emission from the hot component comes from the star itself or whether an accretion disc surrounding the star dominates the hot component.

High-resolution spectra show strong absorption lines of Na I, Ca II and K I that have multiple components at comparable velocities to the components seen in supernovae (Patat et al., 2011). During quiescence, the blue-shifted components have velocities of up to $-50\,\mathrm{km\,s^{-1}}$. As well as the blue-shifted lines, red-shifted components are seen. While the blue-shifted lines can be attributed to absorption in an outflow at a large distance from the binary, the red-shifted component, at a velocity of $+10\,\mathrm{km\,s^{-1}}$ would not be predicted by simple models for the wind or novae. Although it may be possible that these components arise in the photosphere of the giant. In addition to the

absorption, these lines also show a broader emission component. The emission components have a full-width half maximum of approximately $100\,\mathrm{km\,s^{-1}}$, similar to that seen in emission lines of neutral helium (Patat et al., 2011; Bulla, 2013).

The three ions together provide a diagnostic for the ionization state of the gas due to their differing ionization potentials. The line profile evolution suggests that the photoionization was the main driver for the change in strength of the absorptions at $-10\,\mathrm{km\,s^{-1}}$ and $-35\,\mathrm{km\,s^{-1}}$ during the 2006 outburst. The absorption strengths of the Ca II H & K lines and Na I D lines are similar and the Ca I absorption is weaker (Patat et al., 2011). This seems to be at odds with the ionization potentials, as calcium has a higher ionization potential (6.1 eV) than sodium (5.1 eV). This implies that if the majority of calcium atoms are ionized, then sodium should also be ionized. A successful model should therefore explain why Ca II is seen at similar column densities to Na I. The same problem was found by Chugai (2008) and Simon et al. (2009) when considering the Ca II and Na I absorption in SNe Ia, who predict much stronger Ca II absorption than Na I. One possibility for the discrepancy is that both species are significantly ionized, but density of Ca II is reduced as calcium is locked up into grains, as occurs in the interstellar medium (Phillips et al., 1984).

Another line of interest is the Hα line, which probes the circumstellar medium much closer to the binary. The broad wings ($v \sim \pm 1500\,\mathrm{km\,s^{-1}}$) of the H$\alpha$ line are one of the best tracers of the velocity of the white dwarf, as they are found to be in anti-correlation with the motion of the red giant (Brandi et al., 2009). However, the central absorption of the Hα line is uncorrelated with the motion of either star. Zamanov et al. (2005) showed that the highest velocity components ($v \sim \pm 2000\,\mathrm{km\,s^{-1}}$) of the H$\alpha$ line are enhanced by components that vary on timescales in the region of a month.

The Hα line shows a central P-Cygni profile with a blue-shifted absorption with a the same velocity as the metal lines and a width $v \approx 50\,\mathrm{km\,s^{-1}}$. Traditionally, it has been suggested that the Hα may be a double peaked profile emission profile, with the central depression associated with a lack of emission rather than an absorption (e.g. Zamanov et al., 2005). However, this is not consistent with recent high-resolution spectroscopy, which shows that the flux is clearly below the continuum in the Hβ and Hγ lines (Bulla, 2013). This argument is further supported by observations after the

2006 outburst, which showed the P-Cygni profile was still present 1.5 days after the outburst, when the flux is no longer dominated by the accretion disc (Patat et al., 2011). As the P-Cygni profile had disappeared by 12 days after the outburst, the most likely explanation is that the absorption arises in material 10^{14} cm away from the binary. Furthermore, Brandi et al. (2009) observed that the central velocity of P-Cygni absorption shows no correlation with phase, supporting the suggestion that it arises away white dwarf.

Zamanov et al. (2005) suggested that the origin of the broad Hα line wings may be due to a radiation driven wind from the accretion disc. In order for RS Oph to drive such a wind, radiative acceleration must overcome the gravitational pull of the white dwarf, i.e. it must exceed its Eddington Luminosity,

$$L_{\rm Edd} = \frac{4\pi G m_{\rm H}}{\sigma_T} M \approx 3.2 \times 10^4 \frac{M}{M_\odot} L_\odot. \tag{5.1}$$

The luminosity of the hot component in RS Oph is 100 to $300 L_\odot$, well below the Eddington Luminosity for a white dwarf with $M \approx 1.4 M_\odot$. However, as disc winds are line driven, the total opacity can be much higher than Thomson scattering opacity and the effective Eddington Luminosity may be as much as a factor of 1000 to 4000 smaller (Drew & Proga, 2000). Thus it appears that RS Oph may indeed drive a disc wind.

In order to explain the recurrence time (20 yr) and ejected mass ($\sim 10^{-7}\,M_\odot$, Sokoloski et al., 2006) of the 2006 nova. the white dwarf should be accreting at $\sim 10^{-8}\,M_\odot\,{\rm yr}^{-1}$. For a system accreting at such a rate, the X-ray emission in RS Oph is surprisingly faint (Mukai, 2008; Nelson et al., 2011). The discrepancy suggests that the accretion on to the white dwarf must be relatively benign, with the gas losing most of its energy before it reaches the white dwarf, supporting the idea that an accretion disc is present in RS Oph. Thin discs in either a cold or hot state struggle to explain the accretion rate onto the white dwarf, or predict dwarf novae (Wynn, 2008), although a hybrid disc with a hot inner region and cold outer region could explain accretion rate without frequent dwarf novae. Currently the best explanation for the X-ray emission seen in RS Oph is a combination of soft X-rays emitted from the nova shell and a heavily absorbed hard component (Nelson et al., 2011). The absorbing column density for the hard component, $N({\rm H}) \sim 10^{24}\,{\rm cm}^{-2}$, is much higher than the ISM absorption. The absorption must therefore occur within the system.

While the hard component can be explained by a cooling flow, which is an X-ray emitting plasma arising from the direct accretion of gas onto the surface of the white dwarf, the required temperature ($\sim 6 \times 10^7$ K) is much lower than that expected for a gas which is shocked as it collides with the surface of the white dwarf ($\sim 7 \times 10^8$ K). Nelson et al. (2011) attribute this difference to inverse-Compton cooling, which requires an additional UV component to the luminosity of the white dwarf that arises as the white dwarf cools from the previous outburst. The accretion rate of the cooling flow model is $\dot{M} \sim 3 \times 10^{-9}\, M_\odot\, \mathrm{yr}^{-1}$, considerably less than the accretion rate required to explain the 20 yr recurrence period.

5.2 The Circumstellar Model

The simulations presented in this section were set up and run by Shazrene Mohamed, but have been described here in full for completeness. Further details of the code can be found in Mohamed (2010).

The binary system, quiescent mass loss and nova outbursts are simulated using the Smoothed Particle Hydrodynamics (SPH) code GADGET-2 (Springel, 2005), which has been modified to include binary motion, stellar winds, accretion and cooling (Mohamed, 2010; Mohamed et al., 2012). For temperatures above 10^4 K, the cooling is predominately atomic, which is implemented using the non-equilibrium ionization cooling curves from Sutherland & Dopita (1993) for a metallicity [Fe/H] $= -0.5$. At lower temperatures, cooling taking into account the fine-structure lines of C and C^+ and molecular processes based on H_2, CO and H_2O are used, as in Mohamed et al. (2012).

The cooling is thermally unstable in the temperature range $300 < T < 3000$, which leads to the formation of clumps. Physically, the size scale of these clumps is controlled by thermal conduction (Field, 1965). For gas at 10^3 K and densities of $10^9\,\mathrm{cm}^{-3}$, the conductivity, K, is dominated by ideal gas kinetics, $K \approx 2.5 \times 10^3 T^{1/2}\,\mathrm{erg\,s^{-1}\,cm^{-1}}$ Parker (1953) and clumps should form at scales $l \sim 10^{-2}$ cm and below, well below the resolution scale of the simulation.

As no thermal conduction has been added to the SPH implementation, clumping occurs at the resolution scale of the simulation, $h \sim 10^{12}$ cm. The occurrence of resolution scale clumps can be understood in terms of effective conductivity. Individual particles are described by a single temperature, which means the conductivity is effectively infinite below the resolution scale. Since there

is no conduction between particles the conductivity is essentially zero above this scale. Therefore, clumping must occur at the resolution scale since the Field length $l \propto K^{1/2}$.

The presence of clumping only has an indirect effect on the line profiles, which depend on the number absorbers and not the local density. Therefore as long as the large scale structure is resolved the line profiles are not affected by the clumping. However, this is not the case for recombination calculations, which depend on the density. Since photoionization equilibrium gives rise to temperatures of approximately $10^4\,\mathrm{K}$ and at such temperatures the gas is thermally stable, photoionization calculations are not sensitive to the occurrence of clumping in the dense regions. Therefore, the presence of thermal instabilities should not greatly affect the results.

The binary parameters are chosen to be suitable for a recurrent nova progenitor for SN Ia, whilst remaining consistent with observational constraints on RS Oph. We choose the masses $M_{\mathrm{WD}} = 1.38 M_{\odot}$, $M_{\mathrm{RG}} = 0.8 M_{\odot}$ and separation $a = 1.48\,\mathrm{AU}$ to give a period of 453.6 days. The mass loss rate from the red giant is taken to be $\dot{M} = 10^{-7} M_{\odot}\,\mathrm{yr}^{-1}$. The mass loss is modelled by injecting the particles close to the surface of the red giant, which has a radius of $100\,R_{\odot}$. The particles are injected with a low velocity, $v = 20\,\mathrm{km\,s}^{-1}$, which is much less than the escape speed at the surface, $v_{\mathrm{esc}} \approx 55\,\mathrm{km\,s}^{-1}$. The particles are then accelerated by the binary potential. Any mass-loss from the white dwarf due to jets or a disc-wind has been neglected. As the surface of the white dwarf is not resolved in the simulations, accretion on to the white dwarf is handled by slowly decreasing the mass of particles that come within 0.2 AU it, removing them once their mass becomes less than 1 per cent of their initial mass.

The large-scale structure formed after 13 orbits is shown in Fig. 5.1. Two spiral arms are formed, which merge after roughly an orbit. The resulting structure at large distances is a single-armed spiral. The spiral remains confined to the binary plane and becomes clumpy, driven by radiative cooling. While the occurrence of clumping is physical, the clumps themselves arise on the resolution scale $l \sim 10^{12}\,\mathrm{cm}$, rather than the physical scale given by the Field Length $l \sim 10^{-2}\,\mathrm{cm}$ (Field, 1965).

The interaction region between the wind and the binary is shown in Fig. 5.2. The plane of the binary orbit is the x-y plane, with the red giant at $x < 0$ and the white dwarf at $x > 0$. Due to the low injection velocity, the majority of the mass lost from the red giant escapes through the inner

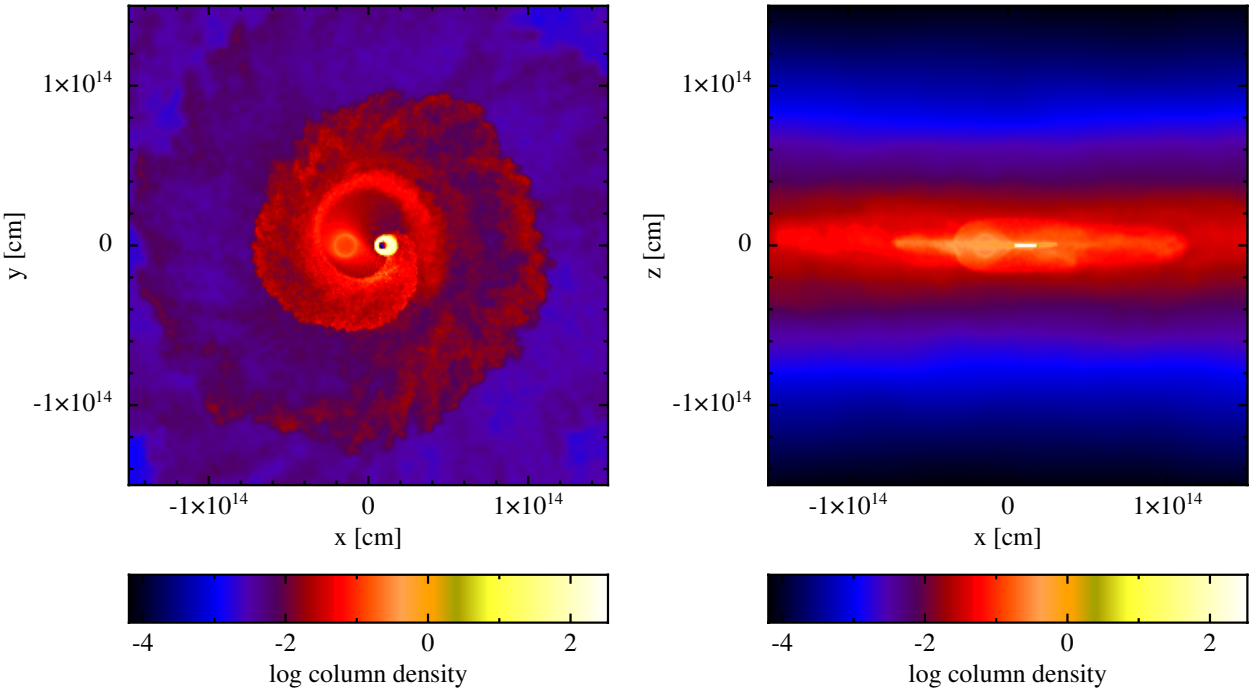

Figure 5.1: Column density during quiescent mass transfer, showing the two-armed spiral structure. The two spirals merge after approximately one orbit. The spiral structure is long-lived, but forms clumps driven by the radiative cooling. The column density is in $\mathrm{g\,cm^{-2}}$.

Lagrange Point (L1) and passes close to the white dwarf, in a similar process to classical Roche-lobe overflow. An accretion disc is formed, along with the two spiral arm streams. The outer parts of the accretion disc are eccentric, with the semi-major axis staying aligned with the binary. The hole in the accretion disc arises due to treating the white dwarf as a sink. In simulations without cooling, an accretion disc does not form (Theuns & Jorissen, 1993).

While some of the gas passing near the white white dwarf becomes entrained in the accretion disc, the gas that is not captured escapes escapes the binary through the L3 Lagrange point. As this material leaves the binary it runs into the gas in the second stream and is shocked, which can clearly be seen by the discontinuous velocities. Rapid cooling of post-shock gas leads to instabilities and causes the gas to clump. The second spiral forms as the wind runs into the gas trailing the white dwarf. The wind remains focussed in the binary plane and is approximately in free expansion once it has reached a few times the binary separation.

The x-z cross-section shows the outflow is strongly confined to the orbital plane, with the density dropping by two orders of magnitude within a few $10^{13}\,\mathrm{cm}$. At higher $|z|$, gas is falling back onto

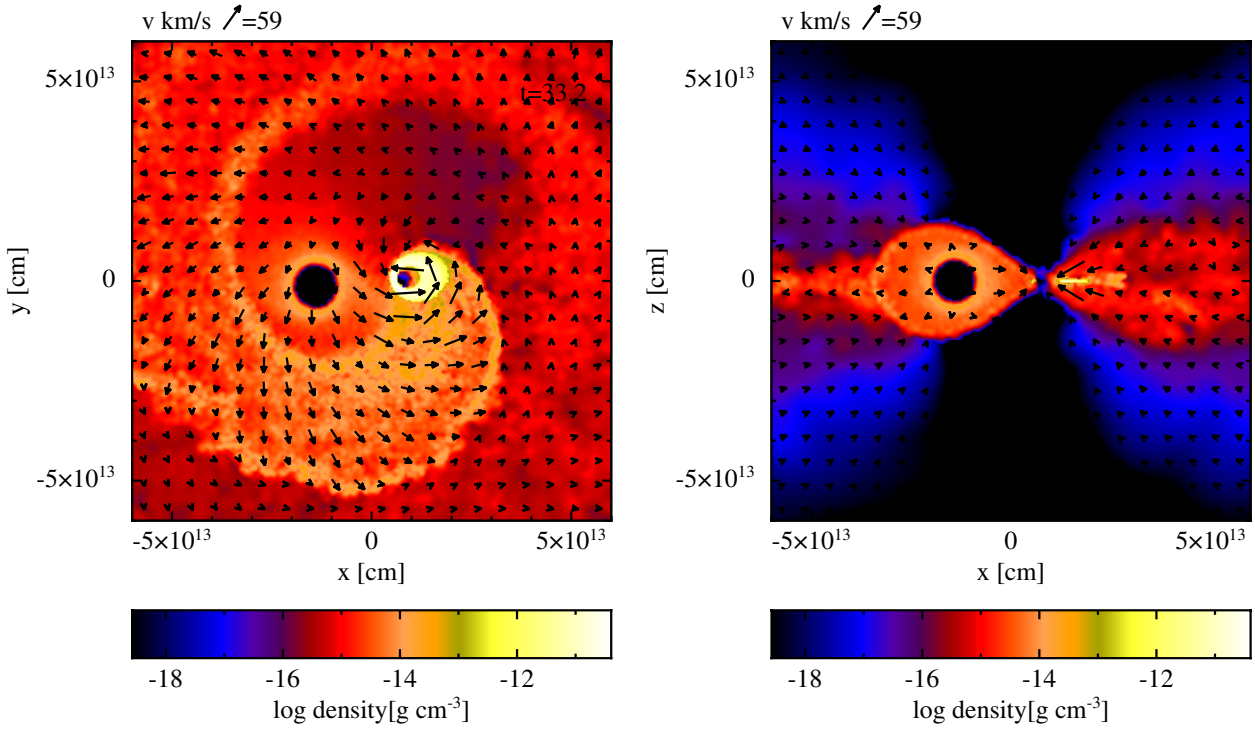

Figure 5.2: Density cross-sections during the quiescent mass transfer phase. Velocity vectors are in the inertial frame. The plane of the binary orbit is the x-y plane and the red giant and white dwarf lie on $y = z = 0$. The red giant is to the left of the white dwarf and the centre of mass of the system is at the origin. The binary interaction shapes the wind into a spiral, which is confined to the equatorial plane. In the x-y plane the two-armed spiral structure formed by the motion of the binary can be seen, along with an eccentric accretion disc. The low density at the centre of the accretion disc arises as a result of treating the white dwarf as a sink. The x-z cross-section shows material falling onto the binary from above the plane.

the binary. Most of this gas arises from the passage of the white dwarf through the red giant wind, which forms a bow shock around the white dwarf and accretion disc. Additionally, there is a small amount of material falling back from further out of the plane. This flow comes from further out in the plane and is more prevalent in the simulation with suppressed cooling, which can be seen more easily in Fig. 5.3.

The suppressed cooling model is included for comparison because the system contains a hot white dwarf and accretion disc, which provide additional heating that has been neglected in the main model. Dobrzycka et al. (1996) estimate luminosity and temperature of the UV emission from the white dwarf and accretion disc using two methods. They integrate the IUE observations of the UV continuum prior to the 1985 outburst, which gives a luminosity, $L_{\rm UV} \sim 100 - 600\,L_{\odot}$,

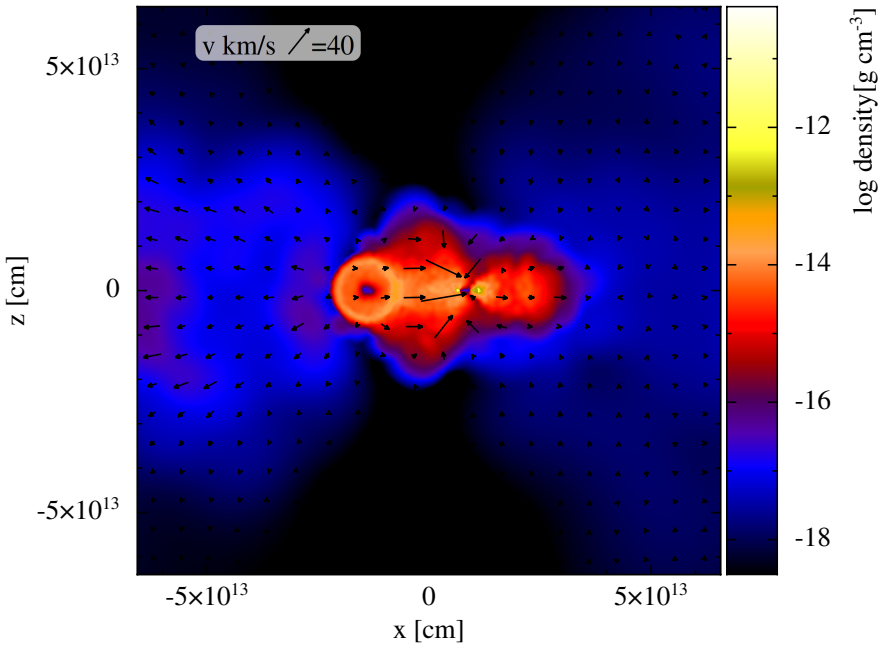

Figure 5.3: Density cross-section in the x-z plane, for the simulation in which cooling has been switched off close to the binary. The flow between the red giant and white dwarf is more diffuse as the additional pressure stops the gas from collapsing. Otherwise the main features are the same. Spatial units are 2 AU.

where $L_\odot$ is the solar luminosity, and temperature, $T \sim 2 \times 10^4$ K. They also give an estimate based on the optical emission lines of H and He, which gives $L_{\rm UV} \sim 100 - 300\, L_\odot$ and temperature, $T \sim 4 - 5 \times 10^4$ K. As the UV continuum is strongly sensitive to interstellar reddening, we prefer the estimate based upon the emission lines. This can be compared with an estimate based upon the accretion rate

$$L = f\frac{GM\dot{M}}{R}, \tag{5.2}$$

which for $M = 1.4 M_\odot$, $\dot{M} = 10^{-8} M_\odot\,{\rm yr}^{-1}$ and $R = 0.01 R_\odot$ gives $L \approx 1000 f L_\odot$, i.e. $f = 0.1 - 0.3$. Photoionization is expected to drive the gas to a temperature of a few 10^4 K, which is consistent with the temperature estimated by Dobrzycka et al. (1996).

The effect that heating has on the structure have been assessed using a simulation that has the cooling switched off close to the binary. As shown in Fig. 5.3, the x-y structure is largely similar to Fig. 5.2, but the escaping wind has a much larger scale height. There is also an envelope that surrounds the binary that appears as the gas is unable to cool and collapse. This increases the

amount of gas that falls onto the white dwarf and the accretion disc from above and below the binary plane. The accretion disc is also thicker, and the maximum densities are lower.

5.3 Ionization Structure

In order to understand the line profiles formed in the circumstellar gas, it is necessary to understand the ionization conditions. The ionization is calculated using a pseudo-1D Strömgren-sphere approximation, where lines of sight through the gas are treated as independent spheres, which neglects the effects of radiative diffusion. Only hydrogen has been included in the calculation. The relevant physical processes include collisional and photoionization, recombination, heating and cooling. The photoionization cross section is taken from Verner et al. (1996). The recombination rates assume the Case B approximation, in which recombinations to the ground state are neglected ('On-The-Spot' approximation) and are taken from Hui & Gnedin (1997). Collisional ionization is generally dominated by photoionization, but is included according to Cen (1992). Three-body recombination has been neglected, although it dominates radiative recombination for $n_e \gtrsim 10^{12}\,\mathrm{cm}^{-3}$. These densities are reached in the accretion disc; however, as the disc remains neutral the error introduced into the ionization fraction does not affect the opacity, which is approximately constant for $x_e \ll 1$.

Heating due to photoionization is included per H-atom according to

$$\Gamma_0 = \int_{\nu_\mathrm{H}}^{\infty} F_\nu \sigma_\nu h(\nu - \nu_\mathrm{H})\,\mathrm{d}\nu, \tag{5.3}$$

where $h\nu_\mathrm{H} = E_\mathrm{H} = 13.6\,\mathrm{eV}$, σ_ν is the photoionization cross section, n_H is the density of neutral hydrogen and F_ν is the flux. Cooling due to recombination is included according to Hui & Gnedin (1997) and collisional excitation cooling and collisional ionization heating are from Cen (1992), which assumes that the cooling gas is optically thin. The cooling approximations used here apply to optically thin gas in HII regions and will over-estimate the temperatures in the neutral parts of the wind, where molecular and fine structure cooling are dominant. However, as the recombination rate is not very sensitive to temperature, the ionization fraction is reliable, which has been can be verified by artificially reducing the cooling rate.

The equations which need to be solved at each location are

$$\frac{\mathrm{d}n_\mathrm{e}}{\mathrm{d}t} = n_\mathrm{H} f + n_\mathrm{e} n_\mathrm{H} C(T) - n_\mathrm{e}^2 \alpha(T)), \tag{5.4}$$

$$\frac{\mathrm{d}T}{\mathrm{d}t} = \frac{2}{3nk_\mathrm{B}}(\Gamma_0 n_\mathrm{H} - \Lambda(T)) - \frac{T}{n}\frac{\mathrm{d}n}{\mathrm{d}t}, \tag{5.5}$$

where $f = \int_{\nu_\mathrm{H}}^{\infty} F_\nu \sigma_\nu \, \mathrm{d}\nu$ is the photoionization rate per atom. As Γ_0 and f are constant for a given flux, the equilibrium ionization state at a given temperature can be solved analytically because the first equation reduces to a quadratic equation for the ionization fraction, $X(T)$. The second equation can then be solved numerically to find the temperature.

The lines of sight are taken through the circumstellar medium from the white dwarf to each particle. The fluid properties along a line of sight are evaluated at points selected using the algorithm described in Section 2.3.1, which is based upon Kessel-Deynet & Burkert (2000). For each radial bin the flux is calculated according to $F_\nu = \frac{L_\nu}{4\pi r^2} \exp(-\tau_\nu) \frac{1-\exp(-\Delta\tau_\nu)}{\Delta\tau_\nu}$, where the last term takes into account the finite depth across the cell. This is needed to ensure conservation of photon number in cells of finite optical depth and results in the need to iterate the solution until the ionization fraction converges.

In principal the algorithm can be accelerated. Rather than solving one Strömgren sphere problem for the line of sight to each particle, a single line of sight could be used for all particles sufficiently close to it. In practice this has not been done because a local criterion based upon the distance to the line does not guarantee consistency and as the ionization is calculation is done by post-processing the simulation, the efficiency is not an issue because the calculations take only a few hours.

The ionization fraction for the model of RS Oph is shown in Fig. 5.4, which has been calculated assuming a luminosity of $100 L_\odot$ and temperatures of $T = 4{\times}10^4\,\mathrm{K}$ and $T = 10^5\,\mathrm{K}$. The temperature estimate from photoionization models of RS Oph is $4{\times}10^4\,\mathrm{K}$ (Dobrzycka et al., 1996). The ionization pattern is a distinctive x-shape in cross section, which arises because the luminosity is sufficient to fully ionize the diffuse material in the polar directions. The accretion disc and the wind close to red giant are dense enough to shield the material close to the plane, which remains neutral. In three dimensions, the ionization pattern is conical, centred on the white dwarf. The opening angle of the

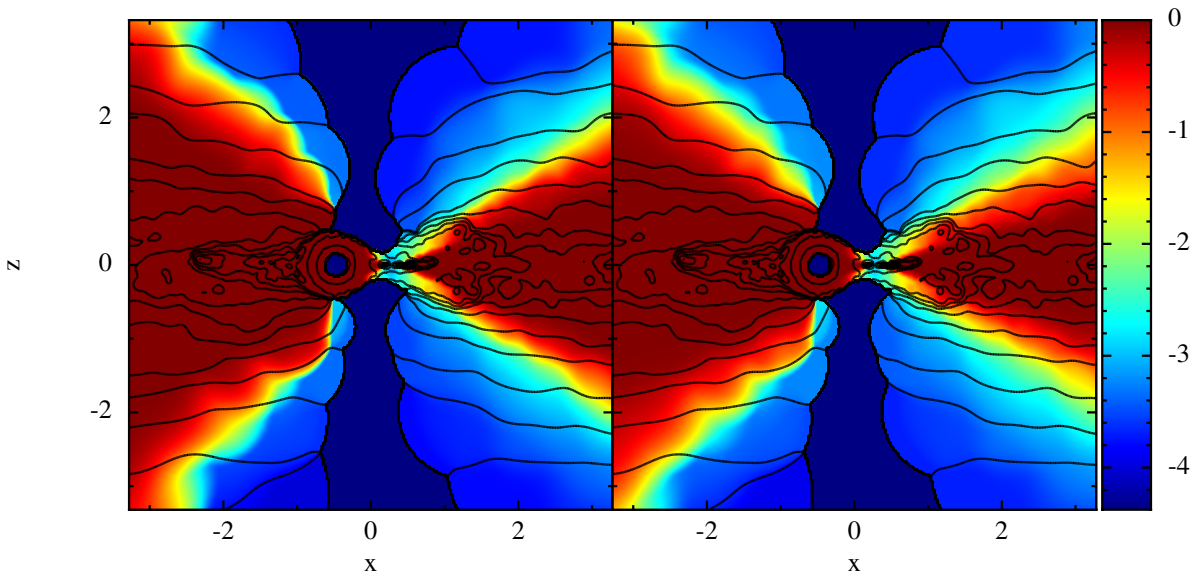

Figure 5.4: Ionization of hydrogen by the white dwarf for a cross-section through the white dwarf and red giant. The white dwarf is assumed to emit a black-body spectrum with $L = 100 L_{\odot}$. The black-body temperatures are $T = 4 \times 10^4\,\mathrm{K}$ (left) and $T = 10^5\,\mathrm{K}$ (right). Contours show the density in logarithmic bins and colours denote the logarithm of the neutral hydrogen fraction. Spatial units are in code units, which are 2 AU. The three-dimensional ionization structure is conical centred on the white dwarf, although the opening angle of the cone decreases towards the red giant.

cone decreases towards the red giant, as can be seen in cross-section.

As the majority of the mass lost from the binary remains close to the binary plane, the white dwarf only ionizes a few per cent of the mass in the wind. Although the differences are minor, the higher temperature model ionizes a slightly wider cone. This is due to the lower cross-section associated with higher energy photons, which means that the effective opacity of the accretion disc is less for the $10^5\,\mathrm{K}$ model.

The red giant shields a fraction of the wind, creating an axial asymmetry that raises the question as to whether the approximation of steady state is reasonable. The density in the wind stays above $10^6\,\mathrm{cm}^{-3}$, except high above the plane ($|z| \gtrsim 10^{14}\,\mathrm{cm}$) where there is little mass in the wind. Therefore, the recombination timescale, $t_r = \frac{1}{n\alpha} \lesssim 10\,\mathrm{day}$, is much less than the orbital period, justifying the use of the steady-state approximation. The ionization structure is not particularly sensitive to the ionizing flux, as the thickness of the accretion disc controls the volume of ionized material. The biggest differences appear near the red giant, where an increased ionizing flux results in a smaller region that is shadowed by the red giant.

5.4 Sodium Absorption Lines

Absorption lines are independent of the source luminosity, making them a useful way to identify the CSM in both supernovae and their progenitor systems. Sodium D lines make a good choice for this comparison because they are strong and have been detected in several SNe Ia, including some in which the lines showed variation (e.g. Patat et al., 2007; Blondin et al., 2009; Simon et al., 2009). While the relative strengths of the Na D line, and the Ca II H & K line is a useful diagnostic for the ionization conditions in the circumstellar medium, the main focus will be on the Na D lines. The Ca II H & K lines will be discussed in relation to the results obtained for the Na D lines.

The absorption line profiles are modelled by considering the optical depth to the photosphere as a function of frequency, $\tau_\nu = a_0 f \int n_{\mathrm{Na}}(s)\phi(\nu)\,\mathrm{d}s$. The atomic absorption coefficient $a_0 = 0.0265\,\mathrm{cm^2\,s^{-1}}$, the oscillator strength $f = 0.641$ for the Na D_2 line and $\phi(\nu)$ is the Doppler profile. The number density of sodium atoms in the ground state is given by n_{Na} and the sodium abundance is taken to be solar (Asplund et al., 2009). The relative intensity is given by $I_\nu = \frac{1}{A}\int \exp(-\tau_\nu)\,\mathrm{d}A$. Lines of sight to the photosphere are adaptively divided until the width of the region is smaller than some fraction of the minimum smoothing length, taken to be 0.25.

The contribution to the line profile from gas $r > 5 \times 10^{14}\,\mathrm{cm}$ has been ignored. This material comes from the first orbit of the simulations and follows a $v \propto r$ velocity law, rather than the constant velocity reached by the mass loss for subsequent orbits. The structure of this material is likely to be an artefact of the initial conditions, which is why it is not included. This only affects profiles with inclinations $i \gtrsim 70°$, otherwise the density is too low by the time the line of sight reaches the material.

As the continuum around the Na D line is dominated by the red giant during quiescence, the photosphere is taken to be the photosphere of the red giant ($100R_\odot$). Three models for the sodium ionization structure are used. One model uses the ionization structure from the photoionization calculation. Sodium is assumed to be ionized in the regions of hydrogen ionization because the ionization potential of sodium (5.1 eV) is lower than that of hydrogen (13.6 eV). In neutral regions local thermodynamic equilibrium (LTE) is assumed, which roughly translates to sodium being ionized where $T > 1000\,\mathrm{K}$. In the second model, designed to help disentangle the location of the

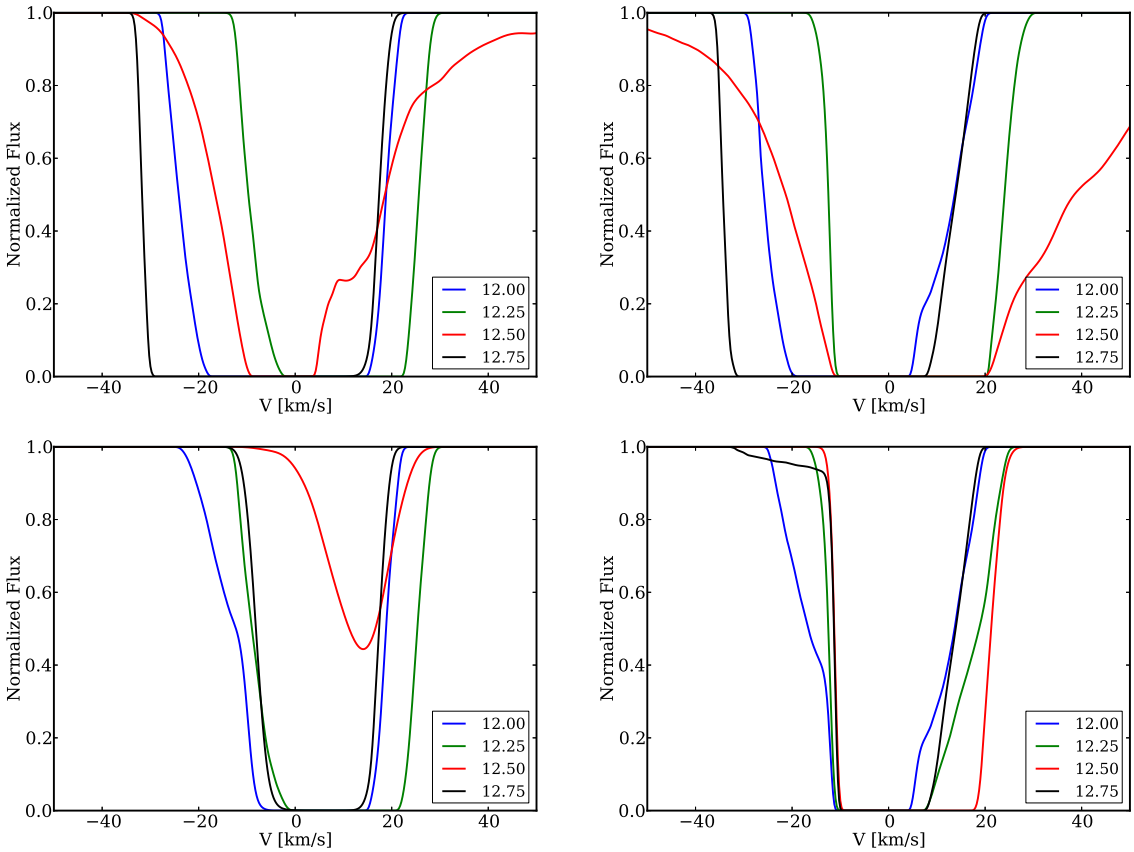

Figure 5.5: Na D line profile evolution with phase, for the photo-ionized models (upper) and for photoionization + bubble (lower). The key denotes the number of orbits since mass transfer began. At phase 0 the red giant is closest to the observer. The line profile is calculated for inclinations of 60° (left) and 75° (right). For $i \lesssim 50°$ the blue-shifted absorption components disappear, except for phases 0.9 to 0.1, when the red giant shields the wind. The effects of shielding by the red giant can be seen in the $i = 60°$ profile. At $i = 75°$ the accretion disc also shields the gas, resulting in a stable blue-shifted component. The red-shifted component that arises in the polar accretion flow is less sensitive to inclination.

different components, the white dwarf is also assumed to ionize a few 10^{13} cm bubble around the binary, in which the neutral fraction is assumed to be zero. In the third model, the fraction of neutral sodium is limited to 10^{-4}.

The results from the photoionized models are shown in Fig. 5.5. The line profiles show both blue- and red-shifted components, which form in different parts of the wind. In the regions of the wind furthest away from the binary, where the gas is flowing radially, the lines of sight always intersect the same clumps of gas. This gives rise to a stable blue-shifted component in the profile,

which can be seen in the photoionization + bubble models. An additional blue-shifted component arises in the wind near the red giant. The gravitational acceleration from the white dwarf results in higher velocities towards the white dwarf than away from it, giving the highest velocity for phases $\phi \sim 0.5$. The strength of this component is not symmetric about $\phi = 0.5$, which is expected as the flow itself is not symmetric due to the motion of the binary. Observationally, this component may be difficult to disentangle from the component arising in the atmosphere of the red giant.

The red-shifted component forms closer to the binary, in the material falling back onto the white dwarf from within a few 10^{13} to 10^{14} cm. The component is strongest for phase $\phi = 0.5$, when the red giant is furthest from the observer. In this case the line of sight passes over the white dwarf, and through more of the material falling back onto the white dwarf. The exception to this case is at lower inclinations, in the photoionization + bubble model, because at low inclinations the line of sight is high above the plane and encounters very little material outside the ionized bubble. The near complete lack of material outside the ionized bubble for lower inclinations may be an artefact of the cooling, as the simulations with suppressed cooling have considerably more gas in this region. In line profiles calculated using this model, we find that the red-shifted absorption is strongest near phase $\phi = 0$ for all inclinations.

The line profiles show strong variation with inclination, with the highest outflow velocities seen at the highest inclination (Fig. 5.6). The inflow components vary in the opposite sense, almost disappearing for $i = 90°$. The variation is naturally explained by the increasing column depth at high inclination.

The line profiles show good qualitative agreement with RS Oph, providing a robust explanation for the red-shifted absorption component seen in the Na I, Ca II and K I lines. This component cannot be explained by one-dimensional models for a wind, which provides strong support for the spiral outflow produced in the model. Since the velocities of the absorption components observed in RS Oph are stable, the models show that they must form further out in in the wind, as components that form close to the binary depend on the phase. This argument is supported by the suggestion that the evolution of these features during outburst is dominated by photoionization (Patat et al., 2011). As the blue-shifted components can still be seen at 12.5 days after the outburst this means

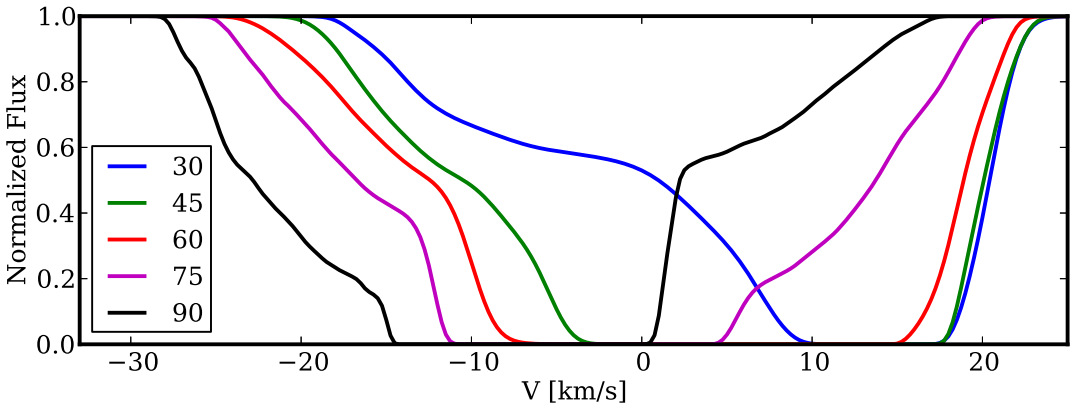

Figure 5.6: Na D line variation with inclination at phase 0, for the photoionization + bubble model. The blue-shifted components are strongest for high inclinations, where additional features can be seen, whereas the red-shifted components weaken at the highest inclinations.

they must form at distances greater than a few 10^{14} cm. Furthermore, the observations are consistent with the red-shifted completely disappearing during nova outburst, which would be expected as the novae sweep up the infalling gas close to the white dwarf.

In addition to absorption component, the simulations suggest a possible origin for the emission component seen on top of the absorption lines (Bulla, 2013). The emission components have a typical width of $100\,\mathrm{km\,s^{-1}}$, larger than that for the absorptions. The most likely origin for these lines is that they arise in the ionized flow close to the white dwarf, that gives rise to the time-variable absorption seen in the photoionization only models in Fig. 5.5. This material has approximately the right velocity to produce the broad emission, and is likely to be ionized by the white dwarf. Combined with its high density, this material is the most likely origin for the emission components.

The maximum velocity produced in the outflow is $v \sim 15\,\mathrm{km\,s^{-1}}$, which is considerably less than the 40 to $50\,\mathrm{km\,s^{-1}}$ seen in RS Oph. As the orbital velocities in RS Oph are relatively well known (Brandi et al., 2009) and the velocity of the outflow is set by the orbital motion, the high velocity cannot be produced by the mass-transfer models. Furthermore, using a higher red giant velocity to produce the outflow would destroy the spiral structure and the red-shifted absorption would not be produced. One possibility is that these components form in the shells of previous novae, which has not been included in these calculations but will be discussed in the next chapter.

The presence of disc-winds, may also provide an explanation for difference in the observed

velocity and the velocity produced in the simulations. Simulations of disc winds in cataclysmic variables the disc wind can drive mass-loss rates of $10^{-10} M_\odot\,\mathrm{yr}^{-1}$ at velocities up to $5000\,\mathrm{km\,s}^{-1}$ (Proga et al., 2002). In RS Oph this momentum would be ultimately deposited in the red giant. While this is not sufficient to provide a kick of $20\,\mathrm{km\,s}^{-1}$ to the entire wind, it could accelerate up to $10^{-8} M_\odot\,\mathrm{yr}^{-1}$ by $20\,\mathrm{km\,s}^{-1}$. Due to the concentration of most of the mass-loss in the binary plane, such a scenario may be likely. Therefore, the inclusion of a disc wind may be able to remove the discrepancy between the velocities produced in the simulation and those observed in RS Oph.

The inclinations favoured by the line profiles are $i > 60°$, which is higher than the inclination suggested by the orbital parameters $i \approx 50°$ (Brandi et al., 2009). The higher inclination is favoured by the simulations as the line of sight needs to intersect the neutral material in the region shielded by the accretion disc. At lower inclinations $i \lesssim 45°$, the column depth becomes too low to produce the required absorption, even if the gas was shielded by a thick disc. However, in the models with suppressed cooling there is more mass at lower inclinations, which suggests that in reality the column depth at lower inclinations is high enough.

The line profiles produced by these models include components that are strongly saturated ($\tau \sim 10^3$), which arise far out in the wind. Due to the use of a Doppler profile, this broadens the components by roughly $3\,\mathrm{km\,s}^{-1}$ (Fig. 5.7). Such strongly saturated components disagree with the observations. If the full Voigt profile for the lines had been used instead of a Gaussian profile the line profile would be much broader and dominated by the wings of the Voigt profile, which decays much more slowly in the line wings $\phi_{\mathrm{voigt}} \propto (\nu - \nu_0)^{-2}$. A lower mass loss rate would remove this discrepancy; however, the white dwarf must accrete enough mass in 20 yr to trigger the novae. This means the accretion rate must be at least $\dot{M} \sim 10^{-8}\,M_\odot\,\mathrm{yr}^{-1}$. As the accretion efficiency is already roughly 10 per cent, this would be somewhat fine tuned as only a small fraction of the mass loss could escape.

An alternative suggestion is that the ionization fraction in the neutral regions is considerably less than unity, which is supported by the presence of the Ca II absorption. Using spherical models Chugai (2008) found that for mass loss rates $\dot{M} \gtrsim 10^{-7}\,M_\odot\,\mathrm{yr}^{-1}$, the density is high enough that hydrogen is neutral in the outer regions but the fraction of neutral sodium is as little as 10^{-4}. Model

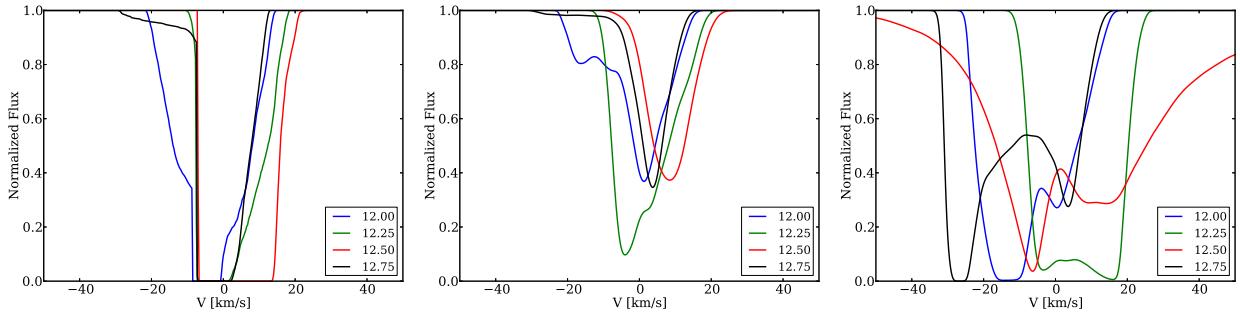

Figure 5.7: Sodium D line profiles in the photoionization + bubble (left, middle) and pure photoionization (right) models. The inclination, $i = 75°$. *Left*: Using a narrow intrinsic line profile, which produces saturated components that are narrower by a few $\mathrm{km\,s^{-1}}$. *Middle, Right*: The neutral fraction of sodium is limited to 10^{-4}.

line profiles at $i = 75°$ are shown in Fig. 5.7 that have the neutral fraction of sodium limited to 10^{-4} . The optical depths are considerably lower, with $\tau < 1$ and no stable component is produced in the outer wind. For an inclination $i = 45°$ the profile is even weaker.

The simulations can be brought into line with the observations if the mass loss rate is a factor of ten higher. If the density distribution of escaping gas is more like that seen in the models with suppressed cooling, then a total mass loss rate of $10^{-6}\,M_\odot\,\mathrm{yr}^{-1}$ would produce an effective mass loss rate of $10^{-7}\,M_\odot\,\mathrm{yr}^{-1}$ at an inclination of 45°, which would be enough to ensure that hydrogen is neutral for $r \gtrsim 10^{14}\,\mathrm{cm}$. The extra mass would produce moderately saturated profiles for moderate ionization fractions and at lower inclinations. Photoionization of the material near the binary that is dense enough to absorb the UV flux would produce an ionization structure similar to the bubble model, producing components that form far out in the wind. The similar strength of the Ca II lines to the Na I in this region supports the idea that calcium is depleted by dust. NIR observations of RS Oph suggest that dust forms at $r > 10^{14}\,\mathrm{cm}$ (Evans et al., 2007), which is consistent with the hypothesis that the Na lines should form further out.

5.5 Polar accretion and Hα emission

Accretion happens through two modes in the simulations. Firstly, an accretion disc forms containing approximately $10^{-7} M_\odot$. Secondly, there is a polar component to the accretion flow that arises out of the material falling from above and below the binary plane. The accretion rate in the polar flow

is $\dot{M} \sim 4 \times 10^{-9} M_\odot \,\mathrm{yr}^{-1}$ in the canonical model. In the model that has suppressed cooling, the polar accretion rate is approximately twice as large.

A polar accretion flow may provide an explanation for the wings of the Hα line seen in RS Oph during quiescence. The broad wings ($> 1500\,\mathrm{km\,s}^{-1}$) have been observed to correlate with the motion of the white dwarf (Brandi et al., 2009). The polar inflow is modelled assuming the material is in free-fall, with the accretion rate set by the parameters from the simulation. The geometry is chosen to be conical or spherical and the Hα emissivity is assumed to be proportional to the Case B radiative recombination rate, while the inflow is assumed to be optically thin. As the recombination time is much shorter than the free fall time, the inflow is assumed to be isothermal. The luminosity at frequency ν, L_ν, is

$$L_\nu = f\alpha(T) \int_V n(r)^2 \phi(\nu)\, \mathrm{d}^3 r. \tag{5.6}$$

The line profile $\phi(\nu)$ is taken to be the Doppler profile, the density set via mass conservation, $n = n_0 r_0^2 v_0/(r^2 v)$, where $v^2(r) = -2GM(r^{-1} - r_0^{-1}) + v_0^2$. The H$\alpha$ emission efficiency, $f = 0.5$, and temperature, $T = 30,000\,\mathrm{K}$, only affect the total luminosity. The density and velocity are chosen to match the polar accretion rate from the simulations. Taking $r_0 = 2.5 \times 10^{12}\,\mathrm{cm}$ this gives $n_0 = 5 \times 10^{-16}\,\mathrm{g\,cm}^{-3}$ and $v_0 = 80\,\mathrm{km\,s}^{-1}$.

In the spherical case, the emission from a shell can be integrated by hand (see equation 2.62) and the problem reduces to an integral over r. For the conical geometry, the boundary conditions on θ and ϕ are more complex, so the integral is evaluated numerically. Monte-Carlo integration is used due to the high-dimensionality of the problem, with photons being drawn according to the emissivity, $\epsilon = n^2\alpha(T)$. The Monte-Carlo integration agrees with the results from direct integration in the spherical case.

Line profiles for a spherical inflow are shown in Fig. 5.8. The accretion rate is kept the same in each model, whilst the initial density and velocity are varied. In the line wings, where $v \propto r^{-1/2}$, the line profile depends only on $\dot{M}$, T and f.

The presence of an accretion disc in the simulations means that a conical model better represents the geometry of the polar accretion component. The accretion disc fills an angle of roughly 25° and 40° in the models with full and suppressed cooling respectively. The line profiles are shown in Fig.

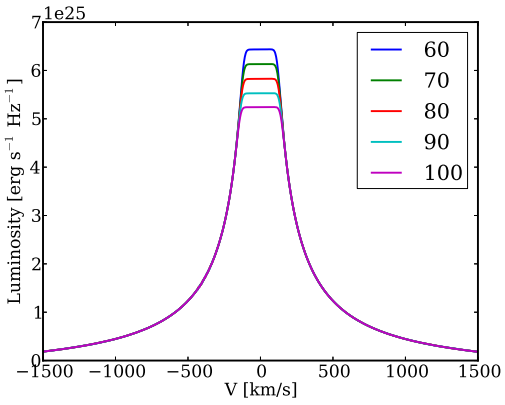

Figure 5.8: Hα line for a spherical inflow model. All models have the same accretion rate, $\dot{M} \approx 2 \times 10^{-8} M_\odot\,\mathrm{yr}^{-1}$. The velocity at the outer edge is varied from -60 to $-100\,\mathrm{km\,s}^{-1}$.

5.9 for conical models with a range of opening angles (defined such that 90 is the spherical accretion case), with the density, n_0, scaled to give each model the same accretion rate. Narrower cones produce higher luminosities as the emissivity is proportional to the square of the density. Conical inflows produce a double peaked profile for observers far enough away from the symmetry axis, roughly corresponding to whether the observer is looking at an angle where the white dwarf would be obscured by the accretion disc. This double peaked profile cannot be the origin of the observed depression in the Hα line, which is an absorption (Bulla, 2013, see also Section 5.1). The expected luminosity of this component is $L_{\mathrm{H}\alpha} \approx 5 \times 10^{-3} L_\odot$, considerably less than the Hα luminosity in RS Oph, which is $0.75 L_\odot$ (Zamanov et al., 2005). Since the luminosity is proportional to the square of the density, the difference would require a polar accretion rate which is roughly 10 times higher than seen in the simulations, or a much narrower opening angle.

Since the models use spherical inflow they assume that angular momentum is negligible in the flow. As shown by Fig. 5.2, this is not the case in the gas close to the white dwarf, at least in the binary plane. Neglecting pressure, the angular momentum of a particle sets a minimum distance from the white dwarf that a particle can reach. The minimum distances for particles that contribute to the density at a distance $r_a = 3 \times 10^{12}\,\mathrm{cm}$ from the white dwarf are shown in Fig. 5.10. While the particles in the polar component tend to have lower angular momentum than particles in the disc, the minimum radii are much larger than the $10^{10}\,\mathrm{cm}$ required to explain the $1500\,\mathrm{km\,s}^{-1}$ Hα line wings. As $10^{10}\,\mathrm{cm}$ is well within the sink radius the flow is not resolved, which means there is

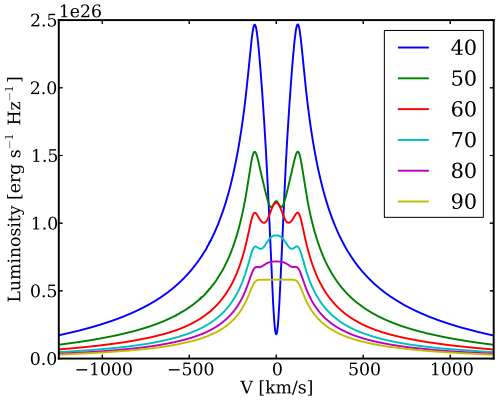

Figure 5.9: Hα line for a conical inflow model. For all models the accretion rate is the same and the observer is at 45° to the symmetry axis. Cones with narrower opening angles produce more luminous profiles as the emissivity, $\epsilon \propto \rho^2$. The key denotes the half-opening angle of the cone, 90° is the spherical model.

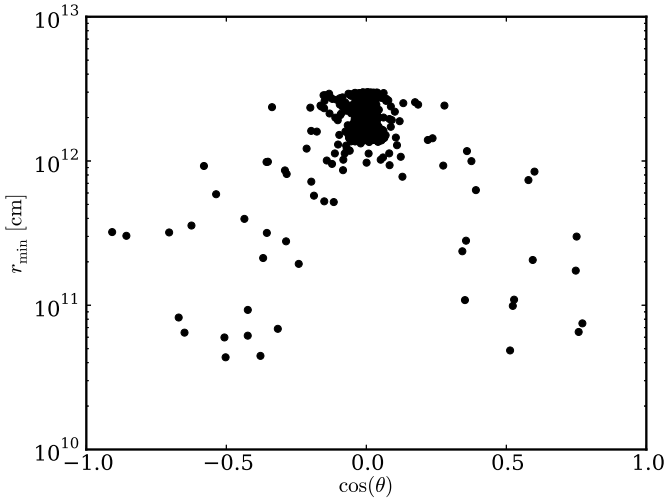

Figure 5.10: Minimum radii of particles being accreted onto the white dwarf as a function of angle. $\theta = 0$ refers to the plane of the binary. The particles shown are those that would contribute to the density at r_a, i.e. $r_i - 2h_i < r_a < r_i + 2h_i$, where r_i and h_i are the distance from the white dwarf and smoothing length of particle i, and $r_a = 3 \times 10^{12}$ cm. The polar accretion component has significantly lower angular momentum than the disc.

considerable uncertainty about the nature of the flow in this region.

Observationally, the hard X-ray emission from RS Oph supports the idea of a polar inflow. The X-ray emission is consistent with a cooling flow model that has an accretion rate of $\dot{M} \approx 3 \times 10^{-9}\,M_\odot\,\mathrm{yr}^{-1}$ and a maximum temperature of $6 \times 10^7\,\mathrm{K}$ (Nelson et al., 2011). The accretion

rate is strikingly similar to the accretion rate in the polar flow. Furthermore, while the maximum temperature of the flow requires an additional strong cooling component to make it consistent with a cooling flow hitting the surface of the white dwarf, it is consistent with the a shock occurring in polar inflow as the gas hits the disc at $v \sim 1600\,\mathrm{km\,s^{-1}}$.

The mass loss rate from the simulations is too low to explain the high absorbing column depth ($N(\mathrm{H}) = 10^{24}\,\mathrm{cm^{-2}}$) that the X-ray emission is subject too; however, the column depth could be produced in the accretion disc. This would require the accretion disc to be considerably thicker than the one in the simulations, at least in the inner parts where the X-rays are emitted.

The strong correlation of the Hα line wings with the motion of the white dwarf means that they must form near the white dwarf, which means they should be subjected to the same column depth as the X-ray emission. As a column depth of $N(\mathrm{H}) = 10^{24}\,\mathrm{cm^{-2}}$ produces an electron scattering optical depth of $\tau_e \approx 0.5$, this is likely to broaden the blue side of the line, but is not enough to thermalize the line. While the bound-bound opacity is likely to be significantly greater, the low radial velocity of the gas in the accretion disc means the bound-bound opacity will contribute the most to the absorbing the centre of the line, not the wings. A strong central absorption in Hα near the white dwarf does not present a problem for the model, because the low velocity emission and central absorption must arise from further out in the binary to explain the lack of a correlation of its velocity with either star (Brandi et al., 2009, see also Section 5.1).

Winds driven from the accretion disc provide a possible alternative explanation for the Hα line profile as the luminosity of the hot component exceeds the effective Eddington luminosity. Simulations of line driven winds in cataclysmic variables naturally produce velocities $v \sim 3000\,\mathrm{km\,s^{-1}}$. However current models predict that the profiles should appear in absorption rather than emission, unless the inclination is high, $i \gtrsim 70°$, (Proga et al., 2002). The difference may not be fundamental, but due to the simplified modelling. Therefore disc-winds remain an attractive origin for the broad emission lines.

5.6 Summary and Discussion

Simulations of the mass transfer in RS Oph have been presented in order to understand how various spectral features arise. Using simplified micro-physics and simulated line profiles allow us to construct a picture of where the spectral features arise in circumstellar medium. The overall picture described in this section is shown in Fig. 5.11

For the mass loss rate used ($10^{-7} M_{\odot}\,\mathrm{yr}^{-1}$) in the simulations of mass transfer, the UV flux from the white dwarf and accretion disc is sufficient to ionize the circumstellar medium. This means that only components that are shielded from the UV emission by the accretion disc remain neutral. In such a picture it may be difficult to construct a consistent model for the Na I D and Ca II H & K line absorption at an inclination of 50°, which is appropriate for RS Oph.

For this reason we prefer a higher mass loss rate for RS Oph of $10^{-6}\,M_{\odot}\,\mathrm{yr}^{-1}$. This would provide sufficient mass that the wind would provide enough optical depth to the UV flux that hydrogen in at $r > 10^{14}\,\mathrm{cm}$ remains neutral. However, the UV flux would be large enough to partially ionize sodium and calcium (Chugai, 2008), which along with the presence of dust in RS Oph, is needed to explain the Ca II H & K absorption. This would give rise to the steady blue-shifted absorption components with velocities up to $20\,\mathrm{km\,s}^{-1}$. Since the flow close to the binary has higher velocity than the terminal wind velocity and is likely to be ionized by the white dwarf, this material may be responsible for the emission components that have been seen (Bulla, 2013).

Currently another explanation is needed for the highest velocity component of the absorption lines ($-40\,\mathrm{km\,s}^{-1}$), which is discussed in the next chapter. The simulations also provide a natural explanation for the red-shifted absorption components seen in the Na I D and Ca II H & K lines, which cannot be explained in a simple model. They arise in the gas that is falling back onto the white dwarf from above the plane, and are strongest when the red giant is furthest from the observer.

This gas forms a polar inflow that may provide an explanation for the large Hα wings that have been observed to correlate with the motion of the white dwarf since a spherical or conical inflow reproduces the line shape. However, the blue-shifted P-Cygni absorption would have to form further away from the white dwarf because it occurs in an outflow, a prospect that agrees with observations both during quiescence and outburst.

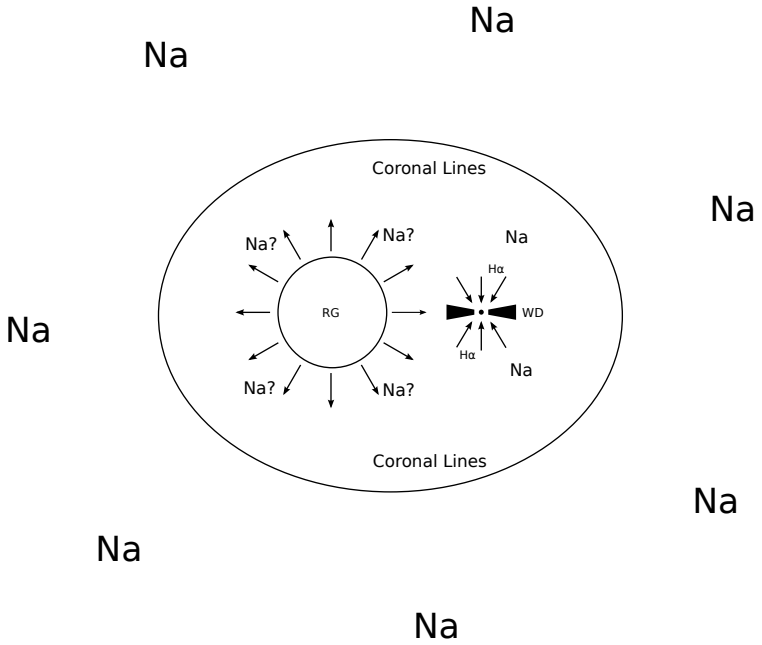

Figure 5.11: Schematic for quiescent line formation in RS Oph. Hα emission occurs close to the white dwarf, in material falling onto the poles of the white dwarf. The P-cygni type absorption is formed in the photo-ionized wind, close to the binary, along with the coronal cF absorption (Brandi et al., 2009). Further out in the wind, the metal lines such as the Na D and Ca H & K lines form. The red-shifted components of these lines form closer in, where material from high above the plane is falling onto the binary. There is also the possibility that some out-flowing components form near the red giant, though these may be degenerate with photospheric components.

The idea that the Hα wings are formed in a polar inflow is supported by the X-ray emission seen in RS Oph, which includes a hard component consistent with a cooling-flow model that has an accretion rate that matches the accretion rate in the polar component. The temperature of the cooling flow is also consistent with gas infalling at $1600\,\mathrm{km\,s^{-1}}$ that has been shocked. The observations require that the hard component is heavily absorbed, of which the only possible source is the accretion disc, which must be thick enough at least in the inner regions to provide the column depth at the preferred inclination of 50°.

The presence of disc-winds, which have been neglected in the simulations may modify the picture significantly. As well as providing a possible explanation for the high-velocity wings seen in the Hα line, the deposition of momentum in the red giant wind may also be able to explain the discrepancy between the velocity produced in the simulations and that observed in RS Oph.

Chapter 6

Novae in RS Ophiuchi and the Circumstellar Medium around SNe Ia

The probable detection of a circumstellar medium in Type Ia supernova (SN Ia) provides a unique probe for the progenitor. The detection and time variation of absorption lines tell us about the density, velocity and distances to gas in the circumstellar medium. The first clear detection of gas in the cirumstellar environment of a SN Ia was SN2006X, which was through the time variation of blue-shifted Na D lines (Patat et al., 2007). Time variation of the Na D lines was also seen in SN 2007le (Simon et al., 2009) and statistical arguments show that there is a 20 per cent excess of SN Ia displaying blue-shifted absorption lines compared with red-shifted or zero velocity absorption lines (Sternberg et al., 2011; Maguire et al., 2013).

The time-dependent behaviours seen in SN2006X and SN2007le require dense clouds of gas within 1 pc from the supernova (Simon et al., 2009). The most likely explanation for these is mass lost from the progenitor star, which is supported by the statistical excess of SNe Ia showing blue-shifted absorption lines, which would not be expected if the absorption is unrelated to the progenitor. Furthermore, the evolution of the line profiles seen in SN2006X shows similarity with that seen in the recurrent nova RS Oph during the 2006 outburst (Patat et al., 2011).

The key features of the time variation in SN2006X that must be reproduced by a successful model are: 1) the absorption line profiles were initially weak, suggesting the circumstellar material

was ionized; 2) after maximum light, the line profiles strengthen on timescales of tens of days, suggesting a recombination timescale of this order; 3) the lowest velocity material recombine first; and 4) the lowest velocity components weaken significantly by 60 days after maximum light, after which the line profiles show no significant further evolution.

Even though there is evidence that most SNe Ia cannot have red-giant companion stars (Bianco et al., 2011; Li et al., 2011; Kelly et al., 2014), further investigation of the connection between RS Oph and SN2006X is of interest. Since recurrent novae also occur in systems with smaller progenitors, e.g. U Scorpii (Thoroughgood et al., 2001), the discussion is relevant to SN Ia in general. In this chapter, models for the interaction between novae and the circumstellar wind in RS Oph are presented. Simulated line profiles during and after the novae are compared to observations and used to constrain the quiescent mass loss. The circumstellar medium is then used to calculate the evolution of sodium absorption expected in SN Ia and the implications for the nova properties required to explain SN2006X are discussed. Finally, a model for the long term interaction of novae with the interstellar medium is discussed as a potential explanation for the 20 per cent excess of blue-shifted absorption lines.

6.1 Nova Models

The simulations presented in this section were set up and run by Shazrene Mohamed, but have been described here in full for completeness. Further details of the code can be found in Mohamed (2010).

RS Ophiuchi has been observed to undergo several outbursts in the last century, with a recurrence period of 10 to 20 years (Rosino & Iijima, 1987). Observations made over a large range of wavelengths during the 2006 outburst can be used to determine the nova properties. Hard X-ray emission was observed to deviate from that expected from a shocked shell, indicating a low mass ejected, $M \sim 10^{-7}\,M_{\odot}$, and a high density in the surrounding medium, $n \sim 10^{9}\,\mathrm{cm}^{-3}$ (Sokoloski et al., 2006). The velocity of the ejecta can be found using broad emission lines, which show $v \sim 4000\,\mathrm{km\,s}^{-1}$ for the first four days, decreasing rapidly thereafter (Anupama, 2008; Das et al., 2006). This agrees with the shock being slowed as it sweeps up the gas in the circumstellar medium. Resolved images of the 2006 nova taken in the optical with the Hubble Space Telescope (Bode et al.,

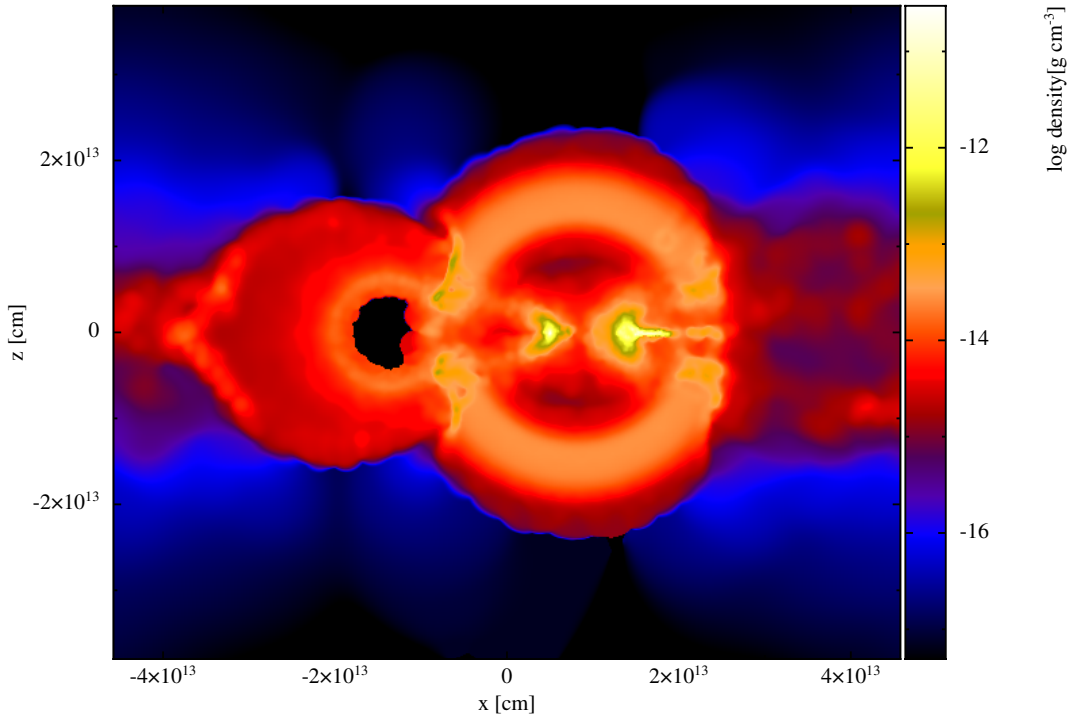

Figure 6.1: Interaction of the nova with the accretion disc and red-giant wind, one day after the shell was ejected. The cross section is through the red giant and white dwarf, as in Fig. 5.2. The accretion disc survives the initial passage of the nova but a large proportion of the gas contained in it rapidly evaporates after it has been shock heated by the nova.

2007) and using VLBI in the radio (O'Brien et al., 2008; Rupen et al., 2008; Sokoloski et al., 2008) show that the nova was bipolar.

The novae are modelled using the Smoothed Particle Hydrodynamics models for the circumstellar medium formed by quiescent mass transfer in RS Oph presented in Chapter 5. After the quiescent mass transfer has evolved for 18 years, the interaction between multiple novae and the circumstellar medium is calculated. The novae are modelled using a spherical shell for the ejecta, which is ejected instantaneously by inserting the shell within the sink region around the white dwarf. The nova mass is taken to be $2 \times 10^{-7} M_{\odot}$, and the velocity is set to give a terminal velocity $v \approx 3500\,\mathrm{km\,s^{-1}}$. The internal energy is initially set to 25 per cent of the kinetic energy, meaning the dynamics are dominated by the ram pressure.

While it appears that mass loss during the novae may continue for some time, even optically thick wind models predict the strongest mass loss at the start of the outburst (Kato & Hachisu,

1994). Time-dependent models for novae on a $1.25\,M_{\odot}$ show that the mass loss rate drops on a timescale of a few hours (Prialnik & Kovetz, 1992). For a Chandrasekhar mass white dwarf, the timescale is expected to be even shorter (e.g. Yaron et al., 2005). Therefore, we expect that a shell is a good model for the interaction of the novae with the circumstellar medium.

The instantaneous ejection of the majority to the mass in recurrent novae is supported by observations of several systems, including U Scorpii and T Pyxidis, which show flat-topped line profiles during outburst (Mason et al., 2012; Shore et al., 2013). Flat-topped profiles are generally indicative of emission confined to a shell. In RS Oph, the early line profiles are triangular, rather than flat topped (Iijima, 2009; Patat et al., 2011). This may be indicative of an extended period of mass loss; however, it may also be due to the circumstellar interaction. Emission lines during the 2006 outburst show the ejecta maintain a high velocity ($v \approx 4000\,\mathrm{km\,s^{-1}}$) during the first few days, after which the velocity drops rapidly (Anupama, 2008). This suggests that if the mass loss from the white dwarf is extended then the duration of the phase must be less than 4 days, or at least the velocity of the mass loss decreases rapidly beyond 4 days.

The red giant has been neglected in the simulation. However, as can be seen in Fig. 6.1, the accretion disc shields the red giant from the nova substantially, so any error introduced should be small. For the purpose of understanding the circumstellar medium, the difference is not too important because the red giant only affects the novae within a small solid angle. The accretion disc initially survives the passage of the nova, immediately cutting the ejecta into two polar lobes.

Within 10 days, the nova has escaped the wind in the polar direction and expands freely, cooling adiabatically. However, the shock takes several years to sweep up the wind in the plane of the disc, decelerating rapidly due to the high mass in the plane. The final structure of the nova ejecta are shown in Fig. 6.2. The nova remains strongly bipolar, with the ejecta in the polar directions remaining close to the ejection velocity. Even though the nova sweeps up the majority of material in the plane, there is considerable material in the centre of the system, which comes from the material that has evaporated from the accretion disc. The swept up wind forms a 'waist' in the plane of the binary, which decelerates to $v \approx 50\,\mathrm{km\,s^{-1}}$. A large fraction of the waist is made up of shocked wind material rather than shocked nova material. The shocked nova material can be seen drawn

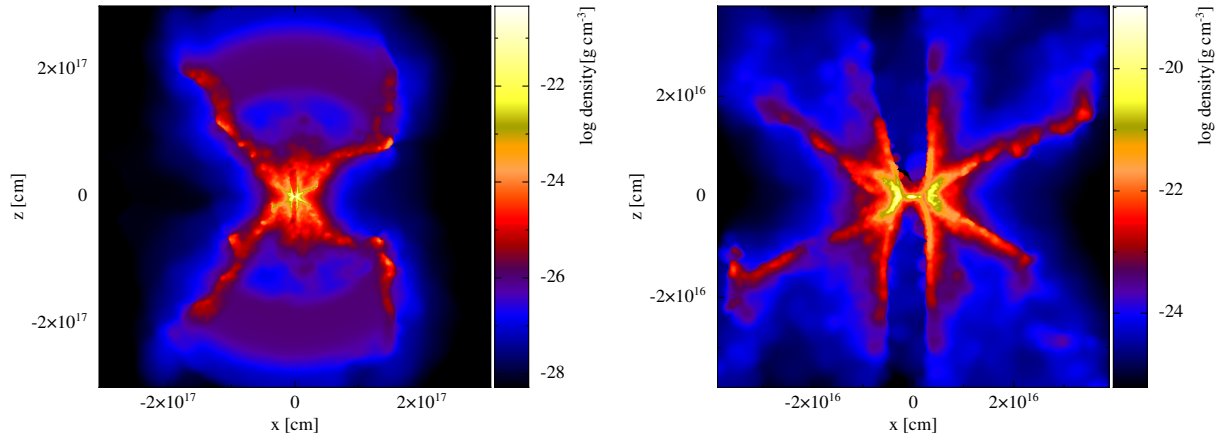

Figure 6.2: Final structure of the first nova, 18 years after the explosion. No contribution from the second phase of mass transfer has been included. At the time of explosion the red giant was on the negative x-axis. *Left*: Full structure. *Right*: Zoom in on central region. The structure of the central region is complex, and contains a high density waist that forms as the nova ejecta run into the dense wind in the plane of binary. Interior to the waist a second high density region arises out the of gas which was ablated off the accretion disc, which forms the central polar features. The low density region along the poles is likely to be an artefact of the hole in the accretion disc.

out along the edge of the of the waist. In the polar directions, the shock accelerates due to the rapidly decreasing density, producing velocities of $v \approx 4000\,\mathrm{km\,s^{-1}}$.

The peak density in the waist material after a recurrence period is $\rho \approx 3\times10^{-20}\,\mathrm{g\,cm^{-3}}$. This can be compared with the thin-shell models by Moore & Bildsten (2012), who found a post-shock density of $n \approx 10^{9}\,\mathrm{cm^{-3}}$ once the novae had swept up the entire wind (1.1 yr). Their models used a higher mass-loss rate $\dot{M} = 10^{-6} M_{\odot}\,\mathrm{yr}$ but the same nova mass to wind mass ratio. The concentration of the wind in the binary plane enhances the mass-loss rate in the plane to $\dot{M} \approx 4 \times 10^{-7} M_{\odot}\,\mathrm{yr}$. Reducing the density reached by the Moore & Bildsten (2012) model accordingly and extrapolating to 18 yr using $\rho \propto t^{-2}$ gives a density $\rho \approx 2.5 \times 10^{-18}\,\mathrm{g\,cm^{-2}}$, roughly 50 times higher than that produced in the simulations.

The difference between the thin-shell estimate and the simulations can be partially reconciled if $\rho \propto t^{-3}$, giving $\rho \approx 1.5 \times 10^{-19}\,\mathrm{g\,cm^{-3}}$, approximately five times higher than that seen in the simulations. If the density evolves as $\rho \propto t^{-3}$, it suggests that the relative thickness of the shell, $\Delta r/r$, is constant and $v \propto r$ in the shell, which is the case in the simulations.

Taking into account that the asymmetry increases the wind mass in in the plane but not the

nova mass, results in a lower shock velocity. As the cooling is approximately isobaric, Moore & Bildsten (2012) give

$$\frac{\rho_s}{\rho_0} \approx \left(\frac{v_s}{v_{\rm th}}\right)^2, \tag{6.1}$$

where ρ_0 is the wind density, v_s is the shock velocity, $v_{\rm th}$ is the thermal velocity once the post-shock gas has cooled and ρ_s is density in the shell once the gas has cooled. Only a moderately lower shock velocity is needed to account for the difference.

Whether structure of the nova shell can be trusted in the presence of cooling is debatable, as the broadening of the shock means that cooling occurs while the gas is still being heated by the shock. While the final post-shock temperature can be expected to be approximately correct, numerical tests showed that the shock structure is not, resulting in a too high shock velocity (Creasey et al., 2011).

Physically, the thickness of the shell is controlled by the sound crossing time, which for a shell thickness of 10^{15} cm at 18 yr and a temperature of 10^4 K, gives $t_x = \Delta r/c_s \approx 30$ yr, where c_s is the sound speed, is close to recurrence time, t_r for the system. While the temperature is currently lower than 10^4 K, if $v \propto r$ then the ratio t/t_x is approximately constant. Therefore, the thickness is likely to reflect the temperature of the gas at the time when the shell was broadened through pressure. As the gas can rapidly cool to 10^4 K, this is likely to be the temperature that controls the evolution.

As over-cooling reduces the temperature and sound speed in the gas this would suggest that the numerical shells should be less broadened than the real ones; however, this seems to disagree with the numerical experiments of Creasey et al. (2011) and the difference is likely to arise due to a lower post-shock density in the over-cooled models. Unfortunately, this means there is a fundamental uncertainty in the evolution of the density within the nova shells. However, quantities depending on the column density are not significantly affected as the increased thickness cancels out the reduced density.

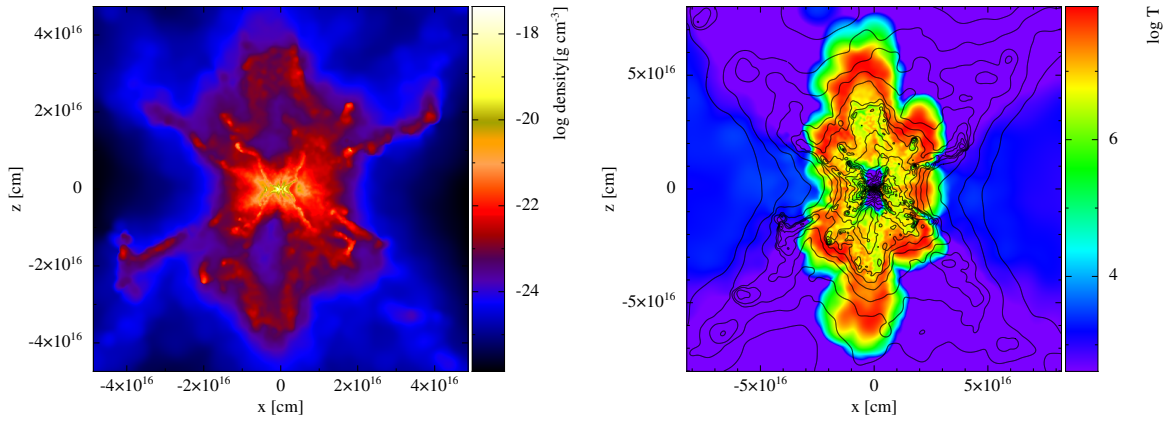

Figure 6.3: The structure 1000 days after the second nova. Note the differing spatial scales. *Left*: Density in cross-section. *Right*: Temperature. The interaction between the polar shells and previous nova shocks the shell, which forms a clumpy structure as it cools. While the shell will never catch up with the previous nova in the polar directions, the shock runs into the waist of the previous nova. The hottest temperatures arise in the forward shock of the second nova, reaching 10^8 K. The reverse shocked ejecta from the second nova is cooler, reaching 5×10^6 K.

6.1.1 The Second Nova

It is clear that subsequent novae encounter a different environment to the first nova, which expands in vacuo. For this reason, a second nova has been calculated. Rather than explicitly calculating the mass-transfer prior to the second nova, the circumstellar medium prior to the second nova is produced by adding the quiescent wind, simulated in the absence of novae (Fig. 5.2), to the structure resulting from the first nova (Fig. 6.2). Since the wind is at much higher density and lower velocity than the remaining nova material any errors introduced by the procedure are small, which was verified for a single test case. The second nova shell is then included using the same model as the first one.

The structure formed by the second nova is considerably more clumped (Fig. 6.3). The greater mass in the polar direction shocks the ejecta and the cooling drives clump formation. The second nova shell is at lower velocity than the first ($\sim 2500\,\mathrm{km\,s^{-1}}$) and will never catch up the first shell. The reverse is true in the plane of the binary because the nova has a higher velocity than the waist and the waist is starting to become overrun by the first shell.

The shock driven through the waist of the first nova shell strips the material that is flowing out at inclinations of $i \gtrsim 30°$ and compresses the rest of the shell, which can be seen in Fig. 6.4. The

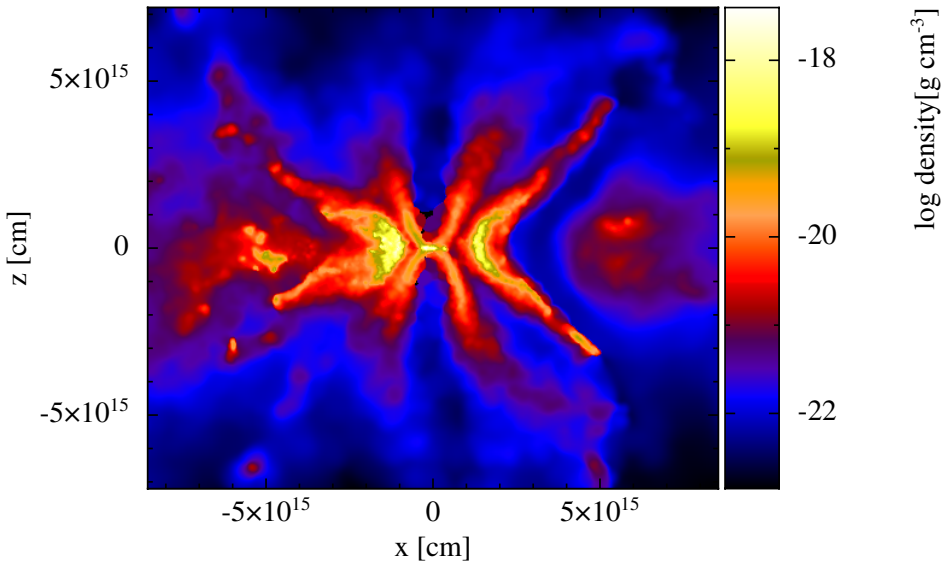

Figure 6.4: Density cross section showing the waist of the novae 2000 days after the second nova. The waist of the first nova has been partially stripped and compressed by shocks from the second nova. The waist is shocked to 10^6 K and begins to cool. Since the cooling timescale in the diffuse parts of the shocked waist is approximately equal to the recurrence period, the remaining gas will cool and survive.

compressed gas reaches 10^6 K before beginning to cool. Since the cooling timescale in the diffuse parts of the remaining gas is approximately equal to the recurrence timescale the gas will cool before the third nova. The long-term fate of the shocked waist will depend on whether it it is shocked again by subsequent novae, because only the dense clumps are likely to be able to cool.

6.1.2 Photoionization of the nova shells

Photoionization of the nova shell can be considered using the same models that are used during quiescence. The nova shells are not sufficiently massive to provide significant optical depth to the ionizing photons, which means that once the nova reaches quiescence the ionization structure is controlled by the material close to the white dwarf which gives rise to the same conical structure as seen in Fig. 5.4. The main difference arises because part of the nova shell does not cool within the recurrence period, remaining collisionally ionized, which can be seen near the plane of the binary in Fig. 6.5. The majority of the mass in the region that is not photoionized remains neutral.

Therefore, in the polar directions the nova shells will be ionized, while close to the binary plane

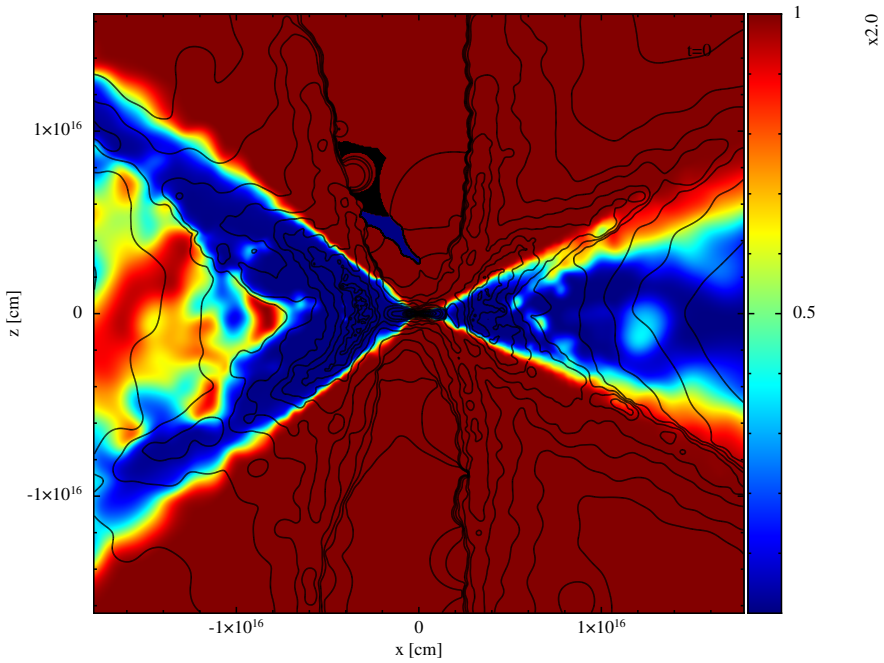

Figure 6.5: Hydrogen ionization fraction of the inner parts of the nova shell, using a luminosity of $L = 100\,L_{\odot}$ and black-body temperature of $T = 4e4\,\mathrm{K}$. The ionization structure is controlled by the inner parts of the binary and follows the same pattern as the pure wind. The exceptions are the diffuse parts of the nova ejecta, where the ejecta have not cooled sufficiently to recombine. The apparently neutral material in the polar direction is an artefact, arising because the density in the simulations is zero in that region.

the shells will be neutral. Since the ionization structure in the nova shells reflects the ionization structure in the wind, the presence of absorption components seen in the nova shells should be linked with the presence of components seen in the wind. Therefore, for illustrative purposes calculations of the line profiles neglecting photoionization from the binary are sufficient.

6.2 Nova contribution to absorption lines

The absorption line profiles for sodium are calculated using the same technique as in Chapter 5. Since RS Oph is a bright source of super-soft X-rays between 30 and 100 days after the outburst (Osborne et al., 2011), the nova shells are assumed to be fully ionized during this time. Once the X-ray luminosity drops then the nova is allowed to recombine. During the recombination phase photoionization is neglected and the density is taken to evolve as $\rho \propto t^{-3}$. However, as discussed earlier, for thin shells expanding at a constant velocity a higher density and $\rho \propto t^{-2}$ is expected.

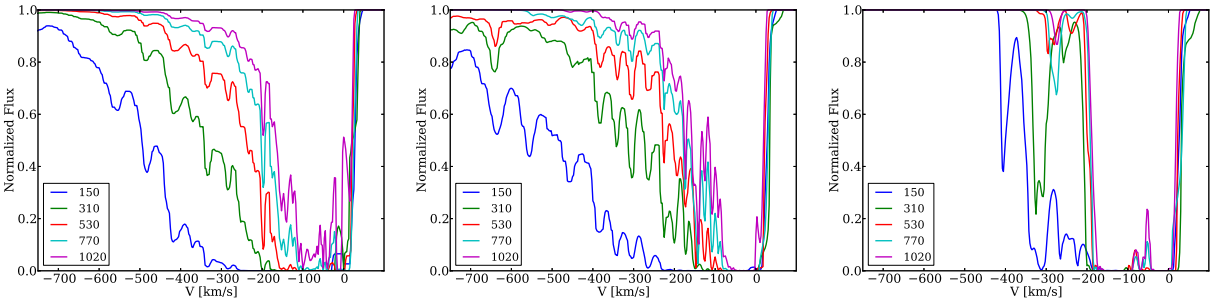

Figure 6.6: Evolution of the nova contribution to the sodium line profiles for inclinations of 30° (left), 45° (middle) and 60° (right). The key denotes days since the start of the outburst. The saturated components at $v = 0$ arise in gas stripped from the accretion disc that remains close to the plane of the binary (Fig. 6.2).

Due to the large range of recombination timescales in the simulations, the main effect is to change the amount of gas that is able to recombine.

The evolution of the ionization fractions is given by

$$\frac{\mathrm{d}X_{\mathrm{H}}}{\mathrm{d}t} = -\alpha_{\mathrm{H}} n_0 \left(\frac{t}{t_0}\right)^{-3} X_{\mathrm{H}}^2, \tag{6.2}$$

$$\frac{\mathrm{d}X_{\mathrm{Na}}}{\mathrm{d}t} = -\alpha_{\mathrm{Na}} n_0 \left(\frac{t}{t_0}\right)^{-3} X_{\mathrm{H}} X_{\mathrm{Na}}. \tag{6.3}$$

Combining the above we find

$$\frac{1}{X_{\mathrm{Na}}}\frac{\mathrm{d}X_{\mathrm{Na}}}{\mathrm{d}t} = \frac{\alpha_{\mathrm{Na}}}{\alpha_{\mathrm{H}}} \cdot \frac{1}{X_{\mathrm{H}}}\frac{\mathrm{d}X_{\mathrm{H}}}{\mathrm{d}t}, \tag{6.4}$$

where α_{Na} and $\alpha_{\mathrm{H,B}}$ are the recombination rates of sodium and hydrogen (case B) and n_0 is the number density of hydrogen at t_0, which is the time recombination begins. The solutions to the above equations are

$$X_{\mathrm{H}}(t) = \left[1 + \tfrac{1}{2}\alpha_{\mathrm{H,B}} n_0 t_0 \left(1 - \left(\frac{t_0}{t}\right)^2\right)\right]^{-1}, \tag{6.5}$$

$$X_{\mathrm{Na}}(t) = X_{\mathrm{H}}^{\frac{\alpha_{\mathrm{Na}}}{\alpha_{\mathrm{H,B}}}}. \tag{6.6}$$

The electron fraction is assumed to be entirely due to hydrogen, which is a reasonable approximation since $\frac{\alpha_{\mathrm{Na}}}{\alpha_{\mathrm{H,B}}} > 5$, therefore sodium recombines more rapidly than hydrogen (Verner et al., 1996). The

temperature evolution has not been included, but the recombination coefficients are not sensitive to temperature. The ionization fractions are not allowed to drop below their LTE values at the appropriate temperature, and the time at which the photoionization is assumed to be negligible is taken to be 100 days. The effect of the approximation $n \propto t^{-3}$ has been tested by comparing the evolution to models where the current density is used. The constant density model produces profiles which are weaker by approximately 10 per cent at velocities of a few $100\,\mathrm{km\,s^{-1}}$, but otherwise the profiles are the same.

The photosphere of the nova shrinks to near the surface of the white dwarf within 20 days (Kato & Hachisu, 1994). The size of the typical structures in the novae are much larger than the binary, therefore the results are not sensitive to whether the photosphere is dominated by the red giant or white dwarf. Accretion may have restarted by 240 days after the nova (Worters et al., 2007), suggesting that the system is in quiescence by this time. Since this follows a period in the post-outburst light curve of lower luminosity, it is reasonable to assume that the white dwarf no longer contributes to the luminosity at the wavelength of the Na D line (Darnley et al., 2008) and the photosphere can be taken to be that of the red giant.

The line profile evolution during the first 1000 days after the second nova is shown in Fig. 6.6. The majority of the nova shell recombines quickly, and the subsequent evolution is dominated by the decreasing column density. For inclinations $i \lesssim 70°$, the deceleration of the shell is small. For higher inclinations, the temperature in the shell remains too high for sodium to recombine during the first 1000 days, therefore the only component that arises is due to the gas stripped from the accretion disc that remains at low velocities and close to the binary plane (see Fig. 6.2).

At high inclinations the shell recombines slowly over several years because the gas is kept hot through it's interaction with the wind. After 18 years, approximately a recurrence time, the nova shell has mostly become neutral, having swept up the entire mass loss the from prior period of quiescence. The line profile at that time is shown in Fig. 6.7, for a variety of inclinations. For inclinations $i \lesssim 40°$, the shell can barely be seen at all because it encountered very little mass and expanded freely until the column depth becomes negligible. For higher inclinations, the ejecta and swept up wind can be seen more strongly and at lower velocities. For $i > 75°$ the shell velocity has

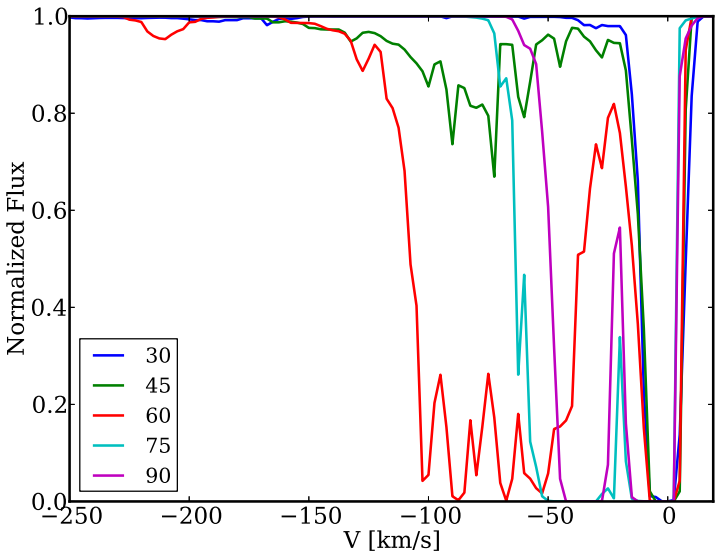

Figure 6.7: Na D line profile for the nova just before the second outburst (7020 days). The key denotes the inclination. At low inclinations the nova shell has become too diffuse and cannot be seen, while at increasing inclinations the velocity of the shell decreases and the line profile strength increases.

dropped to $50\,\mathrm{km\,s^{-1}}$.

The models predict higher velocities for components formed in the nova shell have been seen in RS Oph, with strong absorption up to approximately $250\,\mathrm{km\,s^{-1}}$ and a high velocity tail. However, this discrepancy may be evidence that the mass-loss rate in RS Oph is higher, as suggested from ionization arguments in Chapter 5. Furthermore, a higher mass-loss rate would also help to explain why the quiescent UV flux does not ionize the shell.

The expansion and deceleration of the nova shell suggests a way to test the association of circumstellar absorption features with nova shells. Absorption lines formed in the nova shell must have higher velocities than the typical wind velocities. In cases where high velocity components are seen, a systematic slowing of weakening of the component and no dependence on binary phase would be strong evidence that these lines form in the nova shell.

This behaviour may have already been seen in the 2006 outburst of RS Oph. Prior to the 2006 outburst of RS Oph, the maximum velocity of the absorption components was $v \approx -50\,\mathrm{km\,s^{-1}}$. At 750 days after the outburst the maximum velocity was larger, $v \approx -75\,\mathrm{km\,s^{-1}}$, and the absorption lines were stronger. Under the assumption that the 2006 nova was broadly similar to the 1985 nova,

then this higher velocity component may be from the nova shell. Should subsequent observations show the components decrease in velocity and weaken, it would be clear that this is the case.

6.3 The circumstellar medium for SNe Ia

The circumstellar medium produced by the interaction between the novae and the mass loss during quiescence can be used to calculate the line profile seen when a Type Ia supernova occurs. Since the exact time of detonation in single degenerate progenitors for Type Ia supernovae is controlled by the convective Urca process, which lasts for $\sim 1000\,\mathrm{yr}$ (Paczyński, 1972; Iben, 1982), the time of explosion is likely to be uncorrelated with the nova outbursts. For illustrative purposes the supernova is taken to occur instead of the second nova, once the nova shell has reached it's maximum distance.

The supernova is taken to be an expanding sphere with $v_{\mathrm{SN}} = 20,000\,\mathrm{km\,s^{-1}}$, which sweeps the circumstellar medium. Effectively this is done by removing gas within $r = v_{\mathrm{SN}}t$, so that it doesn't contribute to the line of sight. For the photospheric radius, a simple approximation due to Chevalier (1981) is used

$$R_{\mathrm{p}} = \begin{cases} 2.61 \times 10^{14} t_{\mathrm{d}}^{2/3}\,\mathrm{cm} & t_{\mathrm{d}} < 40.7, \\ 8.86 \times 10^{13} \left[1 - \left(\frac{t_{\mathrm{d}}}{108}\right)^2\right] t_{\mathrm{d}}\,\mathrm{cm} & t_{\mathrm{d}} > 40.7, \end{cases} \tag{6.7}$$

where t_d is the time in days. This expression overestimates the photospheric velocity $v_{\mathrm{p}} = R_{\mathrm{p}}/t$ by approximately 25 per cent when compared with photospheric velocities from abundance tomography calculations (Stehle et al., 2005; Mazzali et al., 2008). The supernova photosphere begins to recede after approximately 60 days. Once the photosphere has receded, a surface brightness model should be used for the supernova. However, by this time the supernova has swept up the majority of the mass in the circumstellar medium and the absorption lines have disappeared.

Both the novae and the wind are included in the models for the circumstellar medium, although the majority of the wind is swept up by the supernova in the first few days. Two models for the ionization state are considered, one where the gas ionization is purely thermal, and a second, following Patat et al. (2007), where the UV flux from the supernova keeps the circumstellar medium

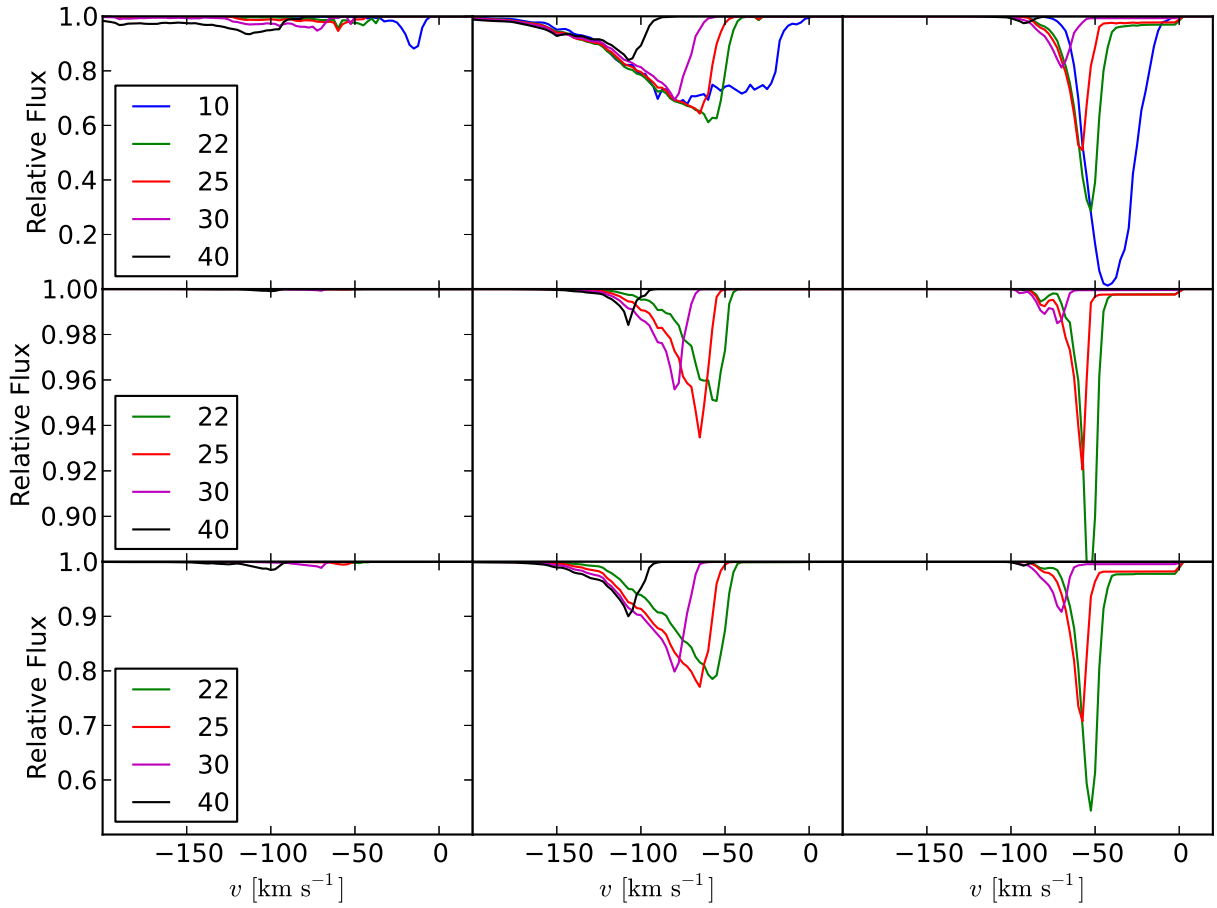

Figure 6.8: Sodium D line profiles against a photosphere expanding with $v = 20,000\,\mathrm{km\,s^{-1}}$. The key denotes time since explosion. *Top*: Thermally ionized model. *Middle*: Recombining model, assuming ionization until 20 days. *Bottom*: Recombining model, using a filling factor, $f = 3 \times 10^{-2}$. The inclination of the observer increases from left to right with $i = 0°$, 45° and 90°. Besides recombination affecting the bottom profiles, two effects contribute to the evolution. The supernova overtakes the lowest velocity ejecta first, causing the profiles to weaken at lower velocities. As the photosphere grows, the covering factor of the components also decreases, reducing the strength at all velocities.

ionized for the first 20 days, after which it is recombines. The recombining model has also been calculated using a filling factor $f = 3 \times 10^{-2}$.

The filling factor takes into account unresolved clumping and is often required by photoionization models to reproduce spectra. While the filling factor has not been measured for RS Oph, it was found to be $f \approx 3 \times 10^{-2}$ for the recurrent nova T Pyx (Shore et al., 2013). A filling factor that is less than unity increases the effective density, but decreases the effective volume, which means that

forming process that are linear in density are unaffected. Recombination depends on the square of the mass, so the filling factor has the effect of decreasing the recombination timescale, t_r, because $\frac{\sqrt{\langle\rho^2\rangle}}{\langle\rho\rangle} = f^{-1}$, implying $t_r \propto f^{-1}$.

The line profile evolution for the different models are shown in Fig. 6.8. Despite the large velocity of the shell in the polar directions, the absorption components produced for velocities greater than a few $100\,\mathrm{km\,s^{-1}}$ are weak. For all inclinations, there are components at $v \sim 50\,\mathrm{km\,s^{-1}}$, which are produced in the ablated accretion disc material and also in the waist for high inclinations. However, as the distances to the waist are only 3×10^{15} cm, the supernova reaches this material after roughly 20 days and the line begins to weaken. The lines weaken later for inclinations of 45° because the waist material is at higher velocities and larger distances for this inclination, resulting in the lines disappearing over 50 days instead of 30.

The recombination timescale with $f = 1$ is approximately 100 days for the $v \sim 50\,\mathrm{km\,s^{-1}}$ component produced in the waist, with longer recombination times-scale for material in the polar directions. The optical depth produced is approximately ten times smaller than the thermal model, but otherwise the evolution is similar. The density of the gas at higher velocity is lower, which gives rise to a distinctive recombination wave from lower to higher velocity. Since the recombination timescale in the model with $f \approx 3 \times 10^{-2}$ is as low as a few days, much more material recombines producing stronger absorption. If the nova shell is more accurately described by a thin shell, density would be 50 times higher (see above). This would produce a similar recombination timescale for the $f = 1$ model as found in the simulations find for the $f = 3 \times 10^{-2}$ model.

A similar recombination wave was seen in SN2006X (Patat et al., 2007). The novae also naturally reproduce the velocity of the absorption components seen in SN2006X and that the lower velocity components are stronger and recombine faster. Furthermore, in the $f = 3 \times 10^{-2}$ model the recombination timescale is short enough to reproduce the recombination wave seen in SN2006X. The main discrepancy in the simulated line profiles is that by 20 to 50 days after explosion the lines have disappeared. While the lowest velocity components in SN2006X disappear on this timescale, other components are still present 150 days after the explosion. Currently there have been no detections of circumstellar material in normal SN Ia which have been observed to disappear, which

suggests a larger distance to the ejecta, $r \gtrsim 5 \times 10^{16}$ cm. An exception this is the supernova PTF 11kx (Dilday et al., 2012), although this was not a normal SN Ia.

The increased distance to the nova shell can be simply explained by a recurrence time of several hundred years. This would require a much lower accretion rate $\dot{M} \sim 10^{-9}\,M_{\odot}\,\mathrm{yr}^{-1}$ (Yaron et al., 2005). Yaron et al. (2005) find that models with accretion rates as low as $\sim 10^{-9}\,M_{\odot}\,\mathrm{yr}^{-1}$ predict that the white dwarf should decrease in mass; however, so far the effects of rotation, convection and composition of the white dwarf mean there remains some uncertainty in this.

If the distance to the shell is 10 times greater then the distance in the simulations, then for the same mass the density would be a factor of 10^3 lower. However, the longer phase of mass loss before the novae would increase the mass in the shell, such that the density would be a factor of 100 lower and the column density a factor of 10 lower, producing lines that are considerably weaker than those seen in supernovae. The low density would also require considerably lower filling factors $f \lesssim 10^{-3}$ to explain the recombination timescale, and the increased mass would mean the velocity of the shell would be lower.

If, as noted in earlier, the shell should actually evolve as $\rho \propto t^{-2}$, as in the thin shell models, then the density would be much higher. Using the estimate based on Moore & Bildsten (2012), then once the shells reach a few 10^{16} cm this would give a density 500 times higher than that found in the simulation, potentially reproducing the recombination timescale without the need for a filling factor. The velocity and column density would be the similar to those for the $\rho \propto t^{-3}$ case, as expected from the simulation.

Alternatively, the dense waist of the nova shells will reach several 10^{16} cm after roughly 10 novae, therefore it may be possible that the line profiles form in multiple nova shells rather than in a single shell. The total mass would be similar to a model with a longer recurrence time, however the mass would be spread out over a larger range of radii. As a consequence, once the supernova starts to overrun the shells contributing to the Na D line profile, the optical depth should reduce smoothly, whereas in a single shell model the process should happen on a much shorter timescale.

As suggested by Chugai (2008), the biggest problem in explaining the Na D line absorption using a nova shell model comes from the ionization by γ-ray deposition, which is the dominant

contribution to the ionization of hydrogen after maximum light. Comparing the ionization rate by γ-ray deposition to recombination gives a critical density, $n_{\rm H} = \frac{\Gamma_{\rm Na}}{\alpha_{\rm Na}}$, above which sodium should be neutral. Using the ionization rate from Kozma & Fransson (1992) and assuming $M_{\rm Ni} = 0.6 M_{\odot}$ gives critical density $n_{\rm H} \approx 2 \times 10^{6}\,{\rm cm}^{-3}$ at $r = 5 \times 10^{16}\,{\rm cm}$.

If the waist evolved entirely in free expansion until it reached $5 \times 10^{16}\,{\rm cm}$, the density would be $n \sim 1\,{\rm cm}^{-3}$. If the mass loss from the red giant is $10^{-6}\,M_{\odot}\,{\rm yr}^{-1}$, as the observations during quiescence and the 2006 outburst suggest, then this would partially help, but filling factor of $f \sim 10^{-4}$ would be required to achieve the density needed. High enough density ratios have been found in simulations of interacting supernova driven super-bubbles (Ntormousi et al., 2011), although it is not clear that sufficient mass is locked up in this ultra-high density phase. Alternatively, if the thin shell models are correct and the density is 500 times higher, a filling factor of $f \approx 0.03$, as observed in T Pyx, would be sufficient to produce the required density.

The interaction of different nova shells is also important for determining the conditions in outer nova shells. The waist is shocked by the second nova, which compresses and heats the gas but strips some of the more diffuse parts. This process may actually help produce high enough densities, since the cooling timescale is short enough that the compressed material cools and clumps. Currently it is not clear how many times the waist would undergo this process, but if the clumps survive it would help increase the density. The process would also impart momentum into the clumps which would help maintain the correlation between distance to and velocity of the absorption lines, which would not be expected for a series of non-interacting shells. However, the stripping may mean that insufficient mass is left in the shell to produce sufficiently strong absorption lines and the column densities are already marginal.

6.4 An Alternative Model

It remains unclear whether the nova shells themselves can be responsible for the circumstellar absorption lines in Type Ia supernovae. The observed 20 per cent excess in blue-shifted lines (Sternberg et al., 2011; Maguire et al., 2013) is strong evidence for a pre-supernova outflow. Furthermore, there has been no detection of circumstellar absorption candidates in elliptical galaxies. While such sta-

tistical arguments say little about an individual supernova, they can provide insights based upon a sample supernovae.

These two arguments appear to be discrepant with each other. (Maguire et al., 2013) suggest that this may be due to different progenitor channels producing the supernovae in the different galaxy types, since the supernovae in ellipticals come from older stellar populations. Alternatively, the explanation may be that the local interstellar medium has a role to play in formation of the lines. As the interstellar medium is diffuse in elliptical galaxies, its effect on the mass-loss is likely to be negligible. However, a shell will form as the wind or novae sweeps up the more dense interstellar medium found in spiral galaxies.

In this section long term effects of the recurrent novae on the circumstellar medium are considered using a simple model. Although a one-dimensional model greatly over simplifies the dynamics, it can capture the main features of the evolution. For this purpose, the novae are modelled as a one-dimensional wind, with mass loss equal to the total mass loss rate from the symbiotic, $\dot{M} = 10^{-7} M_{\odot}\,\mathrm{yr}^{-1}$. The velocity is set by momentum conservation as the novae sweep up the red-giant wind. Therefore, $v = 350\,\mathrm{km\,s}^{-1}$ since the nova mass is 10 per cent of the wind mass. The interstellar medium is taken to be a uniform gas with $n_{\mathrm{H}} = 1\,\mathrm{cm}^{-3}$ and $T = 200\,\mathrm{K}$. Atomic cooling for $T > 10^4\,\mathrm{K}$ has been included using the cooling curves from Sutherland & Dopita (1993).

The recurrent nova phase is taken to be the lifetime of the symbiotic phase, which is roughly $10^5\,\mathrm{yr}$. The evolution of the shell is shown in Fig. 6.9. As the shock sweeps up the interstellar material, the shock slows from $350\,\mathrm{km\,s}^{-1}$ to $15\,\mathrm{km\,s}^{-1}$ by $10^5\,\mathrm{yr}$. The density in the swept up interstellar medium is sufficient to cool it to $10^4\,\mathrm{K}$, but the novae remain hot. Since atomic cooling becomes inefficient at $10^4\,\mathrm{K}$ the inclusion of molecular cooling is required to understand whether the gas can cool further. Rayleigh-Taylor instabilities at the contact discontinuity will induce density perturbations and further enhance the cooling.

Assuming the thickness of the nova shells $\delta r/r = 0.1$ and comparing the sound crossing time in the shocked nova shells, $t_s = \frac{\delta r}{c_s} \approx \frac{10^{17}\,\mathrm{cm}}{100\,\mathrm{km\,s}^{-1}} \approx 3 \times 10^4\,\mathrm{yr}$, to the recurrence time, $t_r \approx 20\,\mathrm{yr}$, suggests that approximating the novae as a smooth wind will underestimate the density in the shocked novae. Since the cooling timescale at $10^6\,\mathrm{K}$, $t_{\mathrm{cool}} \approx 5 \times 10^4 (\frac{\mathrm{cm}^{-3}}{n_{\mathrm{H}}})\,\mathrm{yr}$, the novae will not

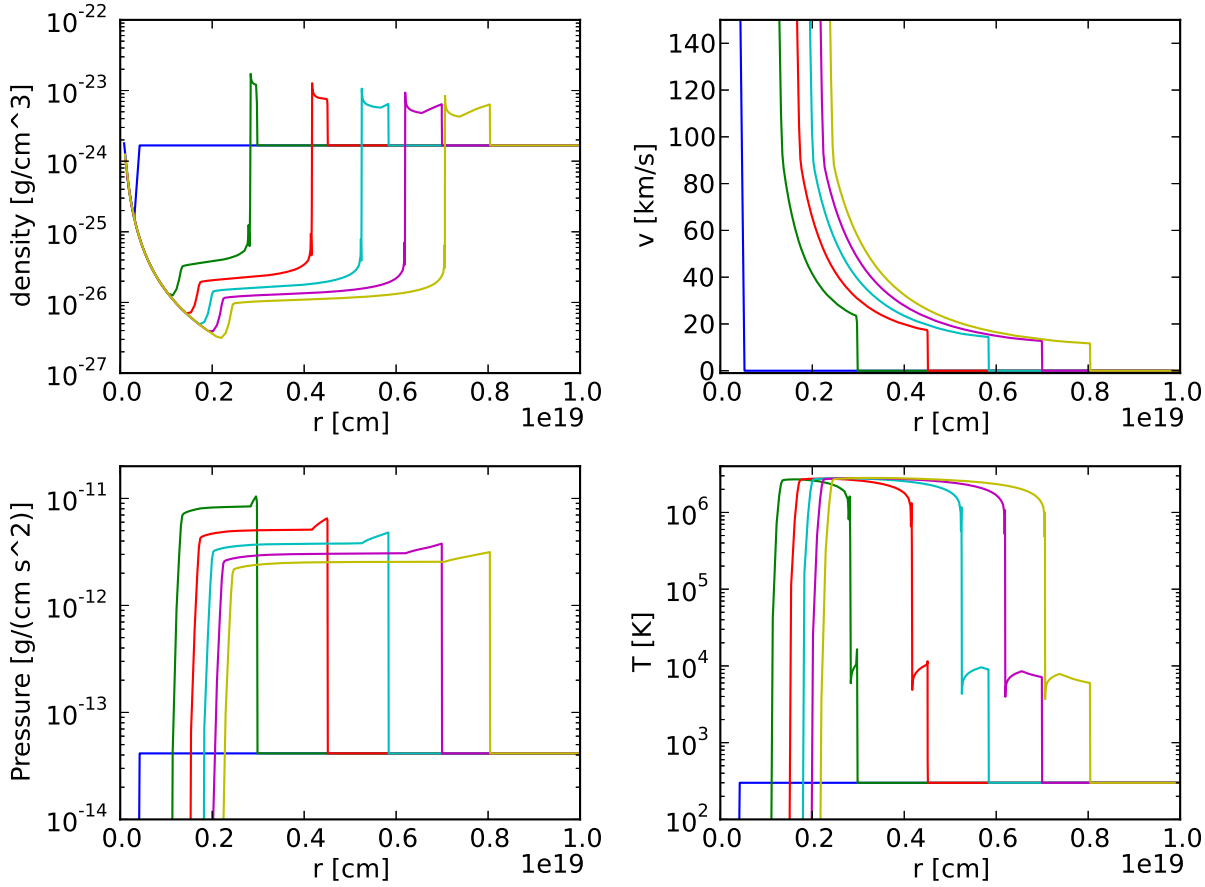

Figure 6.9: Long term evolution of the interaction between the novae and the interstellar medium. The curves show the parameters at 0, 0.2, 0.4, 0.8 and 1×10^5 yr. The swept up interstellar medium rapidly cools to 10^4 K, after which atomic cooling becomes inefficient.

cool to 10^4 K even if the density is a factor of 10 higher. However, clumps that form as the novae sweep up the red giant wind may be sufficiently dense to cool within 10^5 yr.

The column depth through the shocked interstellar medium is $10^{18}\,\mathrm{cm}^{-2}$ at 2×10^4 yr and $3 \times 10^{18}\,\mathrm{cm}^{-2}$ by 10^5 yr, which assuming solar metallicity (Asplund et al., 2009), could explain the column depth in sodium seen in Type Ia supernovae ($N_{\mathrm{Na}} \sim 10^{12}\,\mathrm{cm}^{-}2$) as long as the shell can cool sufficiently.

The velocities in the shell, $v_s \approx 20\,\mathrm{km\,s}^{-1}$, are lower than those typically seen in Type Ia supernovae, which are 50 to $100\,\mathrm{km\,s}^{-1}$. The difference could be explained if the supernova explodes a few 10^3 yr after the start of the symbiotic phase, or with a slightly lower interstellar medium

density. Observationally, the most significant difference would be the larger distance between the supernova and the shells, with would mean that little or no variation of the lines would be expected.

Perhaps the biggest difficulty comes from the assumption that the red-giant wind phase starts at a similar time to the nova phase. If there was a significant delay the wind may clear the region around the binary, and the novae would expand more freely because there would be less mass within the region. This would result in a larger velocity for the nova shells; however, the red-giant wind would not be dense enough to cool considerably as it is swept up by the novae.

Another case of interest are systems like U Scorpii, which undergo frequent recurrent novae but has a sub-giant or main sequence companion. In these cases a red-giant wind would not be present and the novae will interact directly will the interstellar medium. However, the late time evolution is likely to be similar to the calculation presented here, since the nova dominates the momentum, which drives the evolution. On the other hand, if the mass-transfer is sufficiently non-conservative then a disc-like outflow similar to the symbiotic case would be expected, but with higher velocity, although this will have little effect on the effective velocity used in these calculations.

Observations of supernova remnants provide support for the swept up interstellar medium as the origin of the circumstellar lines. Chiotellis et al. (2013) modelled X-ray emission from Tycho's supernova remnant, suggesting that the circumstellar environment was modified by a slow wind with a mass loss rate of $10^{-6} M_{\odot}\,\mathrm{yr}^{-1}$ that has swept the interstellar medium forming a shell. Similar mass loss-rates were also found for Kepler's supernova remnant (Patnaude et al., 2012) and RCW 86 (Broersen et al., 2014). These observations make a compelling case for the role interstellar medium in circumstellar shell formation and the origin of narrow absorption lines.

6.5 Summary

The interaction of recurrent nova shells with the circumsteller medium has been presented. The novae are shaped by the accretion disc within the first day, resulting in a bipolar outflow. In the polar directions the novae rapidly escape the circumstellar medium, while in the plane of the binary the shells are slowed by the dense outflow, which is swept up over a few years and forms a dense waist-like shell. Further novae interact within the first one, catching up the waist and driving a

shock through it. In the polar direction the interaction leads to a more clumpy shell, which is also at lower velocity than the first.

The absorption line evolution after the novae is governed by recombination and dilution as the shells expand. Components at velocities higher than $700\,\mathrm{km\,s^{-1}}$ are too dilute too be seen by the time they recombine, and at higher inclinations velocities $v \gtrsim 400\,\mathrm{km\,s^{-1}}$ are completely absent. As the shells evolve the higher velocity components weaken further, but strong absorption at $v \lesssim 250\,\mathrm{km\,s^{-1}}$ remains. These velocities are larger than the shell seen in RS Oph, but the difference supports the idea that the mass loss from the red giant is closer to $10^{-6} M_{\odot}\,\mathrm{yr^{-1}}$.

The evolution of the lines during the a supernova are consistent with some of the features seen in SN2006X. The highest density material is at the lowest velocity, which recombines the fastest and produces the strongest line profiles. Ab initio calculations suggest the recombination timescale is longer than that seen in SN2006X, but inclusion of a filling factor $f \sim 10^{-2}$ can account for the difference. Similarly, the nova shells may be narrower than those simulated, which could also account for the recurrence time.

Since the distance to the dense waist of the nova shells is only $3 \times 10^{15}\,\mathrm{cm}$, the shell is quickly swept up by the supernova, disappearing on timescales of 20 to 50 days, depending on inclination. To explain the components that are still visible after 150 days, multiple novae or a longer recurrence times are needed, although even then it is not clear whether the components could be seen.

The long term evolution of the interaction between the shells and the local interstellar medium may provide another way to explain the absorption lines. A one-dimensional model shows that the interaction would form a shell at 10^{18} to $10^{19}\,\mathrm{cm}$ after 10^{4} to $10^{5}\,\mathrm{yr}$. This shell is dense enough to cool within a few $10^{4}\,\mathrm{yr}$, and may be able to explain the absorption lines. The large distance would produce a component that does not vary with time, and the low density in the interstellar medium in elliptical galaxies would be able to explain the lack of absorption seen in supernovae in these galaxies.

A model based upon the long term mass loss from the progenitor will not be too sensitive to the details of the outflow. As long as the timescale is appropriate, then the density in the interstellar medium controls the ability of the shell to cool and therefore the presence or absence of the lines.

Furthermore, the model is not too reliant on a red-giant wind in between the novae because the interstellar medium shell velocity is controlled by the momentum, which is dominated by the novae. Although the velocity produced by the long-term evolution scenario is only $v \sim 20\,\mathrm{km\,s^{-1}}$, the model offers an explanation as to why the blue-shifted features are not seen in SN Ia hosted by elliptical galaxies.

Chapter 7

Conclusions and Outlook

The environment around Type Ia supernova progenitors provides interesting prospects for determining the nature of the system prior to the explosion. Specifically, the presence of a non-degenerate, possibly hydrogen-rich companion star at the time of explosion; and mass-loss prior to the explosion provide ways to determine if the progenitor system was single degenerate. In this work we have investigated the nature of the circumstellar medium prior to the explosion and the signatures of such an environment for single degenerate progenitors.

In Chapters 3 and 4 we investigate the dynamical interaction of a supernova with its companion and the surrounding interstellar or circumstellar medium. We use physically motivated model stars, including a sub-giant that could give rise to a Tycho-G like star after explosion (Kerzendorf et al., 2009) and a red giant, chosen to match the parameters of RS Oph, which is a symbiotic system and a recurrent nova that harbours a white-dwarf close to the Chandrasekhar mass (e.g. Sokoloski et al., 2006; Brandi et al., 2009).

Both of these companion stars have the majority of their envelopes stripped by the supernova, since both stars have extended, relatively weakly bound envelopes, a result that agrees with previous calculations involving giant stars (Marietta et al., 2000), and agrees surprisingly well with analytic theory (Wheeler et al., 1975). The stripped material in both systems remains at low velocity relative to the supernova, dominating the mass fraction for $v \lesssim 2000\,\mathrm{km\,s^{-1}}$, but a small fraction of the stripped companion material is found at high velocity, representing 0.2 per cent of the total material

at $10^4\,\mathrm{km\,s^{-1}}$.

We present a simple model for the Hα emission from the stripped companion material, based upon the detailed structure calculated from the simulations. The stripped hydrogen material is most dense in the centre of the supernova, which differs considerably from the uniform cores used in previous models that typically only extend to $1000\,\mathrm{km\,s^{-1}}$ (Mattila et al., 2005; Lundqvist et al., 2013). While our models produce lower luminosities for the uniform cores, we find that the realistic density profiles result in typically broader line profiles, extending up $10,000\,\mathrm{km\,s^{-1}}$ depending on viewing angle. We also find that realistic density profiles produce more luminous Hα emission. However, as the lines are considerably broader than previous calculations, the current observational limits may be less stringent.

As the supernova ages, interacting with the surrounding interstellar or circumstellar medium it becomes a supernova remnant (SNR). We find that the hole in the ejecta survives the interaction with the interstellar medium, at least until the age of Tycho's SNR ($\sim 440\,\mathrm{yr}$). This agrees with the schematic 2D models that have been conducted in the past (García-Senz et al., 2012). As the reverse shock is reaching the iron-rich ejecta by the age of Tycho's SNR we confirm the suggestion that the Fe Kα line traces the reverse shock (Warren et al., 2005).

Our models produce a broken ring for the reverse shock, as has been observed in Tycho's SNR (Warren et al., 2005). If the observed structure is indeed caused by the asymmetry introduced by the supernova-companion interaction, then the relatively large size of the observed hole suggests a higher mass companion, $M \sim 2M_\odot$, consistent with the slow AGB winds suggested by X-ray modelling (Chiotellis et al., 2012). This model can be tested in a number of ways. Firstly, any remnant of the companion star should be moving approximately perpendicular to the direction of the hole. Secondly, the hole should be filled with relatively low density hydrogen rich material, giving rise to different X-ray emission properties. It is known that the emission in the region of the hole is different (e.g. Hayato et al., 2010); however, it needs to be confirmed whether this is compatible with hydrogen rich material.

Furthermore, while the low density will mean the emission is weak, X-ray models suggest using a slow AGB wind that is concentrated in the binary plane and produces higher densities in the hole.

These models produce elliptical remnants, which since Tycho's SNR is spherical would suggest that Tycho's SNR is aligned along the binary axis and that motion of a surviving companion star should be in the plane of the sky. In addition, the density gradient along the line of sight produces multiple shocks in the region of the hole, which have been observed. However, these could also be explained by structure in the interstellar medium.

In chapters 5 and 6 we consider the detailed structure formed as recurrent novae interact with a slow wind from a binary. The models are chosen to represent RS Ophiuchi, a symbiotic system and potential Type Ia supernova progenitor. We find the wind is concentrated in the binary plane, and with sufficient cooling an accretion disc forms. The accretion disc extends to 10^{13} cm and is elliptical, which may explain why previous attempts to model the hot component have been unsuccessful. We find that the accretion disc survives the passage of the novae, but drives a wind from its surface once the shell has passed. As the novae sweep up the wind, the shell becomes bipolar and clumpy, with multiple velocity components along a given line of sight.

In order to explain the circumstellar metal lines seen in RS Oph, the mass-loss should be significantly higher $10^{-7} M_{\odot}\,\mathrm{yr}^{-1}$ in order for there to be sufficient mass close to the binary to prevent the white dwarf ionizing the entire system. We find quiescent line profiles produced in the wind that are stable, similar to those observed, albeit at lower velocity. We also find that the flow includes a polar component that is falling back onto the white-dwarf, which can explain the red-shifted components to the observed absorption lines.

Once the super-soft source phase of the novae ends, we find absorption line profiles that weaken and slow down as time progresses. If such behaviour is observed, then it would be strong evidence for the contribution from nova shells. As well as lower velocity components that form in the shell, there is also high velocity material that may also be detectable.

While the detection of the nova shells through absorption lines is possible for recurrent nova systems, the high ionizing flux from a supernova may mean that the shells are not observed in Type Ia supernovae, even if they are present. Despite this, the simulations produce a number of features observed in SN 2006X. Firstly that the low velocity components are strongest and form in the densest material, and are also closest to the centre of the system, thus disappear first when the

supernova sweeps them up, so SN 2006X may represent an extreme case of mass-loss prior to the explosion.

Even if individual novae are not the explanation for the absorption lines seen in some SN Ia, the pile up of nova shells as they sweep up the interstellar medium or a slow wind may be able to. The combined shells have much greater mass, but typically lower velocities and greater distances, and may be able to explain an excess of time-independent blue shifted absorption lines (Maguire et al., 2013). Furthermore, if the interstellar medium plays a role in the pile up of the shells, then it would explain why no circumstellar absorption lines have been detected in SN Ia that occur in elliptical galaxies.

There remain a number of difficulties for the single-degenerate model for Type Ia supernovae, including the possibility of detectable hydrogen emission and that in the case of some nearby supernovae giant companions should have been directly observable in pre-explosion images. However, the circumstellar environment from single-degenerate progenitors offers some interesting solutions to other problems, like the X-ray emission from SNRs or the origin of absorption lines. Therefore, we see the environment around supernovae continuing to be complimentary to direct modelling of the explosion, the structure of the supernova and its nucleosynthesis.

7.1 Further work

The nature of SN Ia progenitors remains divided, and further investigation is clearly required to help resolve the situation. Based upon what we have learnt in this thesis we suggest some extensions that would help to resolve some of the issues.

Detailed modelling of the emission lines from stripped companion material using multidimensional models that include the appropriate structure are clearly important for assessing the detectability of this material, and that for the case of hydrogen an accurate treatment of Lyman α is critical for determining the luminosity. Looking for broader emission lines may help to rule out, or confirm the presence hydrogen rich material in the nebular phase, while deep X-ray observations of young supernova remnants may also be able to confirm the presence of any such material.

Our understanding of the circumstellar structure in symbiotic novae could be enhanced by

simulations that include either radiative acceleration, or disc winds driven from the accretion disc around the white-dwarf. The combination of binary wind calculations and accretion simulations could help to determine the nature of accretion in symbiotic systems, which could help us learn more about the novae and the mass of the white dwarfs hosted.

Long-term calculations of the evolution novae would help to elude the prospects for the formation of absorption lines from the pile up of winds or nova shells. If such calculations can reproduce the absorption lines, then the two separate observations of the supernovae and their remnants would provide strong evidence for the single-degenerate model.

Finally, a natural extension of the work would be to cover a broader range of progenitor scenarios. By understanding how ionization from the supernova affects its environment, the circumstellar densities and mass required to produce the observed lines could be determined. This would help to extend the tests to a variety of stellar models, helping to produce an unbiased picture of the progenitors of SNe Ia.

Bibliography

Agertz, O., Moore, B., Stadel, J., Potter, D., Miniati, F. et al., 2007. Fundamental differences between SPH and grid methods. *MNRAS*, **380**, 963–978.

Aldering, G., Antilogus, P., Bailey, S., Baltay, C., Bauer, A. et al., 2006. Nearby Supernova Factory Observations of SN 2005gj: Another Type Ia Supernova in a Massive Circumstellar Envelope. *ApJ*, **650**, 510–527.

Ambwani, K. & Sutherland, P., 1988. Gamma-ray spectra and energy deposition for type IA supernovae. *ApJ*, **325**, 820–827.

Anderson, J. P., Habergham, S. M., James, P. A. & Hamuy, M., 2012. The Local Environments of Core-Collapse SNe within Host Galaxies. In *Death of Massive Stars: Supernovae and Gamma-Ray Bursts*, vol. 279 of *IAU Symposium*, 183–186.

Anupama, G. C., 2008. One Year of Monitoring of the 2006 Outburst in Optical and Low Radio Frequencies. In A. Evans, M. F. Bode, T. J. O'Brien & M. J. Darnley, eds., *RS Ophiuchi (2006) and the Recurrent Nova Phenomenon*, vol. 401 of *Astronomical Society of the Pacific Conference Series*, 251.

Anupama, G. C. & Mikołajewska, J., 1999. Recurrent novae at quiescence: systems with giant secondaries. *A&A*, **344**, 177–187.

Arnett, W. D., 1969. A Possible Model of Supernovae: Detonation of ^{12}C. *Astrophysics and Space Science*, **5**, 180–212.

Arnett, W. D., Truran, J. W. & Woosley, S. E., 1971. Nucleosynthesis in Supernova Models. II. The ^{12}C Detonation Model. *ApJ*, **165**, 87.

Asplund, M., Grevesse, N., Sauval, A. J. & Scott, P., 2009. The Chemical Composition of the Sun. *ARA&A*, **47**, 481–522.

Badenes, C. & Maoz, D., 2012. The Merger Rate of Binary White Dwarfs in the Galactic Disk. *ApJ*, **749**, L11.

Balsara, D. S., 1995. von Neumann stability analysis of smooth particle hydrodynamics–suggestions for optimal algorithms. *Journal of Computational Physics*, **121**, 357–372.

Barnes, J. & Hut, P., 1986. A hierarchical O(N log N) force-calculation algorithm. *Nature*, **324**, 446–449.

Barry, R. K., Mukai, K., Sokoloski, J. L., Danchi, W. C., Hachisu, I., Evans, A., Gehrz, R. & Mikolajewska, J., 2008. On the Distance of RS Ophiuchi. In A. Evans, M. F. Bode, T. J. O'Brien & M. J. Darnley, eds., *RS Ophiuchi (2006) and the Recurrent Nova Phenomenon*, vol. 401 of *Astronomical Society of the Pacific Conference Series*, 52.

Bianco, F. B., Howell, D. A., Sullivan, M., Conley, A., Kasen, D. et al., 2011. Constraining Type Ia Supernovae Progenitors from Three Years of Supernova Legacy Survey Data. *ApJ*, **741**, 20.

Blondin, S., Prieto, J. L., Patat, F., Challis, P., Hicken, M., Kirshner, R. P., Matheson, T. & Modjaz, M., 2009. A Second Case of Variable Na I D Lines in a Highly Reddened Type Ia Supernova. *ApJ*, **693**, 207–215.

Bode, M. F., Harman, D. J., O'Brien, T. J., Bond, H. E., Starrfield, S., Darnley, M. J., Evans, A. & Eyres, S. P. S., 2007. Hubble Space Telescope Imaging of the Expanding Nebular Remnant of the 2006 Outburst of the Recurrent Nova RS Ophiuchi. *ApJ*, **665**, L63–L66.

Branch, D., 1998. Type IA Supernovae and the Hubble Constant. *ARA&A*, **36**, 17–56.

Brandi, E., Quiroga, C., Mikołajewska, J., Ferrer, O. E. & García, L. G., 2009. Spectroscopic orbits and variations of RS Ophiuchi. *A&A*, **497**, 815–825.

Broersen, S., Chiotellis, A., Vink, J. & Bamba, A., 2014. The many sides of RCW 86: a Type Ia supernova remnant evolving in its progenitor's wind bubble. *MNRAS*, **441**, 3040–3054.

Bruenn, S. W., 1973. Thermal Consequences of the Convectively Driven URCA Process. *ApJ*, **183**, L125.

Bulla, M., 2013. *A high resolution spectroscopic study of the recurrent nova RS Oph and its link to Type Ia Supernova progenitors*. Master's thesis, University of Milan.

Cappellaro, E., Turatto, M., Tsvetkov, D. Y., Bartunov, O. S., Pollas, C., Evans, R. & Hamuy, M., 1997. The rate of supernovae from the combined sample of five searches. *A&A*, **322**, 431–441.

Castor, J. I., 1970. Spectral line formation in Wolf-Rayet envelopes. *MNRAS*, **149**, 111–127.

Cen, R., 1992. A hydrodynamic approach to cosmology - Methodology. *ApJS*, **78**, 341–364.

Chevalier, R. A., 1981. Exploding white dwarf models for Type I supernovae. *ApJ*, **246**, 267–277.

Chiotellis, A., Kosenko, D., Schure, K. M., Vink, J. & Kaastra, J. S., 2013. Modelling the interaction of thermonuclear supernova remnants with circumstellar structures: the case of Tycho's supernova remnant. *MNRAS*, **435**, 1659–1670.

Chiotellis, A., Schure, K. M. & Vink, J., 2012. The imprint of a symbiotic binary progenitor on the properties of Kepler's supernova remnant. *A&A*, **537**, A139.

Chomiuk, L., Soderberg, A. M., Moe, M., Chevalier, R. A., Rupen, M. P., Badenes, C., Margutti, R., Fransson, C., Fong, W.-f. & Dittmann, J. A., 2012. EVLA Observations Constrain the Environment and Progenitor System of Type Ia Supernova 2011fe. *ApJ*, **750**, 164.

Chugai, N. N., 1987. Scattering of L photons in an infinite expanding medium when there is absorption in the continuum. *Astrophysics*, **26**, 53–57.

Chugai, N. N., 2008. Circumstellar Na I and Ca II absorption lines of type Ia supernovae in the symbiotic scenario. *Astronomy Letters*, **34**, 389–396.

Colgate, S. A., 1970. Ejection of Companion Objects by Supernovae. *Nature*, **225**, 247–248.

Colgate, S. A. & McKee, C., 1969. Early Supernova Luminosity. *ApJ*, **157**, 623.

Creasey, P., Theuns, T., Bower, R. G. & Lacey, C. G., 2011. Numerical overcooling in shocks. *MNRAS*, **415**, 3706–3720.

Dan, M., Rosswog, S., Brüggen, M. & Podsiadlowski, P., 2014. The structure and fate of white dwarf merger remnants. *MNRAS*, **438**, 14–34.

Dan, M., Rosswog, S., Guillochon, J. & Ramirez-Ruiz, E., 2012. How the merger of two white dwarfs depends on their mass ratio: orbital stability and detonations at contact. *MNRAS*, **422**, 2417–2428.

Darnley, M. J., Hounsell, R. A. & Bode, M. F., 2008. Liverpool Telescope Optical Photometry Following the 2006 Outburst of RS Ophiuchi. In A. Evans, M. F. Bode, T. J. O'Brien & M. J. Darnley, eds., *RS Ophiuchi (2006) and the Recurrent Nova Phenomenon*, vol. 401 of *Astronomical Society of the Pacific Conference Series*, 203.

Das, R., Banerjee, D. P. K. & Ashok, N. M., 2006. A Near-Infrared Shock Wave in the 2006 Outburst of Recurrent Nova RS Ophiuchi. *ApJ*, **653**, L141–L144.

Dehnen, W., 2001. Towards optimal softening in three-dimensional N-body codes - I. Minimizing the force error. *MNRAS*, **324**, 273–291.

Dessart, L., Hillier, D. J., Blondin, S. & Khokhlov, A., 2013. The critical ingredients of SN Ia radiative-transfer modelling. *ArXiv e-prints*.

Dilday, B., Howell, D. A., Cenko, S. B., Silverman, J. M., Nugent, P. E. et al., 2012. PTF 11kx: A Type Ia Supernova with a Symbiotic Nova Progenitor. *Science*, **337**, 942–.

Dobrzycka, D. & Kenyon, S. J., 1994. A new spectroscopic orbit for RS Ophiuchi. *AJ*, **108**, 2259–2266.

Dobrzycka, D., Kenyon, S. J., Proga, D., Mikolajewska, J. & Wade, R. A., 1996. The Hot Component of RS Ophiuchi. *AJ*, **111**, 2090.

Drew, J. E. & Proga, D., 2000. Radiation-driven accretion disk winds. *New Astronomy Reviews*, **44**, 21–26.

Durier, F. & Dalla Vecchia, C., 2012. Implementation of feedback in smoothed particle hydrodynamics: towards concordance of methods. *MNRAS*, **419**, 465–478.

Dwarkadas, V. V. & Chevalier, R. A., 1998. Interaction of Type IA Supernovae with Their Surroundings. *ApJ*, **497**, 807.

Eggleton, P. P., 1983. Approximations to the radii of Roche lobes. *ApJ*, **268**, 368.

Evans, A., Woodward, C. E., Helton, L. A., van Loon, J. T., Barry, R. K. et al., 2007. Silicate Dust in the Environment of RS Ophiuchi following the 2006 Eruption. *ApJ*, **671**, L157–L160.

Fekel, F. C., Joyce, R. R., Hinkle, K. H. & Skrutskie, M. F., 2000. Infrared Spectroscopy of Symbiotic Stars. I. Orbits for Well-Known S-Type Systems. *AJ*, **119**, 1375–1388.

Field, G. B., 1965. Thermal Instability. *ApJ*, **142**, 531.

Filippenko, A. V., Richmond, M. W., Branch, D., Gaskell, M., Herbst, W., Ford, C. H., Treffers, R. R., Matheson, T., Ho, L. C., Dey, A., Sargent, W. L. W., Small, T. A. & van Breugel, W. J. M., 1992a. The subluminous, spectroscopically peculiar type IA supernova 1991bg in the elliptical galaxy NGC 4374. *AJ*, **104**, 1543–1556.

Filippenko, A. V., Richmond, M. W., Matheson, T., Shields, J. C., Burbidge, E. M., Cohen, R. D., Dickinson, M., Malkan, M. A., Nelson, B., Pietz, J., Schlegel, D., Schmeer, P., Spinrad, H., Steidel, C. C., Tran, H. D. & Wren, W., 1992b. The peculiar Type IA SN 1991T - Detonation of a white dwarf? *ApJ*, **384**, L15–L18.

Fink, M., Röpke, F. K., Hillebrandt, W., Seitenzahl, I. R., Sim, S. A. & Kromer, M., 2010. Double-detonation sub-Chandrasekhar supernovae: can minimum helium shell masses detonate the core? *A&A*, **514**, A53.

Fransson, C., Lundqvist, P. & Chevalier, R. A., 1996. Circumstellar Interaction in SN 1993J. *ApJ*, **461**, 993.

Fryxell, B. A. & Arnett, W. D., 1981. Hydrodynamic effects of a stellar explosion on a binary companion star. *ApJ*, **243**, 994–1002.

Fuller, J. & Lai, D., 2012. Dynamical tides in compact white dwarf binaries: tidal synchronization and dissipation. *MNRAS*, **421**, 426–445.

García-Senz, D., Badenes, C. & Serichol, N., 2012. Is There a Hidden Hole in Type Ia Supernova Remnants? *ApJ*, **745**, 75.

Gilfanov, M. & Bogdán, Á., 2010. An upper limit on the contribution of accreting white dwarfs to the typeIa supernova rate. *Nature*, **463**, 924–925.

Gull, S. F., 1973. A numerical model of the structure and evolution of young supernovaremnants. *MNRAS*, **161**, 47–69.

Hairer, E., Lubich, C. & Wanner, G., 2006. *Geometric Numerical Integration*. Springer, Berlin, 2nd ed.

Hamuy, M., Phillips, M. M., Maza, J., Suntzeff, N. B., Schommer, R. A. & Aviles, R., 1995. A Hubble diagram of distant type IA supernovae. *AJ*, **109**, 1–13.

Hamuy, M., Phillips, M. M., Suntzeff, N. B., Maza, J., González, L. E., Roth, M., Krisciunas, K., Morrell, N., Green, E. M., Persson, S. E. & McCarthy, P. J., 2003. An asymptotic-giant-branch star in the progenitor system of a type Ia supernova. *Nature*, **424**, 651–654.

Hayato, A., Yamaguchi, H., Tamagawa, T., Katsuda, S., Hwang, U., Hughes, J. P., Ozawa, M., Bamba, A., Kinugasa, K., Terada, Y., Furuzawa, A., Kunieda, H. & Makishima, K., 2010. Expansion Velocity of Ejecta in Tycho's Supernova Remnant Measured by Doppler Broadened X-ray Line Emission. *ApJ*, **725**, 894–903.

Hoeflich, P. & Khokhlov, A., 1996. Explosion Models for Type IA Supernovae: A Comparison with Observed Light Curves, Distances, H 0, and Q 0. *ApJ*, **457**, 500.

Hopkins, P. F., 2013. A general class of Lagrangian smoothed particle hydrodynamics methods and implications for fluid mixing problems. *MNRAS*, **428**, 2840–2856.

Horesh, A., Kulkarni, S. R., Fox, D. B., Carpenter, J., Kasliwal, M. M. et al., 2012. Early Radio and X-Ray Observations of the Youngest nearby Type Ia Supernova PTF 11kly (SN 2011fe). *ApJ*, **746**, 21.

Hoyle, F. & Fowler, W. A., 1960. Nucleosynthesis in Supernovae. *ApJ*, **132**, 565.

Hui, L. & Gnedin, N. Y., 1997. Equation of state of the photoionized intergalactic medium. *MNRAS*, **292**, 27.

Hummer, D. G. & Rybicki, G. B., 1985. The Sobolev approximation for line formation with continuous opacity. *ApJ*, **293**, 258–267.

Iben, Jr., I., 1982. More on carbon burning in electron-degenerate matter - Within single stars of intermediate mass and within accreting white dwarfs. *ApJ*, **253**, 248–259.

Iben, Jr., I. & Tutukov, A. V., 1984. The evolution of low-mass close binaries influenced by the radiation of gravitational waves and by a magnetic stellar wind. *ApJ*, **284**, 719–744.

Iijima, T., 2008. Circumstellar Envelope of RS Ophiuchi. In A. Evans, M. F. Bode, T. J. O'Brien & M. J. Darnley, eds., *RS Ophiuchi (2006) and the Recurrent Nova Phenomenon*, vol. 401 of *Astronomical Society of the Pacific Conference Series*, 115.

Iijima, T., 2009. Spectral evolution of the recurrent nova RS Ophiuchi during the 2006 outburst and some mysterious phenomena. *A&A*, **505**, 287–298.

Jerkstrand, A., Fransson, C., Maguire, K., Smartt, S., Ergon, M. & Spyromilio, J., 2012. The progenitor mass of the Type IIP supernova SN 2004et from late-time spectral modeling. *A&A*, **546**, A28.

Johnson, L. C., 1972. Approximations for Collisional and Radiative Transition Rates in Atomic Hydrogen. *ApJ*, **174**, 227.

Justham, S., 2011. Single-degenerate Type Ia Supernovae Without Hydrogen Contamination. *ApJ*, **730**, L34.

Kahabka, P. & van den Heuvel, E. P. J., 1997. Luminous Supersoft X-Ray Sources. *ARA&A*, **35**, 69–100.

Kasen, D., 2010. Seeing the Collision of a Supernova with Its Companion Star. *ApJ*, **708**, 1025–1031.

Kato, M. & Hachisu, I., 1994. Optically thick winds in nova outbursts. *ApJ*, **437**, 802–826.

Kelly, P. L., Fox, O. D., Filippenko, A. V., Cenko, S. B., Prato, L., Schaefer, G., Shen, K. J., Zheng, W., Graham, M. L. & Tucker, B. E., 2014. Constraints on the Progenitor System of the Type Ia Supernova 2014J from Pre-Explosion Hubble Space Telescope Imaging. *ArXiv e-prints*.

Kerzendorf, W. E., Childress, M., Scharwächter, J., Do, T. & Schmidt, B. P., 2014. A Reconnaissance of the Possible Donor Stars to the Kepler Supernova. *ApJ*, **782**, 27.

Kerzendorf, W. E., Schmidt, B. P., Asplund, M., Nomoto, K., Podsiadlowski, P., Frebel, A., Fesen, R. A. & Yong, D., 2009. Subaru High-Resolution Spectroscopy of Star G in the Tycho Supernova Remnant. *ApJ*, **701**, 1665–1672.

Kerzendorf, W. E., Yong, D., Schmidt, B. P., Simon, J. D., Jeffery, C. S., Anderson, J., Podsiadlowski, P., Gal-Yam, A., Silverman, J. M., Filippenko, A. V., Nomoto, K., Murphy, S. J., Bessell, M. S., Venn, K. A. & Foley, R. J., 2013. A High-resolution Spectroscopic Search for the Remaining Donor for Tycho's Supernova. *ApJ*, **774**, 99.

Kessel-Deynet, O. & Burkert, A., 2000. Ionizing radiation in smoothed particle hydrodynamics. *MNRAS*, **315**, 713–721.

Khokhlov, A. M., 1991. Nucleosynthesis in delayed detonation models of Type IA supernovae. *A&A*, **245**, L25–L28.

Kozma, C. & Fransson, C., 1992. Gamma-ray deposition and nonthermal excitation in supernovae. *ApJ*, **390**, 602–621.

Kromer, M., Pakmor, R., Taubenberger, S., Pignata, G., Fink, M., Röpke, F. K., Seitenzahl, I. R., Sim, S. A. & Hillebrandt, W., 2013. SN 2010lp - a Type Ia Supernova from a Violent Merger of Two Carbon-Oxygen White Dwarfs. *ApJ*, **778**, L18.

Kromer, M., Sim, S. A., Fink, M., Röpke, F. K., Seitenzahl, I. R. & Hillebrandt, W., 2010. Double-detonation Sub-Chandrasekhar Supernovae: Synthetic Observables for Minimum Helium Shell Mass Models. *ApJ*, **719**, 1067–1082.

Leonard, D. C., 2007. Constraining the Type Ia Supernova Progenitor: The Search for Hydrogen in Nebular Spectra. *ApJ*, **670**, 1275–1282.

Lesaffre, P., Han, Z., Tout, C. A., Podsiadlowski, P. & Martin, R. G., 2006. The C flash and the ignition conditions of Type Ia supernovae. *MNRAS*, **368**, 187–195.

Li, W., Bloom, J. S., Podsiadlowski, P., Miller, A. A., Cenko, S. B. et al., 2011. Exclusion of a luminous red giant as a companion star to the progenitor of supernova SN 2011fe. *Nature*, **480**, 348–350.

Li, W., Filippenko, A. V., Chornock, R., Berger, E., Berlind, P., Calkins, M. L., Challis, P., Fassnacht, C., Jha, S., Kirshner, R. P., Matheson, T., Sargent, W. L. W., Simcoe, R. A., Smith, G. H. & Squires, G., 2003. SN 2002cx: The Most Peculiar Known Type Ia Supernova. *PASP*, **115**, 453–473.

Liu, Z. W., Pakmor, R., Röpke, F. K., Edelmann, P., Wang, B., Kromer, M., Hillebrandt, W. & Han, Z. W., 2012. Three-dimensional simulations of the interaction between Type Ia supernova ejecta and their main sequence companions. *A&A*, **548**, A2.

Livne, E., Tuchman, Y. & Wheeler, J. C., 1992. Explosion of a supernova with a red giant companion. *ApJ*, **399**, 665–671.

Lopez, L. A., Ramirez-Ruiz, E., Huppenkothen, D., Badenes, C. & Pooley, D. A., 2011. Using the X-ray Morphology of Young Supernova Remnants to Constrain Explosion Type, Ejecta Distribution, and Chemical Mixing. *ApJ*, **732**, 114.

Lucy, L. B., 2005. Monte Carlo techniques for time-dependent radiative transfer in 3-D supernovae. *A&A*, **429**, 19–30.

Lundqvist, P., Mattila, S., Sollerman, J., Kozma, C., Baron, E., Cox, N. L. J., Fransson, C., Leibundgut, B. & Spyromilio, J., 2013. Hydrogen and helium in the spectra of Type Ia supernovae. *MNRAS*, **435**, 329–345.

Maguire, K., Sullivan, M., Ellis, R. S., Nugent, P. E., Howell, D. A. et al., 2012. Hubble Space Telescope studies of low-redshift Type Ia supernovae: evolution with redshift and ultraviolet spectral trends. *MNRAS*, **426**, 2359–2379.

Maguire, K., Sullivan, M., Patat, F., Gal-Yam, A., Hook, I. M. et al., 2013. A statistical analysis of circumstellar material in Type Ia supernovae. *ArXiv e-prints*.

Mannucci, F., Della Valle, M. & Panagia, N., 2006. Two populations of progenitors for Type Ia supernovae? *MNRAS*, **370**, 773–783.

Maoz, D., Mannucci, F. & Brandt, T. D., 2012. The delay-time distribution of Type Ia supernovae from Sloan II. *MNRAS*, **426**, 3282–3294.

Maoz, D., Sharon, K. & Gal-Yam, A., 2010. The Supernova Delay Time Distribution in Galaxy Clusters and Implications for Type-Ia Progenitors and Metal Enrichment. *ApJ*, **722**, 1879–1894.

Marietta, E., Burrows, A. & Fryxell, B., 2000. Type IA Supernova Explosions in Binary Systems: The Impact on the Secondary Star and Its Consequences. *ApJS*, **128**, 615–650.

Mason, E., Ederoclite, A., Williams, R. E., Della Valle, M. & Setiawan, J., 2012. <ASTROBJ>U Scorpii</ASTROBJ> 2010 outburst: a new understanding of the binary accretion disk and the secondary star. *A&A*, **544**, A149.

Mattila, S., Lundqvist, P., Sollerman, J., Kozma, C., Baron, E., Fransson, C., Leibundgut, B. & Nomoto, K., 2005. Early and late time VLT spectroscopy of SN 2001el - progenitor constraints for a type Ia supernova. *A&A*, **443**, 649–662.

Mazzali, P. A. & Lucy, L. B., 1993. The application of Monte Carlo methods to the synthesis of early-time supernovae spectra. *A&A*, **279**, 447–456.

Mazzali, P. A., Nomoto, K., Patat, F. & Maeda, K., 2001. The Nebular Spectra of the Hypernova SN 1998bw and Evidence for Asymmetry. *ApJ*, **559**, 1047–1053.

Mazzali, P. A., Sauer, D. N., Pastorello, A., Benetti, S. & Hillebrandt, W., 2008. Abundance stratification in Type Ia supernovae - II. The rapidly declining, spectroscopically normal SN2004eo. *MNRAS*, **386**, 1897–1906.

Mazzali, P. A., Sullivan, M., Hachinger, S., Ellis, R. S., Nugent, P. E., Howell, D. A., Gal-Yam, A., Maguire, K., Cooke, J., Thomas, R., Nomoto, K. & Walker, E. S., 2014. Hubble Space Telescope spectra of the Type Ia supernova SN 2011fe: a tail of low-density, high-velocity material with $Z < Z_{\odot}$. *MNRAS*, **439**, 1959–1979.

Milne, P. A., Hungerford, A. L., Fryer, C. L., Evans, T. M., Urbatsch, T. J., Boggs, S. E., Isern, J., Bravo, E., Hirschmann, A., Kumagai, S., Pinto, P. A. & The, L.-S., 2004. Unified One-Dimensional Simulations of Gamma-Ray Line Emission from Type Ia Supernovae. *ApJ*, **613**, 1101–1119.

Minkowski, R., 1939. The Spectra of the Supernovae in IC 4182 and in NGC 1003. *ApJ*, **89**, 156.

Mohamed, S., 2010. *A ẄonderfulM̈use: Mass-Transfer in Mira-type Binaries*. Ph.D. thesis, University of Oxford.

Mohamed, S., Mackey, J. & Langer, N., 2012. 3D simulations of Betelgeuse's bow shock. *A&A*, **541**, A1.

Moll, R. & Woosley, S. E., 2013. Multi-dimensional Models for Double Detonation in Sub-Chandrasekhar Mass White Dwarfs. *ApJ*, **774**, 137.

Monaghan, J. J., 1997. SPH and Riemann Solvers. *Journal of Computational Physics*, **136**, 298–307.

Moore, K. & Bildsten, L., 2012. Circumstellar Shell Formation in Symbiotic Recurrent Novae. *ApJ*, **761**, 182.

Mukai, K., 2008. RS Ophiuchi in Quiescence: Why is it X-ray Faint? In A. Evans, M. F. Bode, T. J. O'Brien & M. J. Darnley, eds., *RS Ophiuchi (2006) and the Recurrent Nova Phenomenon*, vol. 401 of *Astronomical Society of the Pacific Conference Series*, 84.

Nelson, T., Mukai, K., Orio, M., Luna, G. J. M. & Sokoloski, J. L., 2011. X-Ray and Ultraviolet Emission from the Recurrent Nova RS Ophiuchi in Quiescence: Signatures of Accretion and Shocked Gas. *ApJ*, **737**, 7.

Nomoto, K., 1982a. Accreting white dwarf models for type I supernovae. I - Presupernova evolution and triggering mechanisms. *ApJ*, **253**, 798–810.

Nomoto, K., 1982b. Accreting white dwarf models for type I supernovae. II - Off-center detonation supernovae. *ApJ*, **257**, 780–792.

Nomoto, K. & Iben, Jr., I., 1985. Carbon ignition in a rapidly accreting degenerate dwarf - A clue to the nature of the merging process in close binaries. *ApJ*, **297**, 531–537.

Nomoto, K., Nariai, K. & Sugimoto, D., 1979. Rapid Mass Accretion onto White Dwarfs and Formation of an Extended Envelope. *PASJ*, **31**, 287–298.

Nomoto, K., Saio, H., Kato, M. & Hachisu, I., 2007. Thermal Stability of White Dwarfs Accreting Hydrogen-rich Matter and Progenitors of Type Ia Supernovae. *ApJ*, **663**, 1269–1276.

Nomoto, K., Thielemann, F.-K. & Yokoi, K., 1984. Accreting white dwarf models of Type I supernovae. III - Carbon deflagration supernovae. *ApJ*, **286**, 644–658.

Ntormousi, E., Burkert, A., Fierlinger, K. & Heitsch, F., 2011. Formation of Cold Filamentary Structure from Wind-blown Superbubbles. *ApJ*, **731**, 13.

Nussbaumer, H. & Schmutz, W., 1984. The hydrogenic 2s-1s two-photon emission. *A&A*, **138**, 495.

O'Brien, T. J., Beswick, R. J., Bode, M. F., Eyres, S. P. S., Muxlow, T. W. B., Garrington, S. T., Porcas, R. W., Evans, A. & Davis, R. J., 2008. MERLIN and VLBI Radio Imaging of RS Ophiuchi Following the 2006 Outburst. In A. Evans, M. F. Bode, T. J. O'Brien & M. J. Darnley, eds., *RS Ophiuchi (2006) and the Recurrent Nova Phenomenon*, vol. 401 of *Astronomical Society of the Pacific Conference Series*, 239.

Orlando, S., Drake, J. J. & Laming, J. M., 2009. Three-dimensional modeling of the asymmetric blast wave from the 2006 outburst of RS Ophiuchi: Early X-ray emission. *A&A*, **493**, 1049–1059.

Osborne, J. P., Page, K. L., Beardmore, A. P., Bode, M. F., Goad, M. R., O'Brien, T. J., Starrfield, S., Rauch, T., Ness, J.-U., Krautter, J., Schwarz, G., Burrows, D. N., Gehrels, N., Drake, J. J., Evans, A. & Eyres, S. P. S., 2011. The Supersoft X-ray Phase of Nova RS Ophiuchi 2006. *ApJ*, **727**, 124.

Osterbrock, D. E., 1989. *Astrophysics of gaseous nebulae and active galactic nuclei*.

Paczyński, B., 1972. Carbon Ignition in Degenerate Stellar Cores. *Astrophysical Letters*, **11**, 53.

Pakmor, R., Kromer, M., Taubenberger, S., Sim, S. A., Röpke, F. K. & Hillebrandt, W., 2012. Normal Type Ia Supernovae from Violent Mergers of White Dwarf Binaries. *ApJ*, **747**, L10.

Pakmor, R., Röpke, F. K., Weiss, A. & Hillebrandt, W., 2008. The impact of type Ia supernovae on main sequence binary companions. *A&A*, **489**, 943–951.

Pan, K.-C., Ricker, P. M. & Taam, R. E., 2012. Impact of Type Ia Supernova Ejecta on Binary Companions in the Single-degenerate Scenario. *ApJ*, **750**, 151.

Parker, E. N., 1953. Instability of Thermal Fields. *ApJ*, **117**, 431.

Patat, F., Chandra, P., Chevalier, R., Justham, S., Podsiadlowski, P. et al., 2007. Detection of Circumstellar Material in a Normal Type Ia Supernova. *Science*, **317**, 924–.

Patat, F., Chugai, N. N., Podsiadlowski, P., Mason, E., Melo, C. & Pasquini, L., 2011. Connecting RS Ophiuchi to [some] type Ia supernovae. *A&A*, **530**, A63.

Patnaude, D. J., Badenes, C., Park, S. & Laming, J. M., 2012. The Origin of Kepler's Supernova Remnant. *ApJ*, **756**, 6.

Phillips, A. P., Pettini, M. & Gondhalekar, P. M., 1984. Element depletions in interstellar gas. II - The density-dependence of calcium and sodium depletions. *MNRAS*, **206**, 337–350.

Phillips, M. M., 1993. The absolute magnitudes of Type IA supernovae. *ApJ*, **413**, L105–L108.

Podsiadlowski, P. & Mohamed, S., 2007. The Origin and Evolution of Symbiotic Binaries. *Baltic Astronomy*, **16**, 26–33.

Podsiadlowski, P., Rappaport, S. & Pfahl, E. D., 2002. Evolutionary Sequences for Low- and Intermediate-Mass X-Ray Binaries. *ApJ*, **565**, 1107–1133.

Prialnik, D. & Kovetz, A., 1992. Classical nova models with accretion heating at accretion rates of 10 exp -9 and 10 exp - 10 solar masses per year. *ApJ*, **385**, 665–669.

Price, D. J., 2008. Modelling discontinuities and Kelvin Helmholtz instabilities in SPH. *Journal of Computational Physics*, **227**, 10040–10057.

Price, D. J., 2012. Smoothed particle hydrodynamics and magnetohydrodynamics. *Journal of Computational Physics*, **231**, 759–794.

Price, D. J. & Monaghan, J. J., 2007. An energy-conserving formalism for adaptive gravitational force softening in smoothed particle hydrodynamics and N-body codes. *MNRAS*, **374**, 1347–1358.

Proga, D., Kallman, T. R., Drew, J. E. & Hartley, L. E., 2002. Resonance Line Profile Calculations Based on Hydrodynamical Models of Cataclysmic Variable Winds. *ApJ*, **572**, 382–391.

Pskovskii, I. P., 1977. Light curves, color curves, and expansion velocity of type I supernovae as functions of the rate of brightness decline. *Soviet Ast.*, **21**, 675–682.

Rest, A., Matheson, T., Blondin, S., Bergmann, M., Welch, D. L. et al., 2008. Spectral Identification of an Ancient Supernova Using Light Echoes in the Large Magellanic Cloud. *ApJ*, **680**, 1137–1148.

Rest, A., Suntzeff, N. B., Olsen, K., Prieto, J. L., Smith, R. C., Welch, D. L., Becker, A., Bergmann, M., Clocchiatti, A., Cook, K., Garg, A., Huber, M., Miknaitis, G., Minniti, D., Nikolaev, S. & Stubbs, C., 2005. Light echoes from ancient supernovae in the Large Magellanic Cloud. *Nature*, **438**, 1132–1134.

Rosino, L. & Iijima, T., 1987. The 1985 Outburst of RS Ophiuchi. In M. F. Bode, ed., *RS Ophiuchi (1985) and the Recurrent Nova Phenomenon*, 27.

Rosswog, S., 2009. Astrophysical smooth particle hydrodynamics. *New Astronomy Reviews*, **53**, 78–104.

Rosswog, S., 2014. Boosting the accuracy of SPH techniques: Newtonian and special-relativistic tests. *ArXiv e-prints*.

Rosswog, S. & Price, D., 2007. MAGMA: a three-dimensional, Lagrangian magnetohydrodynamics code for merger applications. *MNRAS*, **379**, 915–931.

Ruiz-Lapuente, P., Comeron, F., Méndez, J., Canal, R., Smartt, S. J., Filippenko, A. V., Kurucz, R. L., Chornock, R., Foley, R. J., Stanishev, V. & Ibata, R., 2004. The binary progenitor of Tycho Brahe's 1572 supernova. *Nature*, **431**, 1069–1072.

Rupen, M. P., Mioduszewski, A. J. & Sokoloski, J. L., 2008. An Expanding Shell and Synchrotron Jet in RS Ophiuchi. *ApJ*, **688**, 559–567.

Saio, H. & Nomoto, K., 2004. Off-Center Carbon Ignition in Rapidly Rotating, Accreting Carbon-Oxygen White Dwarfs. *ApJ*, **615**, 444–449.

Saitoh, T. R. & Makino, J., 2009. A Necessary Condition for Individual Time Steps in SPH Simulations. *ApJ*, **697**, L99–L102.

Saitoh, T. R. & Makino, J., 2013. A Density-independent Formulation of Smoothed Particle Hydrodynamics. *ApJ*, **768**, 44.

Schoenberg, I. J., 1946. Contributions to the problem of approximation of equidistant data by analytic functions. *Quart. Appl. Math*, **4**(2), 45–99.

Schwarzschild, M., 1965. *Structure and evolution of the stars*. New York: Dover Publication, 1965.

Sedov, L. I., 1959. *Similarity and Dimensional Methods in Mechanics*. New York: Academic Press.

Shappee, B. J., Stanek, K. Z., Pogge, R. W. & Garnavich, P. M., 2013. No Stripped Hydrogen in the Nebular Spectra of Nearby Type Ia Supernova 2011fe. *ApJ*, **762**, L5.

Shen, K. J., Guillochon, J. & Foley, R. J., 2013. Circumstellar Absorption in Double Detonation Type Ia Supernovae. *ApJ*, **770**, L35.

Shore, S. N., Kenyon, S. J., Starrfield, S. & Sonneborn, G., 1996. On the Interpretation of the Ultraviolet Spectra of Symbiotic Stars and Recurrent Novae. II. The 1985 Outburst of RS Ophiuchi. *ApJ*, **456**, 717.

Shore, S. N., Schwarz, G. J., De Gennaro Aquino, I., Augusteijn, T., Walter, F. M., Starrfield, S. & Sion, E. M., 2013. The spectroscopic evolution of the recurrent nova T Pyxidis during its 2011 outburst. II. The optically thin phase and the structure of the ejecta in recurrent novae. *A&A*, **549**, A140.

Simon, J. D., Gal-Yam, A., Gnat, O., Quimby, R. M., Ganeshalingam, M. et al., 2009. Variable Sodium Absorption in a Low-extinction Type Ia Supernova. *ApJ*, **702**, 1157–1170.

Sobolev, V. V., 1947. *Moving envelopes of stars*. Leningrad: Leningrad State UP.

Sod, G. A., 1978. A survey of several finite difference methods for systems of nonlinear hyperbolic conservation laws. *Journal of Computational Physics*, **27**, 1–31.

Sokoloski, J. L., Luna, G. J. M., Mukai, K. & Kenyon, S. J., 2006. An X-ray-emitting blast wave from the recurrent nova RS Ophiuchi. *Nature*, **442**, 276–278.

Sokoloski, J. L., Rupen, M. P. & Mioduszewski, A. J., 2008. Uncovering the Nature of Nova Jets: A Radio Image of Highly Collimated Outflows from RS Ophiuchi. *ApJ*, **685**, L137–L140.

Springel, V., 2005. The cosmological simulation code GADGET-2. *MNRAS*, **364**, 1105–1134.

Springel, V., 2010. Smoothed Particle Hydrodynamics in Astrophysics. *ARA&A*, **48**, 391–430.

Springel, V. & Hernquist, L., 2002. Cosmological smoothed particle hydrodynamics simulations: the entropy equation. *MNRAS*, **333**, 649–664.

Stehle, M., Mazzali, P. A., Benetti, S. & Hillebrandt, W., 2005. Abundance stratification in Type Ia supernovae - I. The case of SN 2002bo. *MNRAS*, **360**, 1231–1243.

Stein, J. & Wheeler, J. C., 2006. The Convective Urca Process with Implicit Two-dimensional Hydrodynamics. *ApJ*, **643**, 1190–1197.

Sternberg, A., Gal-Yam, A., Simon, J. D., Leonard, D. C., Quimby, R. M. et al., 2011. Circumstellar Material in Type Ia Supernovae via Sodium Absorption Features. *Science*, **333**, 856–.

Sterne, T. E., 1939. Apsidal motion in binary stars. *MNRAS*, **99**, 451–462.

Storey, P. J. & Hummer, D. G., 1995. Recombination line intensities for hydrogenic ions-IV. Total recombination coefficients and machine-readable tables for Z=1 to 8. *MNRAS*, **272**, 41–48.

Sullivan, M., Le Borgne, D., Pritchet, C. J., Hodsman, A., Neill, J. D. et al., 2006. Rates and Properties of Type Ia Supernovae as a Function of Mass and Star Formation in Their Host Galaxies. *ApJ*, **648**, 868–883.

Sutherland, R. S. & Dopita, M. A., 1993. Cooling functions for low-density astrophysical plasmas. *ApJS*, **88**, 253–327.

Theuns, T. & Jorissen, A., 1993. Wind Accretion in Binary Stars - Part One - Intricacies of the Flow Structure. *MNRAS*, **265**, 946.

Thoroughgood, T. D., Dhillon, V. S., Littlefair, S. P., Marsh, T. R. & Smith, D. A., 2001. The mass of the white dwarf in the recurrent nova U Scorpii. *MNRAS*, **327**, 1323–1333.

Totani, T., Morokuma, T., Oda, T., Doi, M. & Yasuda, N., 2008. Delay Time Distribution Measurement of Type Ia Supernovae by the Subaru/XMM-Newton Deep Survey and Implications for the Progenitor. *PASJ*, **60**, 1327–.

Truran, J. W., Arnett, W. D. & Cameron, A. G. W., 1967. Nucleosynthesis in supernova shock waves. *Canadian Journal of Physics*, **45**, 2315.

Verner, D. A., Ferland, G. J., Korista, K. T. & Yakovlev, D. G., 1996. Atomic Data for Astrophysics. II. New Analytic FITS for Photoionization Cross Sections of Atoms and Ions. *ApJ*, **465**, 487.

von Neumann, J. & Richtmyer, R. D., 1950. A Method for the Numerical Calculation of Hydrodynamic Shocks. *Journal of Applied Physics*, **21**, 232–237.

Vriens, L. & Smeets, A. H. M., 1980. Cross-section and rate formulas for electron-impact ionization, excitation, deexcitation, and total depopulation of excited atoms. *Physical Review A: General Physics*, **22**, 940–951.

Walder, R., Folini, D. & Shore, S. N., 2008. 3D simulations of RS Ophiuchi: from accretion to nova blast. *A&A*, **484**, L9–L12.

Wang, C.-Y. & Chevalier, R. A., 2001. Instabilities and Clumping in Type IA Supernova Remnants. *ApJ*, **549**, 1119–1134.

Warren, J. S., Hughes, J. P., Badenes, C., Ghavamian, P., McKee, C. F., Moffett, D., Plucinsky, P. P., Rakowski, C., Reynoso, E. & Slane, P., 2005. Cosmic-Ray Acceleration at the Forward Shock in Tycho's Supernova Remnant: Evidence from Chandra X-Ray Observations. *ApJ*, **634**, 376–389.

Webbink, R. F., 1984. Double white dwarfs as progenitors of R Coronae Borealis stars and Type I supernovae. *ApJ*, **277**, 355–360.

Wheeler, J. C., Lecar, M. & McKee, C. F., 1975. Supernovae in binary systems. *ApJ*, **200**, 145–157.

Whelan, J. & Iben, Jr., I., 1973. Binaries and Supernovae of Type I. *ApJ*, **186**, 1007–1014.

Williams, B. J., Blair, W. P., Blondin, J. M., Borkowski, K. J., Ghavamian, P., Long, K. S., Raymond, J. C., Reynolds, S. P., Rho, J. & Winkler, P. F., 2011. RCW 86: A Type Ia Supernova in a Wind-blown Bubble. *ApJ*, **741**, 96.

Woltjer, L., 1972. Supernova Remnants. *ARA&A*, **10**, 129.

Woosley, S. E., Taam, R. E. & Weaver, T. A., 1986. Models for Type I supernova. I - Detonations in white dwarfs. *ApJ*, **301**, 601–623.

Worters, H. L., Eyres, S. P. S., Bromage, G. E. & Osborne, J. P., 2007. Resumption of mass accretion in RS Oph. *MNRAS*, **379**, 1557–1561.

Wynn, G., 2008. Accretion in RS Ophiuchi. In A. Evans, M. F. Bode, T. J. O'Brien & M. J. Darnley, eds., *RS Ophiuchi (2006) and the Recurrent Nova Phenomenon*, vol. 401 of *Astronomical Society of the Pacific Conference Series*, 73.

Xu, Y., McCray, R., Oliva, E. & Randich, S., 1992. Hydrogen recombination at high optical depth and the spectrum of SN 1987A. *ApJ*, **386**, 181–189.

Yaron, O., Prialnik, D., Shara, M. M. & Kovetz, A., 2005. An Extended Grid of Nova Models. II. The Parameter Space of Nova Outbursts. *ApJ*, **623**, 398–410.

Yoon, S.-C. & Langer, N., 2005. On the evolution of rapidly rotating massive white dwarfs towards supernovae or collapses. *A&A*, **435**, 967–985.

Yoon, S.-C., Podsiadlowski, P. & Rosswog, S., 2007. Remnant evolution after a carbon-oxygen white dwarf merger. *MNRAS*, **380**, 933–948.

Zamanov, R. K., Bode, M. F., Melo, C. H. F., Bachev, R., Gomboc, A., Stateva, I. K., Porter, J. M. & Pritchard, J., 2007. Rotational velocities of the giants in symbiotic stars - II. Are S-type symbiotics synchronized? *MNRAS*, **380**, 1053–1063.

Zamanov, R. K., Bode, M. F., Tomov, N. A. & Porter, J. M., 2005. Emission line variability of RS Ophiuchi*. *MNRAS*, **363**, L26–L30.

Zwicky, F., 1940. Types of Novae. *Reviews of Modern Physics*, **12**, 66–85.